Bistatic Synthetic Aperture Radar

By

Gillian Yates

A thesis presented to the University of London for the degree

of Doctor of Philosophy

Department of Electronic and Electrical Engineering

University College London

April 2005

ProQuest LLC
789 East Eisenhower Parkway
P.O. Box 1346
Ann Arbor, MI 48106-1346

Abstract

Synthetic aperture radar (SAR) allows all-weather, day and night, surface surveillance and has the ability to detect, classify and geolocate objects at long stand-off ranges. Bistatic SAR, where the transmitter and the receiver are on separate platforms, is seen as a potential means of countering the vulnerability of conventional monostatic SAR to electronic countermeasures, particularly directional jamming, and avoiding physical attack of the imaging platform. As the receiving platform can be totally passive, it does not advertise its position by RF emissions. The transmitter is not susceptible to jamming and can, for example, operate at long stand-off ranges to reduce its vulnerability to physical attack. This thesis examines some of the complications involved in producing high-resolution bistatic SAR imagery. The effect of bistatic operation on resolution is examined from a theoretical viewpoint and analytical expressions for resolution are developed. These expressions are verified by simulation work using a simple 'point by point' processor. This work is extended to look at using modern practical processing engines for bistatic geometries. Adaptations of the polar format algorithm and range migration algorithm are considered. The principal achievement of this work is a fully airborne demonstration of bistatic SAR. The route taken in reaching this is given, along with some results. The bistatic SAR imagery is analysed and compared to the monostatic imagery collected at the same time. Demonstrating high-resolution bistatic SAR imagery using two airborne platforms represents what I believe to be a European first and is likely to be the first time that this has been achieved outside the US (the UK has very little insight into US work on this topic).

Bistatic target characteristics are examined through the use of simulations. This also compares bistatic imagery with monostatic and gives further insight into the utility of bistatic SAR.

Acknowledgements

There are many people I would like to thank for their assistance in encouraging me to complete this thesis. Firstly, I would like to thank Andrew Horne for his leadership and direction on this project. Without his insight this work would not have happened. I would also thank the MoD's Corporate Research Programme for funding this work and allowing me to publish it. I am also grateful to QinetiQ for funding my PhD at UCL.

I would like to thank Professor Hugh Griffiths for accepting me as one of his research students and his continued encouragement throughout. Thanks to Hugh and Professor Chris Baker for their helpful comments and guidance.

The modelling results from Spectre have been provided by Dr. Daniel Andre. I am grateful for him allowing me to use his results in this thesis. I would also like to thank Robert Middleton for developing an autofocus routine which runs on a SAR image, and so is equally applicable to bistatic or monostatic imagery. Without this, the bistatic SAR imagery would not be as impressive.

I would like to thank Alan Blake and my other QinetiQ colleagues for supporting me in the writing of this thesis. I would also like to thank Alan for the use of his image manipulation tool Imanip, which greatly eases the work required in testing programs such as the range migration algorithm work.

Thanks must finally go to my family and friends for their never-ending support and encouragement to complete this.

Contents

List of abbreviations

ADAS	Airborne Data Acquisition System
ATR	Assisted Target Recognition
BAC	Bistatic Alert and Cueing
BBC	British Broadcasting Corporation
BTT	Bistatic Technology Transition
CAD	Computer Aided Design
CDF	Cumulative distribution function
DARPA	Defense Advanced Research Project Agency
ECM	Electronic Counter Measures
ESR	Enhanced Surveillance Radar
EUSAR	EUropean conference on SAR
FFT	Fast Fourier Transform
GO	Geometrical Optics
GPS	Global Positioning System

ISAR	Inverse Synthetic Aperture Radar
IMU	Inertial Measurement Unit
moco	MOtion COmpensation
MoD	Ministry of Defence
MTI	Moving Target Indication
MTRC	Motion Through Range Cells
PFA	Polar Format Algorithm
PGA	Phase Gradient Autofocus
PO	Physical Optics
PPS	Pulse Per Second
PRF	Pulse Repetition Frequency
PRI	Pulse Repetition Interval
PTD	Physical Theory of Diffraction
RCS	Radar Cross Section
RF	Radio Frequency
RMA	Range Migration Algorithm
SAR	Synthetic Aperture Radar

TBIRD	Tactical BIstatic Radar Demonstration
UCL	University College London

List of symbols

alt	Platform Altitude above z=0
alt_R	Receiver Altitude above z=0
alt_T	Transmitter Altitude above z=0
α_0	Angle from positive x-axis to the vector from origin to centre of Tx aperture
β	Bistatic angle
β_0	Angle from positive x-axis to the vector from origin to centre of Rx aperture
B	Bandwidth
c	Speed of light
f	Instantaneous frequency $-B/2<f\leq B/2$
f_0	Centre frequency
L	Synthetic aperture length
ϕ	Phase of the signal

ϕ_0	Constant part of the phase of the signal
ϕ_{VAR}	Variable part of the phase of the signal
$_R$ (subscript)	A quantity belonging to the receiver
Rg	Ground range (when platform has altitude)
R_0	Range from platform to scene centre at time $t=0$
R_{0R}	Range from receiver to scene centre at time $t=0$
R_{0T}	Range from transmitter to scene centre at time $t=0$
R	Range from platform to scene centre at time t
R_R	Range from receiver to scene centre at time t
R_T	Range from transmitter to scene centre at time t
R_t	Range from platform to target
R_{Rt}	Range from receiver to target
R_{Tt}	Range from transmitter to target
Rx	Receiver
ΔR	$R_t - R$
t	Time ($-T/2 < t \leq T/2$)
T	Aperture time

$_T$ (subscript)	Quantity belonging to the transmitter
Tx	Transmitter
θ_R	$-\alpha_0 - \pi/2$
θ_T	$-\beta_0 - \pi/2$
v	Velocity of the platform
v_R	Velocity of the receiving platform
v_T	Velocity of the transmitting platform
x_t	Target/scatter location in x-axis
x_{tTx}	Position of x_t in Tx coordinate frame
x_{0T}	x-position of Tx at time $t=0$
x_T	x-position of Tx at time t
y_t	Target/scatter location in y-axis
y_{tTx}	Position of y_t in Tx coordinate frame
y_{0T}	y-position of Tx at time $t=0$
y_T	y-position of Tx at time t
z_t	Target/scatter location in z-axis
z_{tTx}	Position of z_t in Tx coordinate frame

z_{0T}	z-position of Tx at time $t=0$
z_T	z-position of Tx at time t

Chapter 1. Introduction

1.1 Synthetic Aperture Radar (SAR)

A long antenna can be synthesised by coherently integrating the returns from moving a short antenna along a long track, [3], thus allowing fine azimuth resolution normally restricted by the physical length of the antenna. The imaging platform is generally airborne or spaceborne. High resolution is obtained in azimuth by long integration times and in range by the use of high bandwidths. This allows for high-resolution, map like images of the ground to be obtained in all weather conditions both at day and night.

1.2 Bistatic SAR

Modern bistatic radar assumes the transmitter and receiver to be separated by a considerable distance. For bistatic SAR this implies that the transmitter and receiver are onboard separate platforms. Bistatic SAR imagery can be formed with only one platform moving (the transmitter or the receiver) or both platforms moving. Within the scope of this project both platforms have been taken to be airborne, although the work presented here would relate equally well to all scenarios (platforms being airborne, spaceborne, and/or one of them stationary). No restrictions on the trajectories of the two platforms have been made, making this work applicable to any bistatic SAR scenario.

Interest in bistatic SAR has been increasing in recent years due to the advantages it brings. The main advantage is that it can overcome many counter measures. As the receiver in a bistatic system can be completely passive, it does

not advertise its position. Any electronic counter measures (ECM) will be aimed at the transmitter and, depending on the bistatic configuration, will have little or no effect on the imagery collected. Also using an expensive high-power transmitter at long stand off ranges reduces the risk of physical attack to it. The passive receiver can be less expensive and located close to the area of interest. Another possible advantage of bistatic SAR is the ability to reduce the effectiveness of target stealth. Most stealth techniques aim to reduce backscatter at the expense of scatter in other directions. Bistatic SAR configurations could be employed to take advantage of this.

In addition, urban environments are made up of large trihedral structures which result in very strong monostatic returns, obscuring target information in the immediate vicinity. This effect will not occur in bistatic imagery, thus producing clearer imagery of manmade environments.

Bistatic SAR regimes introduce complications. These complications can be divided into two areas. The first is hardware issues such as synchronisation and phase noise. Due to the high bandwidths and long integration times, synchronisation in both time and frequency is vital to high-resolution bistatic SAR. Synchronisation in time allows each transmitted pulse to be recorded at the correct instant at the receiver and range to be evaluated accurately, which is vital for geolocation accuracy. Synchronisation in frequency is needed to maintain coherency between the transmitter and receiver. Accurate synchronisation allows longer integration times and thus higher azimuth resolution. A monostatic radar uses the same master oscillator for both transmitted and received signals. Low frequency components of phase noise

have little effect on system performance as they do not change much over the period of a send-receive cycle. In the bistatic case, different oscillators are used so the imaging process is susceptible to the whole spectrum of phase noise, thus minimising the phase noise in the systems is vital. These hardware issues need to be overcome to produce high-resolution bistatic SAR imagery.

The second area of complication is concerned with image processing issues. Existing SAR processors (and processing algorithms) will need to be adapted for bistatic scenarios. Issues such as motion compensation and autofocus will need to be tackled. Bistatic motion compensation will need to take into account the motion of each platform. An autofocus correcting for error in both platforms' positions will need implemented for high-resolution imagery to be obtained.

1.3 Bistatic definitions

The aim of this section is to briefly set out an example bistatic geometry and define some of the terminology used within this thesis. Throughout this report the subscript '*R*' denotes a quantity belonging to the receiver, and a subscript '*T*' denotes the quantity belonging to the transmitter. A subscript '*0*' denotes being at time zero which is taken to be when the platforms are at the centre of their apertures *i.e.* $-T/2<t<T/2$ and '*T*' (not subscript) is the aperture time. If the platforms are taken to be acting around broadside, the subscript '*0*' denotes the broadside position. A subscript '*t*' (lower case) denotes that a quantity is with respect to the target.

The bistatic angle, β, is defined to be the angle at scene centre formed from the transmitter to the receiver via that target. In this thesis it is taken to be the angle when the platforms are in the centre of their respective apertures, as shown in Figure 1-1. These and the other terms in Figure 1-1 are summarised in Table 1-1 for the transmitter only.

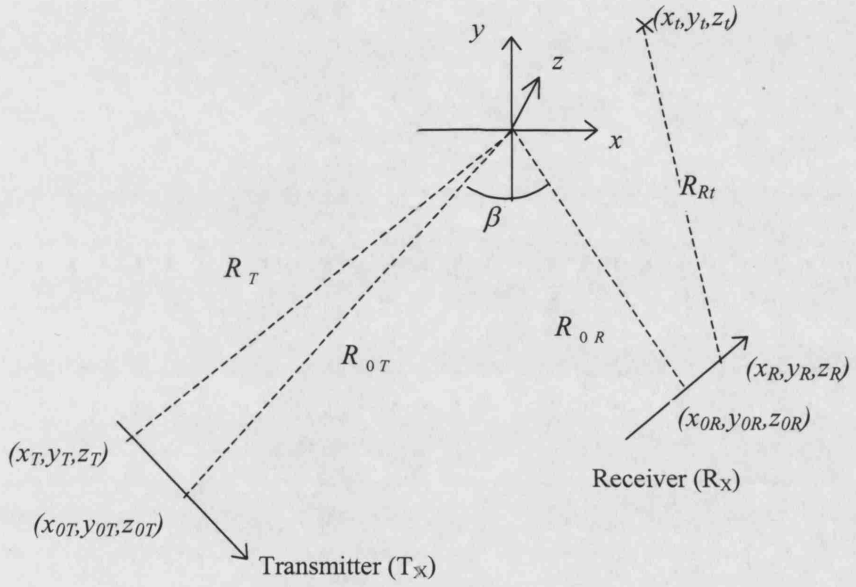

Figure 1-1 Basic bistatic geometry

Quantity	Definition
R_T	Range from transmitter to scene centre at time t
R_{0T}	Range from transmitter to scene centre at time t=0 (the centre of the aperture)
R_{Tt}	Range from transmitter to target at time t
(x_T,y_T,z_T)	Position of transmitter at time t
(x_{0T},y_{0T},z_{0T})	Position of transmitter at time t=0 (the centre of the aperture)
(x_t,y_t,z_t)	Target/scatter location (generally taken as in the plane z=0)

Table 1-1 Definitions for bistatic geometry

1.4 Motivation

The main driving force behind this development of bistatic SAR is that it is anticipated that it would offer high-resolution SAR imagery in situations where monostatic imagery cannot be formed. These are likely to include situations where the transmitter is being jammed through use of electronic counter measures (ECM), denying the conventional monostatic SAR imagery. As the receiver can be made totally passive, it can remain undetected and thus will not be subjected to any directional jamming. This restores the SAR capability allowing surveillance to be maintained.

1.5 Objectives

This work aims to develop a greater understanding of the issues involved in producing high-resolution bistatic SAR imagery. This is expected to be achieved through the development of theoretical understanding as well as a proof of concept experiment to demonstrate that high-resolution bistatic SAR imagery can be formed. It is planned that a greater understanding of the characteristics of bistatic SAR imagery be gained from the imagery from the trial as well as simulation work.

1.6 Methodology

The work begins with developing analytical expressions for bistatic SAR resolution. This theoretical work develops an understanding of what can be expected from any later experimental work. The study then progresses to examining possible adaptations of existing monostatic processing engines for bistatic geometries. This includes the Polar Format Algorithm (PFA) and the

Range Migration Algorithm (RMA). The results from these adaptations are examined using simulations.

The work culminates in a fully airborne bistatic SAR demonstration. Initial ground tests are carried out to examine the results of synchronisation and phase noise. Once these have been examined, the work progresses to a bistatic SAR demonstration using two airborne platforms. The results from this experiment have been processed and the bistatic SAR imagery is discussed in comparison to the monostatic imagery collected at the same time.

Simulations using RCS prediction code (Spectre) have been used to further the understanding of what is seen in the experimental data. This also looks at target signatures of a simplified T72 tank.

1.7 Novel aspects of the work

This work produces high-resolution bistatic SAR imagery using two airborne platforms. The platforms are allowed to fly arbitrary tracks *i.e.* they are not constrained to flying parallel tracks or at similar altitudes. This is certainly a UK and European first and possibly a World first, although very little information in open literature exists of work on this topic outside of Europe.

Two conference papers have been written from results of this work. The first of these presented initial theoretical work to Radar 2002, [1]. The second presented the later airborne demonstration results and was given at EUSAR 2004, [2]. An extended version of the EUSAR paper is currently in the IEE review process for a special EUSAR 2004 edition of the journal of Radar, Sonar and Navigation.

Chapter 2. Context of the research

2.1 Introduction

Bistatic radar is not a new concept. In fact, the first radars developed around the turn of the 20th century were bistatic. They remained that way until advances in engineering (the development of the transmit/receive switch) allowed the transmitter and receiver to be co-located. Since then the majority of the research and development for radar has been focused on monostatic configurations.

The topic of bistatic radar is one that keeps reappearing, usually when a new application for it arises. Currently bistatic radar is undergoing a resurgence in interest. This is due to the need to overcome counter measures, its counter stealth capability and from the use of passive bistatic radars. This is when a transmitter of opportunity is used, *i.e.* one not under the control of the operator of the receiver. This overcomes the need for a dedicated, often expensive transmitter.

This section briefly covers open literature on the history and development of bistatic radar, before concentrating on the more relevant but limited topic of bistatic SAR.

2.2 Bistatic radar

One of the most comprehensive works on all aspects of the history and development of bistatic radar is a book by Willis entitled simply 'Bistatic

Radar' [4]. It covers the first radar experiments in the early 1900's, through the first concepts of bistatic radar. The author reviews the development of bistatic radar on a country-by-country basis. This book expands on a chapter written by Willis appearing in Skolnik's Radar Handbook [5]. This chapter in Skolnik acts as a good summary of Willis' work. Willis covers in depth the reasons for each resurgence of interest in bistatic radar, and the uses of bistatic radar over the last hundred years. Although this book mainly concentrates on stationary radar, the topic of bistatic SAR is covered, albeit briefly. Willis reports on the experimental results obtained by Auterman reported in [6]; see separate paragraph. Willis discusses the effect of bistatic geometries on SAR resolution, as well as the synchronisation issues involved. In later sections, Willis develops an approximate expression for bistatic range resolution from the transmitters and receivers angle of rotation around the target.

Another comprehensive review of bistatic radar is provided by Dunsmore in a chapter of [7]. Dunsmore provides a full history of bistatic radar, with particular interest in UK radar development (along with the US and USSR). He mentions the requirement of a bistatic receiver to follow the energy from the transmitter's pulses (pulse chasing). The book comments on the target detection advantages of bistatic over monostatic, such as overcoming counter measures and the covertness of the receiver. He also looks at the design and operational advantages and disadvantages of bistatic operation. He suggests the use of atomic clocks to overcome complications with accurate time and frequency of both radar, along with the use of Global Positioning System (GPS) to aid pulse timing, platform location and motion. The book mostly concentrates on systems where the both the transmitter and receiver are ground based and stationary.

Dunsmore discusses aspects of bistatic radar cross section (RCS), and repeats interesting results by others on the subject. Dunsmore comments on an experimental airborne bistatic SAR system developed jointly by Xantech and Goodyear Aerospace (Bistatic Technology transition (BTT) / Tactical Bistatic Radar Demonstration (TBIRD)). Here time synchronisation was achieved with a pair of rubidium atomic clocks. Dunsmore concludes his review with the belief that the future of bistatic radar lies with the low-cost passive bistatic operation. Although the use of passive radars is an active area of research, I believe the other advantages of bistatic SAR (such as counter vulnerability) make it of interest for an active system also.

Along with Willis' book, Dunsmore's work acts as a good introduction to the area of bistatic work and provides a useful and extensive list of references for the researcher to pursue their particular areas of interest.

An early work on the geometrical effects of bistatic radar is given by Jackson in [8]. The author only considers static platforms since, as he says: "*platform motion introduces immense complications*". The author cites the problems of imaging near the receiver or the baseline (the line between the transmitter and receiver). One of the main advantages of bistatic operation is cited as being able to use higher pulse repetition frequencies since range ambiguities can be resolved using the geometry. The advantages of having imagery from both the transmitter (monostatic) and the bistatic receiver are examined. This work provides a comprehensive guide to the considerations of bistatic geometries.

A good paper produced on multistatic radar (not SAR) was written by Milne, [9]. The author presents theoretical considerations of the advantages and

implementations of multistatic surveillance radar. He discusses the deficiencies in monostatic radar such as its susceptibility to interference. This paper is a comprehensive work, highlighting the advantages of separating the radar transmitter and receiver. These advantages include the system being virtually immune to deliberate directional interference. Also, using multiple receivers allows triangulation to resolve range and velocity ambiguities as well as locating interference sources.

2.3 Passive bistatic radar

In recent years there has been considerable interest in passive bistatic systems. This is where the radar receiver is working independently of the transmitter, and the transmitter has no knowledge of the receiver's existence. This produces radar imagery without the need for a dedicated, expensive transmitter, and uses a passive receiver with the opportunity for complete covertness, sometimes known as 'hitchhiking'. This has other advantages such as it allows the use of frequencies not normally available due to licensing issues.

An early example of work in this field is given by Schoenenberger and Forrest in [10]. This paper looks at both passive and active bistatic radar configurations (*i.e.* where the transmitter is under the same control as the receiver and when the two are totally independent). The main reason for using bistatic radar is given as the need to overcome man-made interference sources (jammers). This work focuses on overcoming two main disadvantages of bistatic radar. The first is the requirement that the receiver has information on the transmitter's pulse timings, pointing direction and a coherent RF reference. The second is the problem of displaying the results on the plan-position-indicator. Solutions to

overcome each problem are suggested including direct path reception of the transmitted signal or the transfer of information between the radars using telecommunications. Solutions to these problems have been demonstrated in a passive radar experiment using the air traffic control radar at Heathrow and a receiver situated at University College London (UCL).

Further work on this topic is presented by Griffiths and Carter [11]. Here the civil air traffic control radar at Heathrow airport is used as transmitter of opportunity with a receiver at UCL. The authors discuss way of achieving coherence between the radars at the receiver. In order to keep the receiver completely independent the solution to this problem is found by using the return from close in clutter as a coherent reference. The system is used for moving target indication (MTI) and experimental results are presented.

More recent published work by Howland describes research on a passive bistatic radar system using a television transmitter as a transmitter of opportunity in [12]. His work covers a brief summary of previous experiments by Griffiths *et al.* using a receiver at UCL and a television transmitter 12km away at Crystal Palace as well as satellite broadcast television transmissions. Howland uses the Doppler shift and the direction of arrival to detect and track airborne targets. No timings are made, so the transmitter and receiver do not need to be synchronised. The only requirement on the transmitter is that it is stable and of a known frequency. He presents experimental results using a receiver at Malvern, UK, and a television transmitter 420km away in Northern France. Howland also presents work on this topic in [13] using the BBC

television transmitter at Crystal Palace with a receiver 150km away. Airborne targets were tracked up to 260km away from the receiver.

2.4 Bistatic SAR

Auterman discusses the importance of the master oscillator in a bistatic SAR system in [6]. In monostatic SAR systems using the same master oscillator in the transmit and receive chain significantly cancels out any close to carrier phase noise. There is no similar phase noise cancellation in bistatic SAR. The author presents results from bistatic SAR trials with the transmitter and receiver on different aircraft. Both aircraft were fitted with accurate and stable quartz crystal master oscillators for phase synchronisation. Time synchronisation was achieved using a direct path signal between the aircraft. Auterman presents the processed imagery from experiments with a 2° bistatic angle vertically as well as 40° and 80° bistatic angles horizontally. The imagery has been processed to a nominal resolution of 12.5ft in range and 7ft in azimuth although the author states that that level of performance was not achieved. The imagery presented is remarkable for 1983, however it is unlikely that the phase noise achieved here would be acceptable for the formation of high-resolution imagery. The technical parameters of the experiment (for example the centre frequency was 9.3 GHz) are given. Each platform is flying at the same nominal range (5 nautical miles) and velocity (180 knots), in a parallel configuration. No information on the processing of the imagery is given. The author concludes that for an aperture time of the order of one second, the oscillator phase noise is acceptable. This imagery is also presented in Willis' book [4].

A paper presented at EUSAR (European Conference on SAR) in May 1998 by Martinsek and Goldstein, [15], gives the results of bistatic SAR experiments using a space-borne transmitter and an airborne receiver. The aircraft was flown in the mainbeam of the transmitter, flying a parallel track. Frequency synchronisation was achieved using the direct path from the transmitter collected via an antenna on top of the receiver. The imagery is processed by range compression, by convolving each target echo with its reference signal from the direct path, and azimuth compression achieved using a discrete Fourier transform. A sample of their bistatic imagery of an area in Alaska is presented. The image has a pixel spacing of 12m suggesting the resolution to be of that order.

Sandia National laboratories have a 1-metre resolution bistatic SAR image on their website [14]. Little information is given about the technical work behind this or the details of the experiment. The interest is only in the quality of the image and the date, 28th July 1994, when covering the history of bistatic SAR.

An article by Elson, [16], reports on the planned flight test program to examine the feasibility of using airborne bistatic radar to enhance air-to-ground surveillance as part of the US Sanctuary Program. The programme, which was due to start in September 1980, aimed to prove the concept of bistatic imagery and investigate some bistatic geometries. The author discusses the difficulties that bistatic SAR introduces (such as problems with coherence). This report aims to publicise the forthcoming work, and holds little technical content.

The same topic is discussed in an article published in Defense Electronics journal by Blumgold, [17]. This provides more details of the joint Air Force -

DARPA (Defense Advanced Research Project Agency) proof of concept of tactical bistatic radar demonstration (TBIRD) (part of the extensive Sanctuary program). The author reports that the TBIRD program aims to demonstrate clutter tuning[1] for moving target detection, forward looking SAR (with the receiver moving directly towards the target) and large bistatic angles of up to 120°. A data link is used between the platforms and time and phase synchronisation was achieved using rubidium frequency source. The stability of this frequency source was found to be sensitive to low frequency vibration and a had low frequency phase noise problem.

Fawcette provides a comprehensive look at many aspects of the US bistatic programmes such as the Sanctuary program and Bistatic Alert and Cueing (BAC) in [18]. The need to counter platform vulnerability of surveillance systems is sited as the main problem these programmes aim to overcome. The BAC programme (proposed but unfunded at the time of the article) uses a moving 'illuminator of opportunity' with a cheap and portable receiver. The planned X-band demonstrations under the sanctuary program (TBIRD) are described as able to perform both moving target indication (via clutter tuning) and SAR capabilities. An industry source is quoted as saying "If TBIRD shows what we think, we will be able to test it in operational aircraft by 1983".

Although these articles, [16], [17] and [18], provide little technical content, they highlight the amount of interest in bistatic SAR to provide a less vulnerable technique of ground surveillance. These reports all date back to around 1980 and focus on extensive US programmes of work about to start in this field. It

[1] where the receiver is flying so that its motion compensates for the motion of the transmitter creating a zero Doppler shift on the ground area being imaged

appears that any information about this work after 1980, including the results of the TBIRD experiments, is not in open literature.

Kirk examines the problem of bistatic SAR motion compensation in [19]. He hinges the motion compensation problem on the requirement to know the bistatic triangle (with transmitter, target and receiver position as the apexes) and bistatic coherency. He discusses ways in which the receiver can determine the transmitter's position. With each ranging technique he discusses the design requirements and the accuracy of it. Both the requirements for ranging techniques and coherency require either direct path reception of the transmitted signal at the receiver or highly stable clocks on board each platform. Once this information is known, Kirk applies a motion compensation solution which is a combination of the respective monostatic motion compensation solutions for each platform.

Cardillo looks at the area of bistatic SAR resolution in his paper [20]. Using vector analysis the author develops equations for range and Doppler resolution for any point on the ground. He finds that range resolution is dependent only on the directions to the transmitter and receiver, not on the ranges. Doppler resolution is dependent on the angular rates of the platforms about the target. Cardillo also looks at a definition of cross range resolution. He states that as range and Doppler resolutions are often non-orthogonal, they do specify pixel size in a meaningful way, and develops an expression for resolution orthogonal to range resolution.

Work by Soumekh considers imaging problems when using a transmitter and receiver on different aircraft in his paper on an inversion method for bistatic

SAR [21]. The author develops an inversion method and compares it to a plane wave approximate inversion through the use of simulations. Soumekh's method shows considerably less distortions than the planar wavefront method. He simplifies the problem by assuming both platforms have the same velocity, *i.e.* are flying parallel at the same speed. The same author presents later work on image formation using wide bandwidth, continuous wave bistatic SAR [22]. The author cites Skolnik's work, [5], when stating that wideband bistatic SAR imaging systems have been utilised for military recognisance. This work uses a continuous wide-band transmitter which is stationary with respect to the target (for example a geostationary earth orbit (GEO) television station) with an airborne receiver close to the target.

Recently, a programme of work being carried out jointly by the Office National d'Étude et Recherches Aérospatiales (ONERA) and DLR has demonstrated bistatic SAR using two airborne platforms in experiments carried out in February 2003. In [23] the reasons for the attractiveness of bistatic SAR are cited as lower costs (one expensive transmitter with multiple cheaper receive only platforms) single pass interferometry and the use of bistatic scattering for signature analysis. It is interesting that the need to overcome countermeasures such as jamming is not mentioned. In [23], details of the radars used are given, for the experiments the largest bandwidth of the bistatic system is 100MHz. Highly constrained platform geometries are flown to demonstrate a spaceborne system and to investigate scattering mechanisms. In certain geometries processing can be achieved through a monostatic processor, however the authors developed a processor based on the two trajectories of the platforms. Calibration of the bistatic image is achieved through the use of a transponder.

The difficulties in removing the two beam patterns are discussed. The authors present their early imagery from these experiments. These images are discussed further in [24] where the authors concentrate on the production of bistatic interferograms. The authors conclude that bistatic SAR has the potential to reduce the strong dihedral reflections in urban imaging and their results are promising for the use of one transmitter with two receivers for 3D information.

2.5 Conclusions

This chapter examines published work on both bistatic radar and bistatic SAR. There is not a substantial amount of work published in the field of bistatic SAR. Much of the existing work is purely theoretical for example the work by Soumekh [21], [22]. Some of the work does provide bistatic SAR imagery, for example Auterman, [6], Martinsek and Goldststein, [15], Cantalloube and Dubois-Fernandez *et al.*, [23], [24]. However this imagery is not particularly high resolution (although the actual resolution is not given but appears to be of the order of several metres). In all cases the aircraft have been flying highly constrained trajectories such as parallel tracks. The work being presented here provides high-resolution spotlight bistatic SAR imagery without constraining the aircraft to any particular flight paths.

This literature review shows that there is considerable interest in the topic of bistatic SAR. It shows that the difficult aspects of bistatic SAR are synchronising the two platforms and processing the imagery. This review also shows that high-resolution bistatic SAR imagery has not been demonstrated in open literature.

Chapter 3. Bistatic SAR resolution theory

3.1 Introduction

This section formulates the theory of bistatic SAR resolution. It assumes both aircraft are flying along perfectly straight trajectories at zero altitude *i.e.* in the plane of the scene. Both platforms are also taken to be operating around broadside.

3.2 Theory development

This follows closely the method used for deriving the equations for the monostatic SAR resolution theory developed in Appendix A. Imagine each aircraft has associated with it its own set of orthogonal axes, shown for the transmitter in Figure 3-1. Each aircraft is thought to be flying parallel to its corresponding x-axis. A point scatterer is at position (x_t, y_t) in the overall (x,y) coordinate frame. This point has coordinates (x_{tTx}, y_{tTx}) in the transmitter's frame *i.e.* where the transmitter's x-axis, x_{Tx}, is parallel to the transmitters flight path.

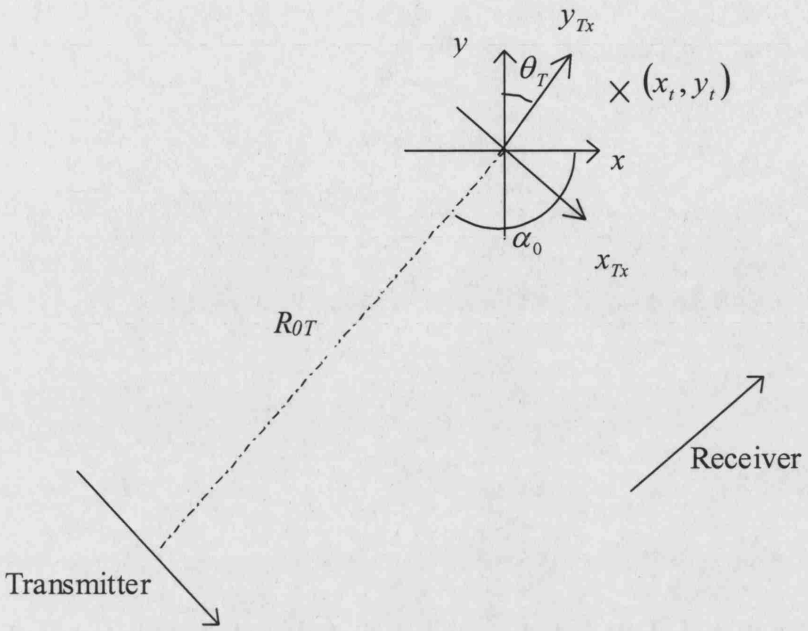

Figure 3-1 Bistatic geometry

The instantaneous range from the transmitter to the target is given by:

$$R_{Tt}^{\ 2} = (tv_T - x_{tTx})^2 + (R_{0T} + y_{tTx})^2 \qquad (1)$$

where R_{0T} is the broadside range from the transmitter to scene centre, v_T is the velocity of the transmitter, t is the time such that $-T/2 < t \le T/2$, and T is the aperture time. The instantaneous range from the transmitter to scene centre is given by:

$$R_T^{\ 2} = R_{0T}^{\ 2} + t^2 v_T^{\ 2} \qquad (2)$$

Similarly for the receiver:

$$R_{Rt}^{\ 2} = (tv_R - x_{tRx})^2 + (R_{0R} + y_{tRx})^2 \qquad (3)$$

$$R_R^{\ 2} = R_{0R}^{\ 2} + t^2 v_R^{\ 2}. \qquad (4)$$

To transform each of these platform-dependant coordinate axes into the overall *(x,y)* axes, a simple rotation transformation needs to be applied to each. To

transform from the (x_{Tx},y_{Tx}) axes to the (x,y) axes shown above, requires a rotation through a positive angle θ_T. To be consistent with the previous work, reference [25], this angle can be expressed in terms of the angle from the positive x-axis to the centre of the transmitter's aperture (denoted α_0), *i.e.* $\theta_T=-\alpha_0-\pi/2$. Similarly for the receiver the rotation angle θ_R can be expressed as $\theta_R=-\beta_0-\pi/2$, where β_0 is the angle between the positive x-axis and the centre of the receiver's aperture.

Applying the rotation transformation leads to expressions for the target location in each coordinate axes in terms of the target position in the overall axes (x,y):

$$x_{tTx} = -x_t \sin(\alpha_0) + y_t \cos(\alpha_0) \tag{5}$$

$$y_{tTx} = -x_t \cos(\alpha_0) - y_t \sin(\alpha_0) \tag{6}$$

$$x_{tRx} = -x_t \sin(\beta_0) + y_t \cos(\beta_0) \tag{7}$$

$$y_{tRx} = -x_t \cos(\beta_0) - y_t \sin(\beta_0) \tag{8}$$

The two-way path to the target is given by $R_t = R_{Tt} + R_{Rt}$. Substituting equations *(5)* and *(6)* into equation *(1)*, and equations *(7)* and *(8)* into equation *(3)* gives:

$$R_t = \sqrt{(tv_T + x_t \sin\alpha_0 - y_t \cos\alpha_0)^2 + (R_{0T} - x_t \cos\alpha_0 - y_t \sin\alpha_0)^2} + \sqrt{(tv_R + x_t \sin\beta_0 - y_t \cos\beta_0)^2 + (R_{0R} - x_t \cos\beta_0 - y_t \sin\beta_0)^2} \tag{9}$$

Subtracting the return from scene centre, $\Delta R = R_t - R$:

$$\begin{aligned}\Delta R = &\left(R_{0T} - x_t\cos\alpha_0 - y_t\sin\alpha_0\right)\sqrt{\left(1+\left(\frac{tv_T + x_t\sin\alpha_0 - y_t\cos\alpha_0}{R_{0T} - x_t\cos\alpha_0 - y_t\sin\alpha_0}\right)^2\right)}\\ &- R_{0T}\sqrt{1+\left(\frac{tv_T}{R_{0T}}\right)^2}\\ &+\left(R_{0R} - x_t\cos\beta_0 - y_t\sin\beta_0\right)\sqrt{\left(1+\left(\frac{tv_R + x_t\sin\beta_0 - y_t\cos\beta_0}{R_{0R} - x_t\cos\beta_0 - y_t\sin\beta_0}\right)^2\right)}\\ &- R_{0R}\sqrt{1+\left(\frac{tv_R}{R_{0R}}\right)^2}.\end{aligned} \tag{10}$$

Using the binomial theorem to expand the four square root terms above to include quadratic terms gives:

$$\begin{aligned}\Delta R \approx &\left(R_{0T} - x_t\cos\alpha_0 - y_t\sin\alpha_0\right)\left(1+\frac{1}{2}\left(\frac{tv_T + x_t\sin\alpha_0 - y_t\cos\alpha_0}{R_{0T} - x_t\cos\alpha_0 - y_t\sin\alpha_0}\right)^2\right)\\ &+\left(R_{0R} - x_t\cos\beta_0 - y_t\sin\beta_0\right)\left(1+\frac{1}{2}\left(\frac{tv_R + x_t\sin\beta_0 - y_t\cos\beta_0}{R_{0R} - x_t\cos\beta_0 - y_t\sin\beta_0}\right)^2\right)\\ &- R_{0T}\left(1+\frac{1}{2}\left(\frac{tv_T}{R_{0T}}\right)^2\right) - R_{0R}\left(1+\frac{1}{2}\left(\frac{tv_R}{R_{0R}}\right)^2\right).\end{aligned} \tag{11}$$

This can be rearranged as:

$$\begin{aligned}\Delta R \approx &-x_t\left(\cos\alpha_0 + \cos\beta_0\right) - y_t\left(\sin\alpha_0 + \sin\beta_0\right)\\ &+\frac{t^2{v_T}^2 + x_t\sin^2\alpha_0 + {y_t}^2\cos^2\alpha_0 + 2tv_Tx_t\sin\alpha_0 - 2tv_Ty_t\cos\alpha_0 - 2x_ty_t\sin\alpha_0\cos\alpha_0}{2\left(R_{0T} - x_t\cos\alpha_0 - y_t\sin\alpha_0\right)}\\ &+\frac{t^2{v_R}^2 + x_t\sin^2\beta_0 + {y_t}^2\cos^2\beta_0 + 2tv_Rx_t\sin\beta_0 - 2tv_Ry_t\cos\beta_0 - 2x_ty_t\sin\beta_0\cos\beta_0}{2\left(R_{0R} - x_t\cos\beta_0 - y_t\sin\beta_0\right)}\\ &-\frac{t^2{v_T}^2}{2R_{0T}} - \frac{t^2{v_R}^2}{2R_{0R}}.\end{aligned} \tag{12}$$

The phase from transmitter to receiver via a scatterer at Cartesian location *(x,y)* relative to scene centre is given by:

$$\phi = \frac{2\pi}{c}\Delta R\left(f + f_0\right) \tag{13}$$

where the frequency f is such that $-B/2 \leq f \geq B/2$, B is the bandwidth, f_0 is the centre frequency and c is the speed of light. Separating ϕ into the constant and varying parts, *i.e.* $\phi = \phi_0 + \phi_{VAR}(t, f)$, gives:

$$\begin{aligned}\phi_{VAR} \approx & \frac{2\pi}{c} f \Delta R \\ & + \frac{2\pi}{c} f_0 \left(- \frac{t^2 v_T{}^2}{2R_{0T}} - \frac{t^2 v_R{}^2}{2R_{0R}} + \frac{t^2 v_T{}^2 + 2tv_V x_t \sin\alpha_0 - 2tv_T y_t \cos\alpha_0}{2\left(R_{0T} x_t - \cos\alpha_0 - y_t \sin\alpha_0\right)} \right. \\ & \left. + \frac{t^2 v_R{}^2 + 2tv_R x_t \sin\beta_0 - 2tv_R y_t \cos\beta_0}{2\left(R_{0R} - x_t \cos\beta_0 - y_t \sin\beta_0\right)} \right).\end{aligned} \tag{14}$$

For large values of R_0 (compared with x_0 and y_0), $(R_0 - x_t \cos\alpha_0 - y_t \sin\alpha_0) \rightarrow R_0$ and $(R_0 - x_t \cos\beta_0 - y_t \sin\beta_0) \rightarrow R_0$. Using this approximation, equation *(14)* becomes:

$$\begin{aligned}\phi_{VAR} \approx & \frac{2\pi f}{c} \left[- x_t \left(\cos\alpha_0 + \cos\beta_0\right) - y_t \left(\sin\alpha_0 + \sin\beta_0\right) \right. \\ & + \frac{x_t{}^2 \sin^2\alpha_0}{2R_{0T}} + \frac{y_t{}^2 \cos^2\alpha_0}{2R_{0T}} \\ & + \frac{2tv_T x_t \sin\alpha_0}{2R_{0T}} - \frac{2tv_T y_t \cos\alpha_0}{2R_{0T}} - \frac{2x_t y_t \cos\alpha_0 \sin\alpha_0}{2R_{0T}} \\ & + \frac{x_t{}^2 \sin^2\beta_0}{2R_{0R}} + \frac{y_t{}^2 \cos^2\beta_0}{2R_{0R}} \\ & \left. + \frac{2tv_R x_t \sin\beta_0}{2R_{0R}} - \frac{2tv_R y_t \cos\beta_0}{2R_{0R}} - \frac{2x_t y_t \sin\beta_0 \cos\beta_0}{2R_{0R}} \right] \\ & + \frac{2\pi f_0}{c} \left(\frac{2tv_T x_t \sin\alpha_0}{2R_{0T}} - \frac{2tv_T y_t \cos\alpha_0}{2R_{0T}} + \frac{2tv_R x_t \sin\beta_0}{2R_{0R}} - \frac{2tv_R y_t \cos\beta_0}{2R_{0R}} \right)\end{aligned} \tag{15}$$

Noting that R_0 is considerably greater than x_t, y_t and t, and assuming f_0 is also considerably greater than both f and t, the dominant terms of equation *(15)* gives:

$$\phi_{VAR} \approx \frac{-4\pi f}{c}\cos\left(\frac{\alpha_0-\beta_0}{2}\right)\left[x_t\cos\left(\frac{\alpha_0+\beta_0}{2}\right)+y_t\sin\left(\frac{\alpha_0+\beta_0}{2}\right)\right] + \frac{2\pi f_0 t}{c}\left[\frac{v_T x_t\sin\alpha_0 - v_T y_t\cos\alpha_0}{R_{0T}} + \frac{v_R x_t\sin\beta_0 - v_R y_t\cos\beta_0}{R_{0R}}\right]. \quad (16)$$

With some manipulation of the second part of this equation, given in Appendix A, it can be expressed as:

$$\phi_{VAR} \approx \frac{4\pi f}{c}\cos\left(\frac{\alpha_0-\beta_0}{2}\right)\left[-x_t\cos\theta_v - y_t\sin\theta_v\right] - \frac{2\pi f_0 t}{c}\sqrt{\frac{v_T^{\,2}}{R_T^{\,2}}+\frac{v_R^{\,2}}{R_R^{\,2}}+\frac{2v_T v_R}{R_T R_R}\cos(\alpha_0-\beta_0)}\left[-x_t\cos\theta_u - y_t\sin\theta_u\right], \quad (17)$$

where $\theta_u = \arctan\left[-\frac{v_T\cos\alpha_0/R_{0T} + v_R\cos\beta_0/R_{0R}}{v_T\sin\alpha_0/R_{0T} + v_R\sin\beta_0/R_{0R}}\right]$, $\theta_v = \cos\left(\frac{\alpha_0+\beta_0}{2}\right)$.

To gain two independent expressions for the 2D resolution of a bistatic SAR system equation *(17)* needs to be separable, *i.e.* of the form ϕ=*A.f.v*+*B.t.u*. Using the definitions of u and v developed by Andrew Horne and defined in reference [25] and shown in Figure 3-2, *i.e.*

$$u = -x\cos\theta_u - y\sin\theta_u \quad (18)$$

$$v = -x\cos\theta_v - y\sin\theta_v \quad (19)$$

the phase becomes:

$$\phi_{VAR} \approx \frac{4\pi f}{c}\cos\left(\frac{\alpha_0-\beta_0}{2}\right)v_t - \frac{2\pi f_0 t}{c}\sqrt{\left[\frac{v_T^{\,2}}{R_T^{\,2}}+\frac{v_R^{\,2}}{R_R^{\,2}}+\frac{2v_T v_R}{R_T R_R}\cos(\alpha_0-\beta_0)\right]}u_t \quad (20)$$

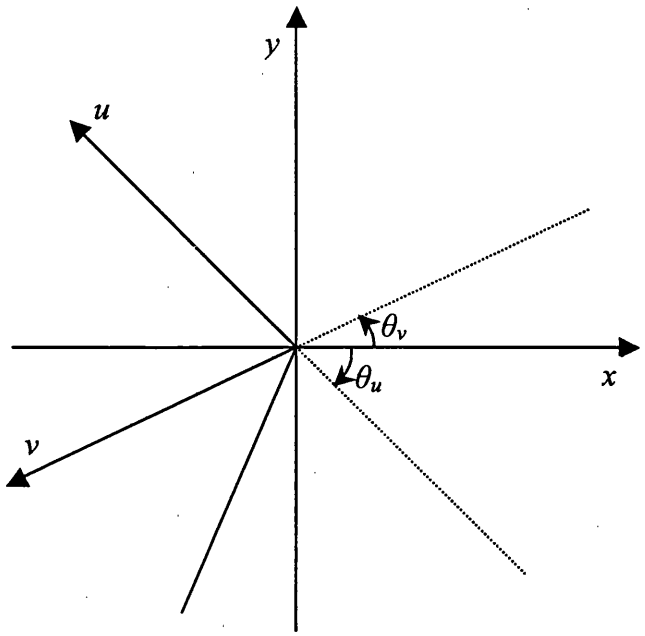

Figure 3-2 Non-orthogonal processing frame as defined in reference [25]

Therefore, neglecting the constant phase term, this gives the response from a scatterer at position (u_0, v_0), $S(f,t)=exp(i\phi)$, as:

$$S(f,t)=\exp i\left\{\begin{array}{l}\dfrac{4\pi f}{c}\cos\left(\dfrac{\alpha_0-\beta_0}{2}\right)v_t- \\ \dfrac{2\pi f_0 t}{c}\sqrt{\left[\dfrac{v_T^{\,2}}{R_T^{\,2}}+\dfrac{v_R^{\,2}}{R_R^{\,2}}+\dfrac{2v_Tv_R}{R_TR_R}\cos(\alpha_0-\beta_0)\right]}u_t\end{array}\right\} \qquad (21)$$

The image is formed by convolving it with its matched filter $H(f,t)$ where:

$$H(f,t)=S^*(f,t)=\exp i\left\{\begin{array}{l}\dfrac{-4\pi f}{c}\cos\left(\dfrac{\alpha_0-\beta_0}{2}\right)v+ \\ \dfrac{2\pi f_0 t}{c}\sqrt{\left[\dfrac{v_T^{\,2}}{R_T^{\,2}}+\dfrac{v_R^{\,2}}{R_R^{\,2}}+\dfrac{2v_Tv_R}{R_TR_R}\cos(\alpha_0-\beta_0)\right]}u\end{array}\right\} \qquad (22)$$

This gives the response to the point target as:

$$s(u,v)=\int_{-\infty}^{\infty}\int_{-\infty}^{\infty}S(f,t)H(f,t)\,df\,dt$$
$$=\int_{-T/2}^{T/2}\exp\left(\frac{2\pi i f_0 t}{c}\sqrt{\left[\frac{v_T^{\,2}}{R_T^{\,2}}+\frac{v_R^{\,2}}{R_R^{\,2}}+\frac{2v_Tv_R}{R_TR_R}\cos(\alpha_0-\beta_0)\right]}\right)(u-u_t)dt \qquad (23)$$
$$\cdot\int_{-\Delta f/2}^{\Delta f/2}\exp\left(\frac{-4\pi i}{c}\cos\left(\frac{\alpha_0-\beta_0}{2}\right)\right)(v-v_t)df.$$

Evaluating these integrals gives:

$$s(u,v)=\operatorname{sinc}\left(\frac{\pi f_0 T}{c}\sqrt{\left[\frac{v_T^{\,2}}{R_T^{\,2}}+\frac{v_R^{\,2}}{R_R^{\,2}}+\frac{2v_Tv_R}{R_TR_R}\cos(\alpha_0-\beta_0)\right]}\right)(u-u_t)$$
$$\operatorname{sinc}\left(\frac{2\pi\Delta f}{c}\cos\left(\frac{\alpha_0-\beta_0}{2}\right)\right)(v-v_t). \qquad (24)$$

So, the resolutions ρ_u and ρ_v in the two dimensions are:

$$\rho_u=\frac{c}{Tf_0\sqrt{\left[\frac{v_T^{\,2}}{R_T^{\,2}}+\frac{v_R^{\,2}}{R_R^{\,2}}+\frac{2v_Tv_R}{R_TR_R}\cos(\alpha_0-\beta_0)\right]}} \qquad (25)$$

$$\rho_v=\frac{c}{2\Delta f\cos\left(\frac{\alpha_0-\beta_0}{2}\right)} \qquad (26)$$

A simple check can be made on these bistatic SAR resolution equations. A monostatic SAR geometry is a special case of a bistatic SAR geometry with the transmitter and receiver co-located, so any results for bistatic SAR should be those for monostatic SAR when the transmitter quantities are set equal to the receiver ones. Here, setting $v_T=v_R=v$, $R_T=R_R=R$ and $\alpha_0=\beta_0$ gives:

$$\rho_u=\frac{c}{Tf_0\sqrt{\left[\frac{v^2}{R^2}+\frac{v^2}{R^2}+\frac{2v^2}{R^2}\cos(0)\right]}}$$

$$= \frac{cR}{2Tf_0 v}$$

$$= \frac{cR}{2f_0 L} \tag{27}$$

$$\rho_v = \frac{c}{2\Delta f} \tag{28}$$

(noting that $vT=L$). Which are identical to the monostatic SAR equations developed in Appendix A.

3.3 Summary

Analytical expressions for the theoretical values of bistatic SAR resolution have been developed in terms of a *u-v* coordinate frame described in reference [25]. These have been shown to be the same as those developed in Appendix A for the case when the transmitter and receiver are collocated. These bistatic equations will be compared with the results from simulation work in the next section.

Chapter 4. Initial simulations

4.1 Introduction

To verify the resolution theory developed in the previous chapter, initial simple simulations have been implemented. These include the simulation of raw bistatic radar data as well as implementing the simplest form of a SAR processor.

4.2 Raw data simulations

To test the theory about a bistatic radar system as discussed in the previous section, one of the first requirements is to obtain raw data. The easiest and cheapest way of generating this is through simple simulations. While generating these, assumptions have been made in order to make the processing more straightforward.

4.2.1 Assumptions

Throughout all simulations the raw data has been formulated such that it is range compressed. The platforms have been modelled as though they are traversing along perfectly straight lines, so that no motion compensation or autofocusing are required. It has also been assumed that they each know their exact position, and that of the other platform. It is assumed that the receiver can constantly record the transmitted signal, so no synchronisation issues have been considered. To initially simplify the problem further, both aircraft are assumed

to be flying at the same altitude (the problem of altitude is introduced in section 5.4). This essentially reduces the problem to a 2D scenario. Each aircraft is assumed to be working in spotlight mode so illumination times do not need to be considered. Only the point target returns any signal, clutter has not been modelled nor has any noise. In these simulations, it has also been assumed that both platforms are flying at the same speed.

The geometries of the aircraft are set up such that when both platforms are at the centre of the aperture the y-axis bisects the bistatic angle, Figure 4-1. This makes the geometry of the processed image easier to interpolate as the v-axis, from the earlier theory, always lies along the vertical (*i.e.* the conventional y-axis).

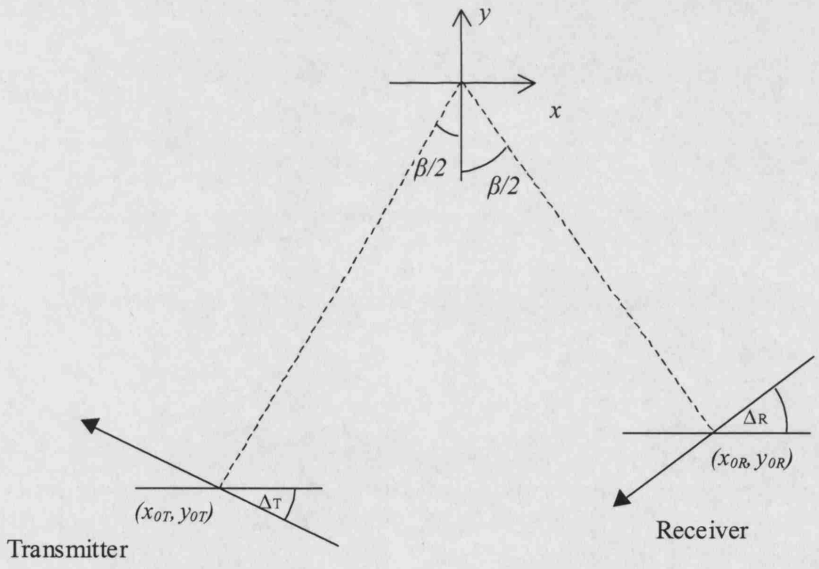

Figure 4-1 Basic bistatic geometry

4.2.2 Raw data program

The program requires the input of the positions of the centre of each aperture, the velocity (as a speed, S, and an angle, Δ, to the positive x-axis) of each platform, as well as the aperture time. From this information, it simulates the data by stepping along each flight path (in steps of platform speed divided by the PRF, noting that the PRF is the same for both platforms). At each step, it calculates each platform's position and then the distance from that position to the given target. The ranges from the transmitter position to the target and the receiver position to the target are then added together to give the total range that the signal has travelled. This value is then halved, to give a bistatic equivalent of one way path length, before being substituted into the range compressed signal return in the form of a sinc function ($\sin(x)/x$) multiplied by a complex exponential.

4.2.3 Results

When both platforms are operating around broadside, the raw data appears similar to that from broadside monostatic radar. The range to scene centre becomes a minimum when both the platforms are broadside to it. It only requires one of the platforms to be squinted for the raw data to appear similar to that from squinted (in either direction) monostatic radar, in this case the global minimum (the turning point) is not recorded in the data.

Three typical results from the raw data simulator are given in Figure 4-2, Figure 4-3 and Figure 4-4.

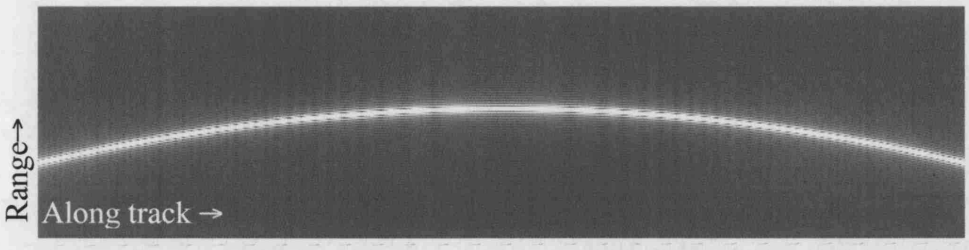

Figure 4-2 Simulated raw data with a bistatic angle of 90°, both platforms at broadside

Figure 4-2 is raw data of a simulated point target at scene centre using a bistatic angle of 90°, with transmitter and receiver both operating around broadside.

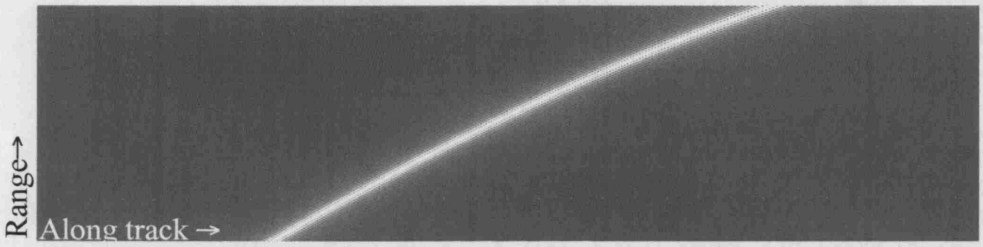

Figure 4-3 Simulated raw data with a bistatic angle of 90°, with the transmitter squinted by 15°

Figure 4-3 is data from a simulated point target at scene centre using a bistatic angle of 90°, with the receiver operating around broadside and the transmitter at a squint angle of 15° (positive squint measured looking forward of broadside).

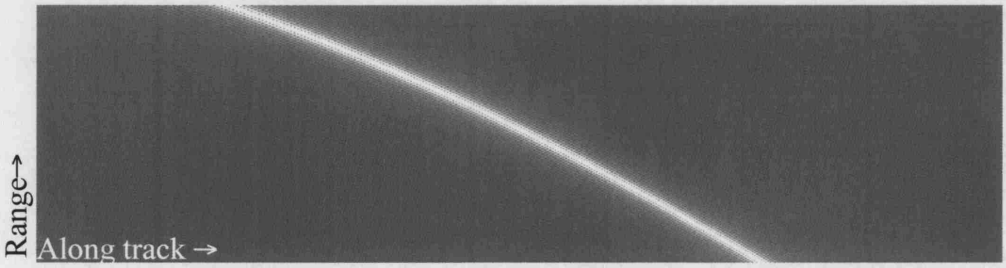

Figure 4-4 Simulated raw data with a bistatic angle of 90°, with the receiver squinted by -15°

Figure 4-4 shows data simulated from a point target at scene centre using a bistatic angle of 90°, with transmitter operating around broadside and the receiver at a squint angle of -15°.

4.3 Point by point processor

The simplest way to process the simulated raw data is on a point by point basis. This compares the actual raw data with the raw data that would be generated from a hypothesised target at each point throughout the scene. Figure 4-5 shows a summary of the point by point processor.

The aperture time used in calculating the azimuth resolution must be taken as only the part of the raw data where the signal has been recorded. In Figure 4-2 this is the whole of the simulated raw data, however in Figure 4-3 and Figure 4-4 the aperture time is shorter than the raw data simulated.

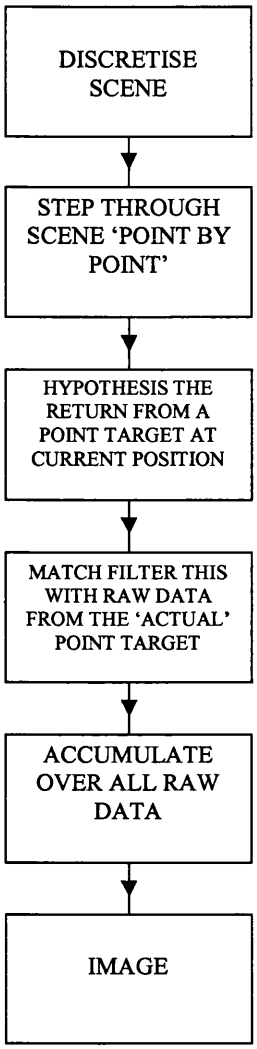

Figure 4-5 Point by point processor flow diagram

4.3.1 Results

Figure 4-6 to Figure 4-8 are the results from processing simulated raw data using the point-by-point processor from three different bistatic geometries. Two sets of raw data have been generated for each geometry. The first is for a single point at scene centre, shown on the left in each figure, the second is a set of five points: one at scene centre, two displaced in azimuth at $(\pm 2m,0)$ and two

displaced in range at $(0,\pm 2m)$, shown on the right. Each of the plots is of range along the vertical axis and azimuth horizontally.

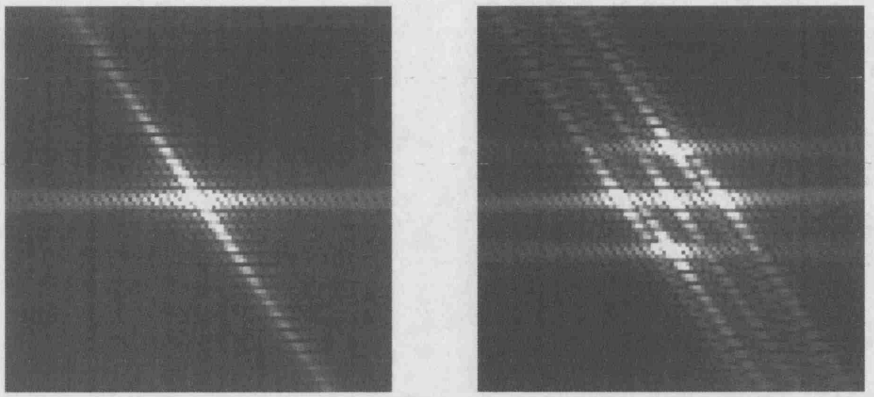

Figure 4-6 Simulated bistatic imagery with 90° bistatic angle

Figure 4-6 shows processed data of a simulated point target at scene centre using a bistatic angle of 90°, with transmitter and receiver both operating around broadside. The aperture time was 1.024 seconds. There is no weighting applied to the data, so the sidelobe structure appears clearly. Note the non-orthogonal sidelobes, which do not affect the position of the targets, *i.e.* the target configuration remains the same.

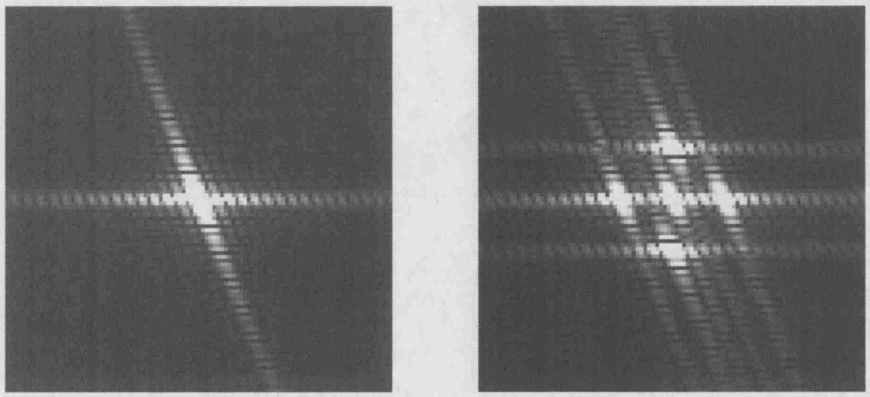

Figure 4-7 Simulated bistatic imagery with 60° bistatic angle

Figure 4-7 shows processed data using a bistatic angle of 60° with both transmitter and receiver working around broadside and an aperture time of 1.024 seconds. It can be seen that using a bistatic angle of 60°, gives sidelobes closer to being orthogonal than the 90° bistatic angle.

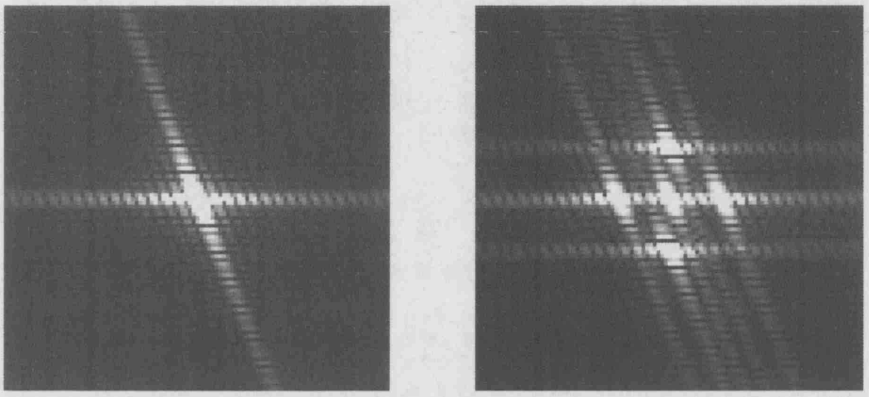

Figure 4-8 Simulated squinted bistatic imagery with 60° bistatic angle

Figure 4-8 shows the results obtained by processing simulated raw data using a bistatic angle of 60° with an aperture time of 1.024 seconds, the receiver working around broadside and the transmitted squinted by -15°. This shows that platform squint has little effect on the image.

4.3.2 Comparison with previous theory

In order to be able to measure the resolution of these images, they must first be interpolated so that the sidelobes are orthogonal. The imagery is in (x,y) coordinates, this must be transformed into (u,v) coordinates by inverting the coordinate transformation described in equations *(18)* and *(19)*. That is using the coordinate transformation:

$$x = \frac{1}{\cos\theta_u \sin\theta_v - \cos\theta_v \sin\theta_u}\left(v\sin\theta_u - u\sin\theta_v\right) \qquad (29)$$

$$y = \frac{1}{\cos\theta_u \sin\theta_v - \cos\theta_v \sin\theta_u}\left(u\cos\theta_v - v\cos\theta_u\right)$$

where:

$$\theta_u = \arctan\left[-\frac{v_T \cos\alpha_0 / TR_{0T} + v_R \cos\beta_0 / TR_{0R}}{v_T \sin\alpha_0 / TR_{0T} + v_R \sin\beta_0 / TR_{0R}}\right], \qquad (30)$$

$$\theta_v = \frac{\alpha_0 + \beta_0}{2}$$

and α_0 is the angle from the positive x-axis to the middle of the transmitter's aperture, β_0 is the angle from the positive x-axis to the centre of the receiver's aperture, T is the aperture time and v is the platform velocity.

Applying the geometry used to produce Figure 4-6, $\theta_v = -\pi/2$ radians and θ_u =0.588 radians. Substituting these theta angles into the coordinate transformation given in equation *(29)* and applying it to the images shown in Figure 4-6 produces the orthogonal images shown in Figure 4-9. In each of these interpolated images the u-axis is horizontal and the v-axis is vertical.

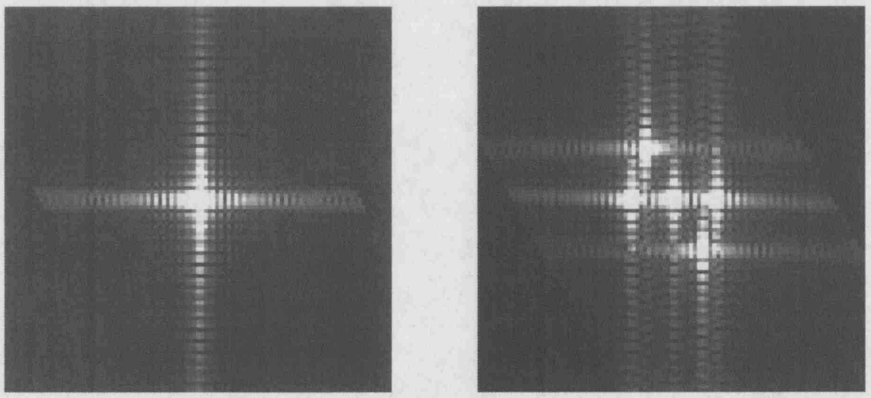

Figure 4-9 Interpolated simulated bistatic imagery with 90° bistatic angle

Analytical expressions for the resolutions in the u and v dimensions have been formulated in the previous section. These were found to be:

$$\rho_u = \frac{c}{Tf_0\sqrt{\left[\frac{v_T^{\,2}}{R_T^{\,2}} + \frac{v_R^{\,2}}{R_R^{\,2}} + \frac{2v_T v_R}{R_T R_R}\cos(\alpha_0 - \beta_0)\right]}}, \qquad \rho_v = \frac{c}{2\Delta f \cos\left(\frac{\alpha_0 - \beta_0}{2}\right)} \tag{31}$$

This gives a theoretical resolution in this example of ρ_u = 0.287m and ρ_v = 0.424m.

Measuring the -3dB resolution of the orthogonal image shown in Figure 4-9 gives values of 0.27m in the u-direction and 0.37m in the v-direction. In order to compare these -3dB values with those obtained from the theory (zero-to-null), they must be divided by a factor of 0.89, see Appendix B. This gives the resolution from the simulation as (0.30m, 0.41m) (note vector notation for resolution given as (u-resolution, v-resolution)). These values have been obtained by measuring them from the image and are subject to measurement errors. Noting this, the resolution obtained from the simulation is very close to that from the theory.

Applying the same theory to the geometry used to generate Figure 4-7 gives $\theta_v = -\pi/2$ radians and $\theta_u = 0.368$ radians. Using these values of θ give the coordinate transformation required in the interpolation to make the axes orthogonal. The results of applying this transformation can be seen in Figure 4-10.

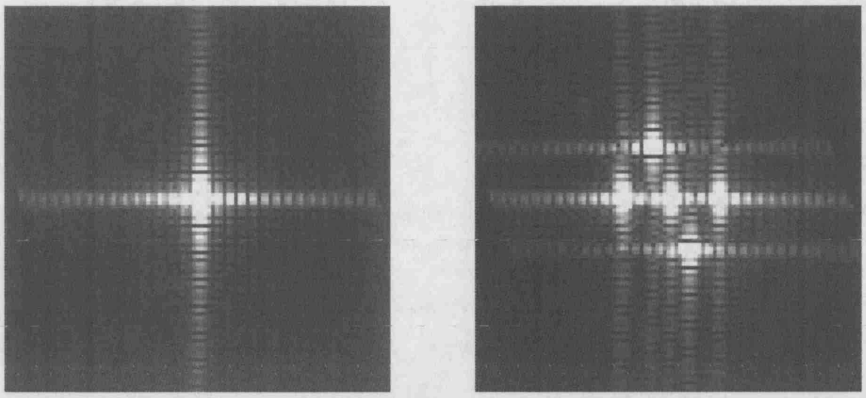

Figure 4-10 Interpolated simulated bistatic imagery with 60° bistatic angle

The analytical expressions for the resolution yields a theoretical resolution of $\rho_u = 0.263$m and $\rho_v = 0.346$m. Measuring the zero-to-null resolution from the orthogonal image shown in Figure 4-10 gives a resolution from the simulated image as (0.26m, 0.35m). These values are in agreement with those obtained from the theory.

Applying the theory to the geometry used for Figure 4-8, gives $\theta_v = -\pi/2$ radians and $\theta_u = 0.372$ radians. On closer inspection of the simulated raw data, it was seen that although the data was generated for 1.024 seconds, a return from the target was only within the data for 0.585 seconds, and it is this value for the aperture time which should be used. Substituting these values of θ into the coordinate transformation given in equation *(29)* produces the required interpolation to make the axes orthogonal. The results of applying this transformation can be seen in Figure 4-11.

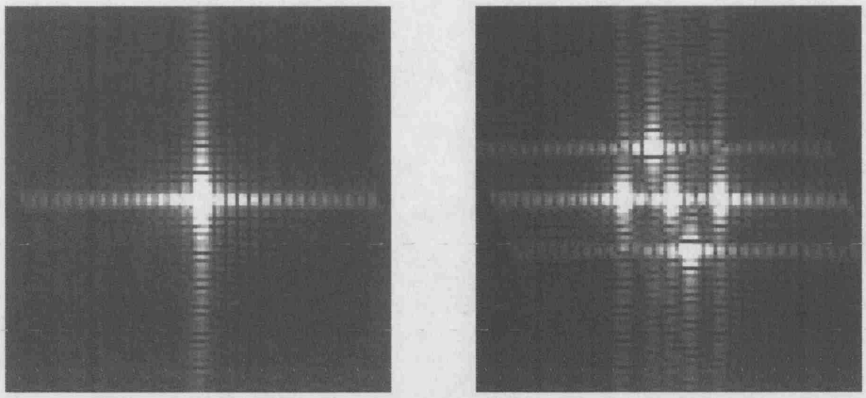

Figure 4-11 Interpolated simulated squinted bistatic imagery with 60° bistatic angle

Substituting the values obtained for the shorter length aperture into the analytical expressions for resolution gives $\rho_u = 0.461\text{m}$ and $\rho_v = 0.346\text{m}$. Measuring the zero-to-null resolution from the orthogonal image gives (0.44m, 0.34m). These values obtained are comparable to those from the theory.

4.3.3 Conclusions

The results of these simulations agree with the theory developed in the previous section, within the bounds of measurement errors. This has verified both the theory of bistatic SAR resolution and the raw data generation program.

This is a processor in its simplest form. It works accurately, but is computationally inefficient. To create a system that is operationally viable, faster image processing is required. For this reason, the adaptation of existing processing algorithms used in monostatic SAR need to be investigated and adapted for the bistatic case.

Chapter 5. Polar Format Algorithm (PFA)

5.1 Introduction

Using spotlight SAR gives the opportunity for long synthetic apertures and therefore fine azimuth resolution. Increasing the azimuth resolution causes problems with motion through resolution cells (MTRC). The polar format algorithm (PFA) partially corrects for the MTRC problem by storing the return from successive pulses along radial lines (*i.e.* in polar coordinates) instead of parallel lines, 28. This requires a 2D (or two 1D) interpolation to resample the data into a rectilinear grid.

Before the PFA interpolation can be applied, the raw data must be in the spatial-frequency domain. This requires some modification of the raw data prior to the 2D PFA interpolation. A summary of the whole PFA process can be seen in Figure 5-1.

Initial work looked at adapting the 'pre' and 'post' processing aspects of the algorithm. Namely, changes to the range curvature correction, azimuth dechirp and output sample spacing elements. The results of the adaptations are presented first.

Work then continues to look at the critical PFA processing engine. The work presented here examines three different bistatic adaptations of the polar format algorithm itself. In each case, the theory behind the method has been

implemented in mathematical packages to give a theoretical measure of scene size. These adaptations have also been implemented into a simulation and used to process synthesised raw data.

The effects of altitude have been included in the later simulations. The results from this have been examined for different geometries and different grazing angles to quantify the effects of out-of-plane motion on scene size limitations.

PFA is only one possible processing engine. It has known and well documented limitations, the most significant being the limitations it imposes on scene size. It is developed here only as a fall back option, if more advanced methods (developed later in this thesis) fail.

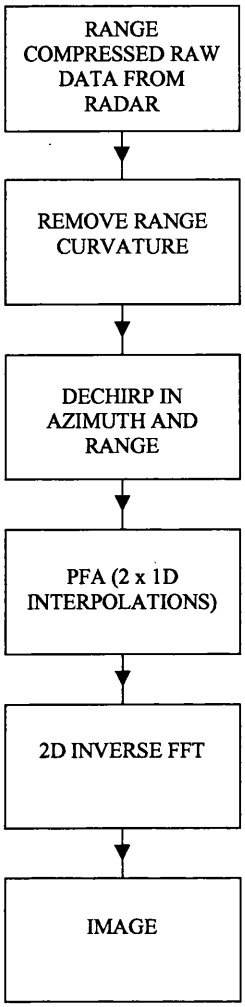

Figure 5-1 Polar Format Algorithm

5.2 Pre-processing elements

5.2.1 Algorithm development

From a detailed examination of the PFA it was possible to note where the changes to the pre-processing would have to be made to adapt it for a bistatic system. These were namely the range curvature correction and the azimuth dechirp.

The two dimensional monostatic range to the scene centre is given by the quadratic equation:

$$R = \sqrt{(x_s + X\cos(\Delta))^2 + (y_s + X\sin(\Delta))^2} \qquad (32)$$

where (x_s, y_s) is the start position of the radar

X is the length the radar has moved along the aperture (X=0 at the start of recording)

Δ is the angle that the aircraft's flight path makes with the positive x-axis) as demonstrated in Figure 5-2.

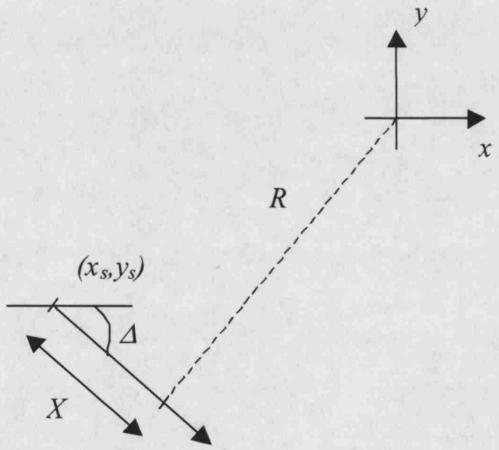

Figure 5-2 Monostatic range equation

The distance travelled by the radar signal when it reaches the receiver via a target at scene centre is therefore given by $2R$.

In the bistatic case, the range to the scene centre has two parts, namely, that from the transmitter to the scene centre and then from the scene centre to the

receiver. Each of these ranges vary quadratically as a function of platform position (*i.e.* aperture time). The range curvature across the raw data will remain quadratic with platform motion as in the monostatic case. However, in the bistatic case it will be the result of adding together two quadratics, one gained from the transmitter's motion the other from the receiver.

In the existing PFA program, the range-curvature correction function requires the input of the range to the scene centre as a function of position along aperture. From the platform's start position, its velocity and the time along the aperture, each platform's exact position can be calculated. From this, the range to the scene centre from each platform is easily calculated. These are summed to give the full distance that the signal will travel from transmitter to receiver via scene centre. For consistency with the monostatic case, this range has to be halved.

The bistatic range to scene centre is given by:

$$R_t = \sqrt{\left(x_{sT} + \frac{v_T}{v_R} X\cos(\Delta_T)\right)^2 + \left(y_{sT} + \frac{v_T}{v_R} X\sin(\Delta_T)\right)^2} + \sqrt{(x_{sR} + X\cos(\Delta_R))^2 + (y_{sR} + X\sin(\Delta_R))^2} \qquad (33)$$

where the subscript T denotes that the variable relates to the transmitter and the subscript R denotes that the variable relates to the receiver. The only additional information required is the speed of the platforms which are denoted by the letter v.

The azimuth dechirp consists of multiplying the data by the conjugate of the expected signal return from the scene centre. In the bistatic case, this will be a

function of both platforms' motion and the only adaptation required was the definition of range to the scene centre as described above.

5.2.2 Results and comparisons with previous theory

In all cases the scene is square in dimensions, but the spacing is unequal so the image appears as a rectangle. An input to the program is the x-resolution. In most cases, (the only exception being Figure 5-3) that value was entered as 0.3m. The output image appears in u-v space with the u-axis horizontal and the v-axis vertical. This is due to the way the window is cut out of the K-space annulus. Since a uniform rectangle is inscribed out of the data, the resulting image will have orthogonal sidelobes.

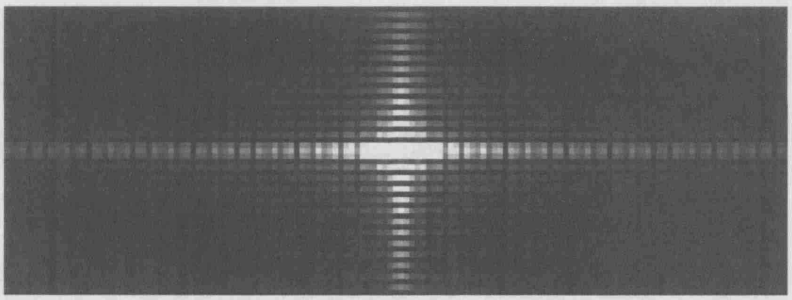

Figure 5-3 Simulated bistatic imagery with 90° bistatic angle

Figure 5-3 shows the output from the PFA processor using the same geometry as in Figure 4-6 from the point-by-point processor *i.e.* a bistatic angle of 90° with both the transmitter and receiver working around broadside. From the theory the 'best' achievable resolutions are given by $\rho_u = 0.14$m and $\rho_v = 0.42$m. Here, the requested resolution in the horizontal direction (*i.e.* u-direction) was 0.3m. Measuring the zero-to-null resolution of the image in Figure 5-3 (0.30m, 0.29m). The measured resolution in the u-direction is the

same as the value of 0.3m that was requested. The value 0.29m for the *v*-direction appears incorrect. However, from the theory, the effective monostatic bandwidth is given by $B_{eff}=\Delta f\cos((\alpha_0-\beta_0)/2)$, where Δf is the bistatic bandwidth. The image pixel spacing the *v*-direction needs to be scaled by this value. Taking the measured value of resolution and dividing it by a factor of $\cos((\alpha_0-\beta_0)/2)$ *i.e.* cos(-45.0°) gives a resolution in the *v*-direction of 0.41m (known as the bistatic correction in later paragraphs). This value is very close to the theoretical value of 0.42m.

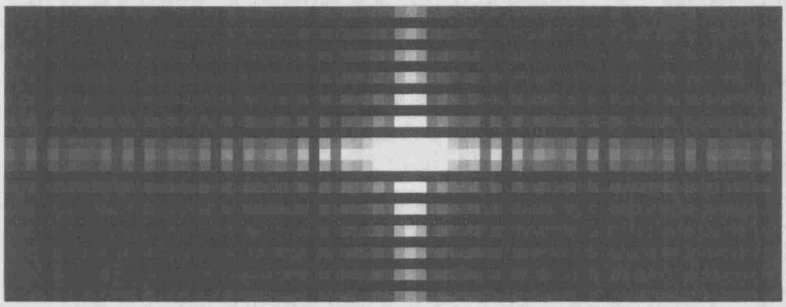

Figure 5-4 Simulated bistatic imagery with 90° bistatic angle

Figure 5-4 has the same bistatic geometry as Figure 5-3. The only difference is the value of the requested horizontal resolution entered into the PFA program. In this example, a value of 0.5m was used. The zero-to-null resolution (including the bistatic correction) measured from the image is (0.49m, 0.41m). The value of the resolution in the *v*-direction remains unchanged (as is expected), while the value in the *u*-direction increases to be very close to the requested value of 0.5m.

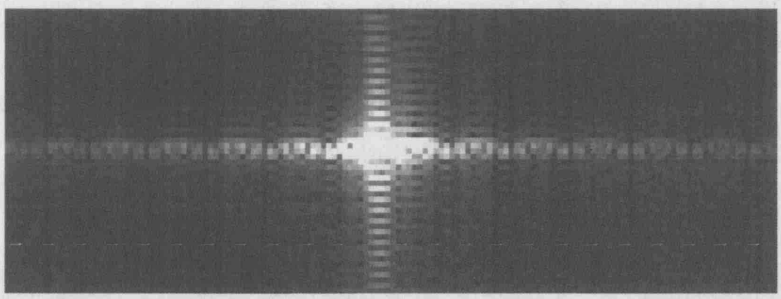

Figure 5-5 Simulated squinted bistatic imagery with 90° bistatic angle

Figure 5-5 shows the output from the PFA processor with a bistatic angle of 90°, with the receiver working around broadside and the transmitter squinted by 15°. From the theory the minimum attainable resolution is given by $\rho_u = 0.14$m and $\rho_v = 0.42$m. Measuring the zero-to-null resolution from Figure 5-5 and applying the bistatic correction gives (0.31m, 0.43m). The value for the u-direction is very similar to the value of 0.3m requested. The corrected value in the v-direction is very close to the theory. The positioning on the point target in the image does not appear to be central horizontally.

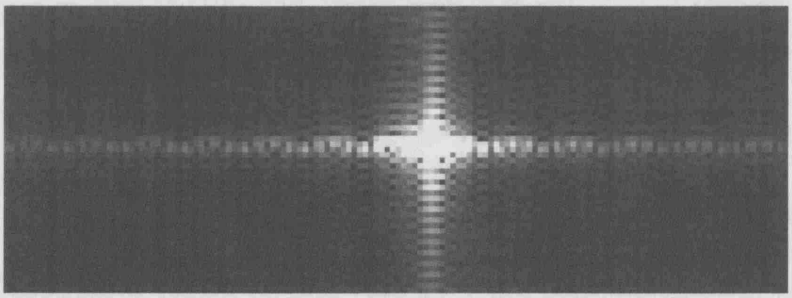

Figure 5-6 Simulated bistatic imagery with 90° bistatic angle

Figure 5-6 shows the output from the PFA processor with a bistatic angle of 90°, with the transmitter working around broadside and the receiver squinted by -15°. From the theory the minimum attainable resolution is given by $\rho_u = 0.15$m and $\rho_v = 0.42$m. Measuring the corrected zero-to-null resolution gives (0.31m,

0.42m). This value for the u-direction is very similar to the value of 0.3m requested, the value in the v-direction is very close to the theoretical value of 0.42m.

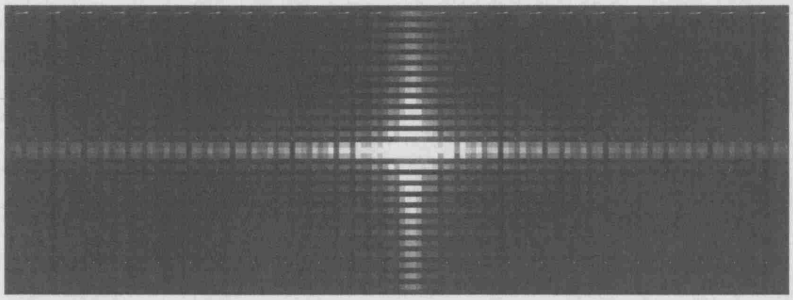

Figure 5-7 Simulated bistatic imagery with 60° bistatic angle

Figure 5-7 shows the output from the PFA processor with a bistatic angle of 60°, with both the receiver and the transmitter working around broadside. Applying the theory to this geometry gives the best obtainable resolution being $\rho_u = 0.13$m and $\rho_v = 0.35$m. Measuring the corrected zero-to-null resolution from Figure 5-7 gives (0.30m, 0.34). This value in the u-direction is the same as the value of 0.3m that was requested, the value in the v-direction is very similar to the value given by the theory.

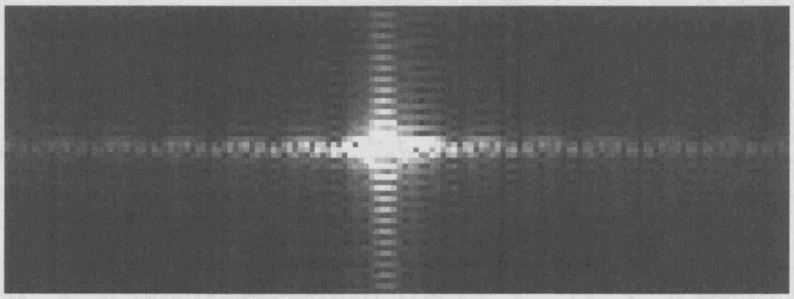

Figure 5-8 Simulated squinted bistatic imagery with 60° bistatic angle

Figure 5-8 shows the output from the PFA processor with a bistatic angle of 60°, with the transmitter working around broadside and the receiver squinted by

15°. Applying the theory to this geometry gives the best obtainable resolution being $\rho_u = 0.14$m and $\rho_v = 0.35$m. Measuring the zero-to-null resolution from Figure 5-8 gives (0.31m, 0.35m). This value in the *u*-direction is very close to the value of 0.3m requested, the resolution in the *v*-direction agrees with the value given by the theory. Again as with the previous squinted image, the position of the point target seems to be displaced horizontally in the image.

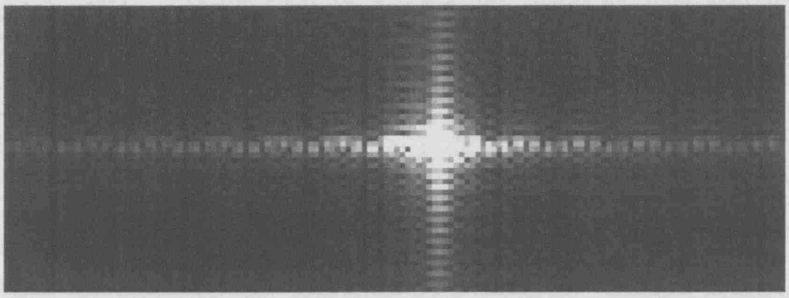

Figure 5-9 Simulated squinted bistatic imagery with 60° bistatic angle

Figure 5-9 shows the output from the PFA processor with a bistatic angle of 60°, with the receiver working around broadside and the transmitter squinted by -15°. Once again, applying the theory to this geometry gives the best obtainable resolution being $\rho_u = 0.13$m and $\rho_v = 0.35$m. Measuring the corrected zero-to-null resolution from Figure 5-9 gives (0.31m, 0.35m). This value in the *u*-direction is very close to the value of 0.3m that was requested, the value in the *v*-direction is the same as that given by the theory. As with the previous squinted example the position of the point target seems to be displaced horizontally.

5.2.3 Conclusions

The pre-processing elements of PFA have been adapted for bistatic geometries. These adaptations have been shown to produce the resolution at scene centre

(where PFA is exact) that the theory in Chapter 3 predicts. The limitation in scene size (arising from PFA being based on the incorrect assumption of planar wavefronts) will be investigated later in this chapter. There also appears to be a problem with the point target wandering horizontally when squinted bistatic geometries are introduced.

5.3 Modification of the polar format processing algorithm

In section 5.2, the modifications to the range curvature, azimuth dechirp and output image re-sampling elements of the PFA process were explored. This section looks at the adaptation of the polar reformat interpolation itself for bistatic operation.

This section looks at three different ways of extending the monostatic polar interpolation for bistatic use. Each method has been implemented from a theoretical point of view using mathematical computer packages and by implementing it into a new PFA simulation. They were each tested under three different scenarios. The first was a monostatic geometry, the second was bistatic with equal angular velocity (in this case equal speed and stand off range), the third case was a generic bistatic one. In this latter case, the transmitter and receiver are always flying at the same speed, but at different ranges. In all cases, the platforms are working around broadside. The theoretical resolutions and simulation results are presented in section 5.3.4.

An additional adaptation, not considered here, is given in [25]. This recent work provides a PFA for bistatic SAR. This paper along with [26] should provide useful insight into the bistatic PFA.

5.3.1 Tangents to ellipse method

A natural extension of the monostatic PFA is taken from the planar wavefronts approximation. Monostatically, PFA stores the return from successive pulses along radial lines. Another, identical, way of visualising this is by storing successive pulses along the tangent to the iso-range circle passing through the scene centre. In the bistatic extension, these lines of iso-range are ellipses with the platforms as the foci. This extends the monostatic interpretation to storing the returns from successive pulses along the tangents to iso-range ellipses at the scene centre.

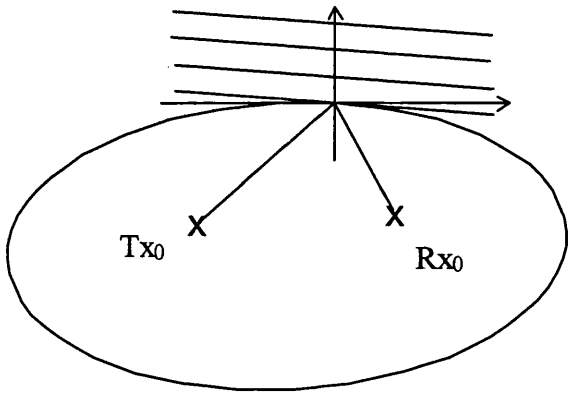

Figure 5-10 The ellipse geometry

A generic expression for an ellipse with arbitrary foci passing through scene centre has been developed in Appendix B. From this, an equation for the gradient of this ellipse at the scene centre has been obtained, equation *(34)*. This value is calculated at every step of platform position and the data from that pulse is stored along it.

$$\text{gradient} = \frac{\alpha_0 b}{a\sqrt{a^2 - \alpha_0^{\,2}}}, \qquad (34)$$

where a is half the total path length to scene centre *i.e.* $a = \frac{R_T + R_R}{2}$, c is half the distance between platform positions (foci), $c = \sqrt{\left(\frac{x_T - x_R}{2}\right)^2 + \left(\frac{y_T - y_R}{2}\right)^2}$, $b = \sqrt{a^2 - c^2}$, $\alpha_0 = \left(\frac{x_T + x_R}{2}\right)\cos\theta - \left(\frac{y_T + y_R}{2}\right)\sin\theta$ and $\theta = \arctan\left(\frac{y_T - y_R}{x_T - x_R}\right)$.

5.3.2 Half bistatic angle approach

Another way of extending PFA for bistatic use is suggested in reference 30. This suggests that the bisector of the instantaneous bistatic angle can be used as an equivalent monostatic projection. This stores the return from successive pulses along the 'instantaneous' v-axes demonstrated in Figure 5-11. The instantaneous bistatic angle is given by:

$$\beta_I = \arctan\left(\frac{x_R}{y_R}\right) + \arctan\left(\frac{x_T}{y_T}\right) \qquad (35)$$

where (x_R, y_R) is the instantaneous position of the receiver and (x_T, y_T) is the instantaneous position of the transmitter

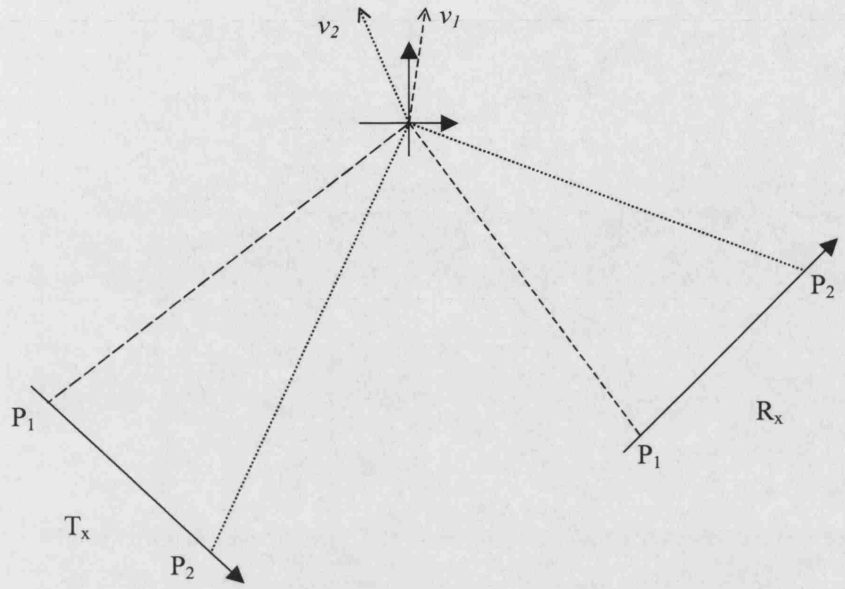

Figure 5-11 Half bistatic angle geometry

The results from both of these methods, demonstrated in section 5.3.4, are shown to be unacceptable in terms of scene size limitations. This provoked a requirement for the development of a completely novel approach.

5.3.3 Mathematical approach

This method has been developed by Andrew Horne. This technique has been developed from a mathematical approach, as opposed to a physical one. The details of which can be found in reference [29]. The results from this work have been integrated into the bistatic SAR simulation code developed here. For the purpose of this thesis, only the results of the simulation code are presented here for comparison with the methods described previously.

5.3.4 Results and comparisons

In each of these cases, a theoretical value of the resolution of a target offset from scene centre was calculated using mathematical computer packages. These methods were also implemented into a simulation. This involved creating synthesised raw data and passed it through the whole PFA process as described in Figure 5-1.

The three PFA modifications are:

1. Ellipse
2. Half bistatic angle
3. Novel mathematical approach

Three test geometry cases:

A. monostatic- around broadside with a slant range of 2km,

B. equal angular momentum- both platforms around broadside each with a slant range of 2km, equal speed and a bistatic angle of 90°,

C. a generic bistatic geometry- both platforms around broadside with the transmitter slant range of 10km, receiver slant range of 2km, both with equal speed and a bistatic angle of 90°.

Initially in each of these cases very low grazing angle is assumed, *i.e.* platform heights are zero. It was assumed that a phase error of $\pi/2$ would cause an unacceptable degradation in resolution, as inferred on page 136 of reference

[28]. The theory column in each of the tables below shows the displacement of a target in the u-direction with a phase error of $\pi/2$. The simulation has been run with point targets placed at multiples of 100m in the u-direction (with the exception of a few cases where targets are placed closer together). In all cases, a resolution of 0.3m in both dimensions was expected. Only values of resolution are quoted, in vector notation, when the resolution shows a significant degradation. The position of the target from scene centre is also given.

Method 1.

Case	Theory	Simulation	
A	182m	100m (0.310m,0.298m)	200m (0.801m,0.298m)
B	334m	300m (0.299m,0.298m)	400m (0.334m,0.298m)
C	8.5m	0m (0.301m,0.298m)	10m (0.342m,0.298m)

Table 5-1 Scene limitations using the ellipse method

Method 2

Case	Theory	Simulation	
A	182m	100m (0.310m,0.298m)	200m (0.801m,0.298m)
B	334m	300m (0.310m,0.298m)	400m (0.335m,0.298m)
C	12.2m	0m (0.302m,0.298m)	10m (0.342m,0.298m)

Table 5-2 Scene limitations using the half bistatic angle method

Method 3

Case	Theory	Simulation	
A	174m	100m (0.299m,0.297m)	200m (0.790m,0.297m)
B	450m	400m (0.318m,0.297m)	500m (0.488m,0.301m)
C	137m	100m (0.295m,0.297m)	200m (0.372m,0.297m)

Table 5-3 Scene limitations using the mathematical method

In all cases and all methods, the simulations agree broadly with the theory. For the monostatic and equal angular momentum cases (A and B), all three methods have similar results. In fact, it can be shown numerically that methods 1 and 2 are identical in these two cases. In the generic bistatic case there is a very marked difference in scene size. In this case, the ellipse and half bistatic angle

methods have different results (more noticeably in the theory). However, they are still both similar and extremely poor having a scene radius of around ten metres. This would make them unacceptable methods to process bistatic data. The novel mathematical approach allows a larger scene size by an order of magnitude. For the case shown, a scene diameter of over 250 metres is achievable.

For all methods the equal angular momentum case allows a larger scene size than the monostatic case. This was not unexpected. This is because there is less curvature of the raw data in the simple bistatic case than in the monostatic case.

5.4 Introducing altitude

So far, the work on the bistatic PFA algorithm has made the assumption that both platforms are operating at zero altitude. This simplified the bistatic geometry by putting the whole problem, including the scene, the image, both platforms and their velocity vectors, within a single plane. The introduction of altitude in the monostatic case does not fundamentally complicate the problem for the processing engine. In bistatic processing, platform height is likely to introduce problems of large out-of-plane motions. Figure 5-12 shows the problem in the more general case. The natural reference plane to use is probably that which includes the scene centre and the aperture centres of transmit and receive platforms. However, it is clear that neither the transmit platform, T, or the receive platform, R, will be within the plane except at the centre of the aperture.

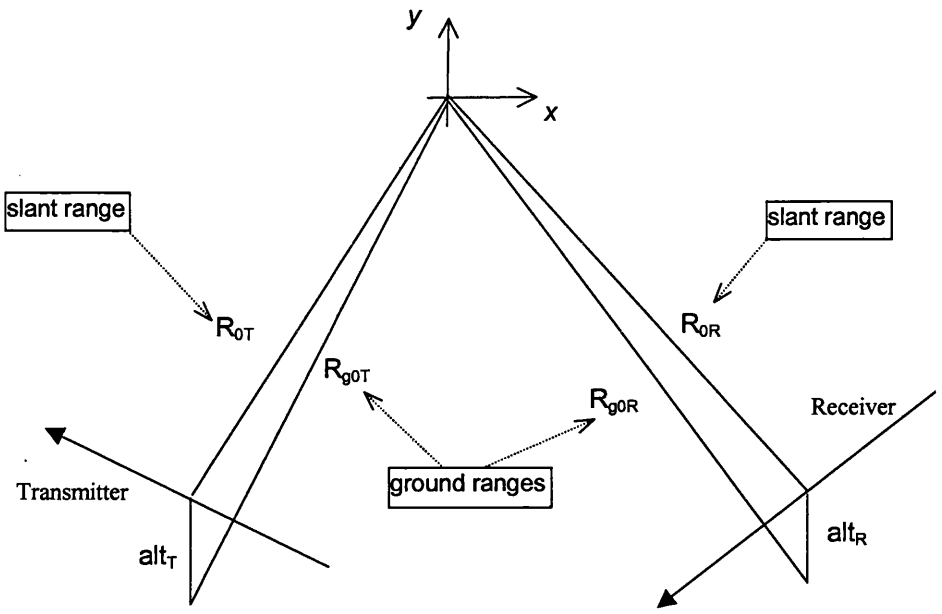

Figure 5-12 Introducing altitude

Including altitude in the process uses the same PFA processing code as in the 2D case. However, the ranges calculated in the pre-processing code for correcting range curvature and azimuth dechirping need to be altered to include altitude. Now the range becomes:

$$r = R_{0T}\left(1-\frac{2v_t t\sin\theta_t}{R_{0T}}+\frac{v_t^2t^2+alt_T^2}{R_{0T}^2}\right)^{\frac{1}{2}}+R_{0R}\left(1-\frac{2v_r t\sin\theta_r}{R_{0R}}+\frac{v_r^2t^2+alt_R^2}{R_{0R}^2}\right)^{\frac{1}{2}} \qquad (36)$$

From the previous results, it is clear that the novel mathematical approach developed here is the best method, by far, for both bistatic cases. Therefore, it is this method that is used to investigate the inclusion of altitude. Note that the targets are now displaced in the x direction, where in the previous section targets were displaced in u. In cases A and B this is the same as before, u=100m translates to x=100m, in case C u=100m translates to x=83.2m.

Method 3, case A:

Altitude	Simulation		
1000m	0m (0.299m,0.297m)	100m (0.299m,0.297m)	200m (0.790m,0.297m)
0m	0m (0.297m,0.297m)	100m (0.299m,0.297m)	200m (0.790m,0.297m)

Table 5-4 Effects of altitude in the monostatic case

Method 3, case B:

Altitude	Simulation			
Rx 1000m Tx 1000m	100m (0.299m,0.297m)	200m (0.302m,0.297m)	300m (0.376m,0.297m)	
Rx 0m Tx 1000m	100m (0.299m,0.297m)	200m (0.301m,0.297m)	300m (0.310m,0.297m)	400m (0.700m,0.297m)
Rx 1000m Tx 0m	100m (0.299m,0.297m)	200m (0.300m,0.297m)	300m (0.320m,0.297m)	
Rx 0m Tx 0m	100m (0.299m,0.297m)	200m (0.299m,0.297m)	300m (0.301m,0.297m)	400m (0.318m,0.297m)

Table 5-5 Effects of altitude in the equal angular momentum case

Method 3, case C:

Altitude	Simulation		
Rx 1000m Tx 5000m	0m (0.299m,0.297m)	100m (0.942m,0.298m)	200m (2.90m,0.298)
Rx 1000m Tx 1000m	0m (0.299m,0.297m)	100m (0.326m,0.298m)	200m (1.38m,0.298m)
Rx 0m Tx 5000m	0m (0.299m,0.297m)	100m (0.768m,0.298m)	200m (2.49m,0.298m)
Rx 0m Tx 1000m	0m (0.299m,0.297m)	100m (0.297m,0.298m)	200m (0.914m,0.297m)
Rx 1000m Tx 0m	0m (0.299m,0.297m)	100m (0.322m,0.298m)	200m (1.32m,0.297m)
Rx 0m Tx 0m	0m (0.299m,0.298m)	100m (0.290m,0.297m)	200m (0.804m,0.298m)

Table 5-6 Effects of altitude in the generic bistatic case

It was expected that the out of plane motion of the two aircraft would cause a degradation in scene size. This is shown in these simulations. In case A (the monostatic case) altitude makes no difference. This is due to the platform and the targets being in the same plane, altitude just has the effect of tilting this plane. In cases B and C (the bistatic ones) the largest scene size is from the case when both aircraft are at zero altitude. In case B, with either the transmitter at an altitude or the receiver at the same altitude (or grazing angle) gives similar scene sizes. When both the transmitter and receiver are at altitude, the scene size degrades further. In case C, the zero altitude example gives by far the best

result. Both platforms flying at the same grazing angle (row 1 of Table 5-6) or altitude (row 2 of Table 5-6) does not seem to increase the scene size. Both aircraft at high grazing angles produces the worst result.

5.5 Illustration of PFA simulations

To illustrate the bistatic PFA processor further, a piece of a monostatic processed radar image has been used as a mock 'scene'. This has been imaged bistatically using the raw data simulator. The bistatic geometry used in this case was a bistatic angle of 90° with both transmitter and receiver working around broadside. Figure 5-13 shows the original piece of processed radar data used as the scene, while Figure 5-14 shows the output image from the PFA processor from the bistatic raw data. This image was then interpolated to give the image in Figure 5-15.

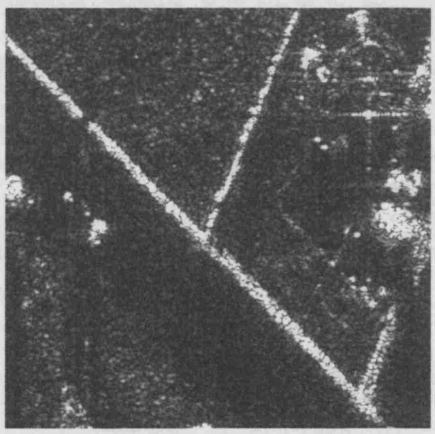

Figure 5-13 Monostatic image used as scene, range vertically azimuth horizontally

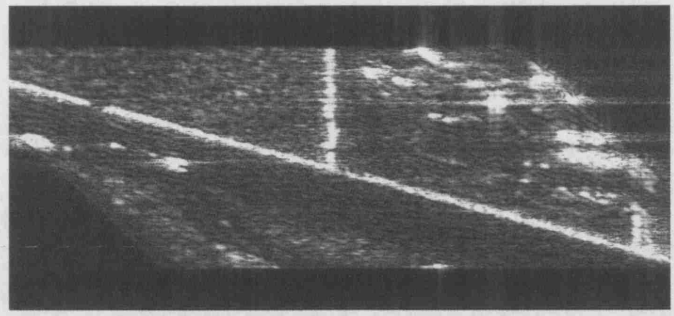

Figure 5-14 Output from PFA displayed in u-v frame (u horizontally, v vertically)

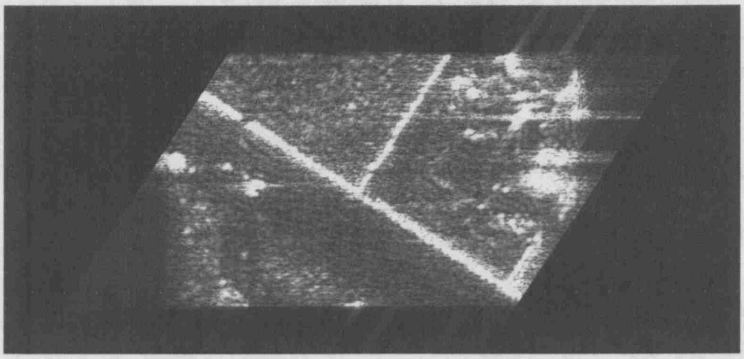

Figure 5-15 Output from PFA interpolated into original image frame (x,y)

5.6 Conclusions

The PFA interpolation part of the process has been adapted for bistatic use. This thesis looks at the results from three different approaches for this and compares them in terms of scene size limitations. The novel mathematical approach developed by Andrew Horne has been shown to be far superior to the other methods tested here.

The inclusion of altitude in the problem has been addressed. The resulting out-of-plane motion has produced tighter constraints on scene size, as expected. The radius of an acceptable scene has decreased from approximately 150m to 50m

in some cases. Although this would be limiting, this section shows that PFA is a viable option for bistatic operation.

The scene size limitation is a known drawback of PFA. This leads us to look at a more advanced processing algorithm, namely the Range Migration Algorithm (RMA).

Chapter 6. Range Migration Algorithm (RMA)

6.1 Introduction

The main advantage of the RMA is that, unlike PFA, it does not does not suffer from geometric distortions or scene size limitations. This is because it does not assume planar wave fronts.

To understand the complications in adapting RMA for bistatic use, a summary of the monostatic development is presented. Possible ways of finding an approximate form of the bistatic adaptation of the process are examined and their results are presented.

As a simplification, the altitude of both aircraft is set to be zero to remove any out of plane motion effects.

6.2 Algorithm

A summary of the whole RMA process can be found in Figure 6-1. The step that is unique to RMA is the Stolt interpolation. This is a deformation of the signal in the range dimension operating in K-space *i.e.* the (K_x,K_R) domain. It corrects range curvature for scatterers at different ranges. The phase of a scatterer offset in azimuth only (imaged monostatically) is a linear grating after the matched filtering and is unaffected by the Stolt interpolation. This is shown in the left hand graphs of Figure 6-3 and Figure 6-4. Targets offset in range are left with residual range curvature after the matched filtering stage, shown in the

right hand graph of Figure 6-3. The Stolt interpolation straightens the lines of constant phase to form a linear phase grating, Figure 6-4.

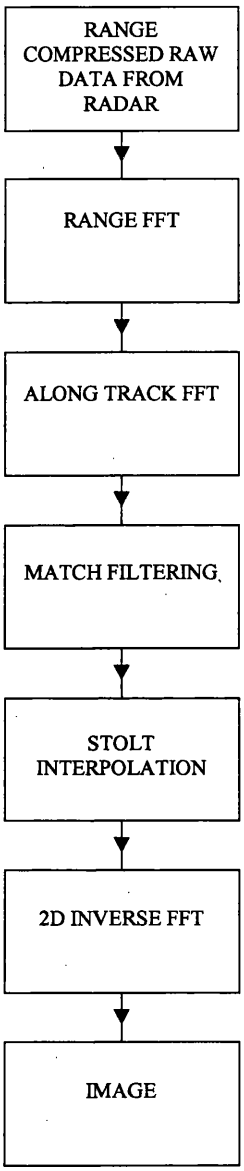

Figure 6-1 Range Migration Algorithm

In the monostatic case, the process is developed using the analytical expression for the phase of the return from a single scatterer. The signal is then Fourier transformed. This stage needs to be approximated using the principle of

stationary phase in order for the Fourier transform integral to be evaluated. The result of this provides the analytical form of the matched filter. From this, an analytical expression of the Stolt interpolation is obtained as:

$$K_Y \rightarrow \sqrt{K_R^{\,2} - K_X^{\,2}}\,. \qquad (37)$$

The full derivation of the monostatic form of RMA is developed in reference [31].

The difficulty in adapting RMA for bistatic use is with the matched filter and Stolt interpolation stages. Where, in the monostatic case, the matched filter is derived from the analytical expression for the along track Fourier transform of the signal, in the bistatic case this expression is too complicated. An exact form (or even an accurate approximation) for the Fourier transform cannot be found. Without this analytical expression, the form of the bistatic 'Stolt' interpolation is unclear.

Knowing the analytical form of the matched filter is not an essential part of the process. This step can be achieved by calculating a raw data image of a scatterer at the scene centre. The matched filter is simply the conjugate of this image in the Fourier domain. The matched filtering process can be completed by multiplying the matched filter image with the Fourier transformed original data. This process is rather cumbersome and is computationally inefficient, but it is exact.

Without the form of the matched filter, the bistatic form of the Stolt interpolation becomes unclear. Work researching the form of the bistatic 'Stolt' interpolation is presented here.

6.3 Bistatic form of 'Stolt' interpolation

An analytic expression for the phase after the application of the bistatic 'Stolt' must be in the form:

$$\phi = K_u u_0 + K_v v_0 . \qquad (38)$$

When it is in this form a simple 2D inverse Fourier transform produces the desired target image. This implies that the phase of a target displaced from scene centre in v only, should have horizontal lines of constant phase after the interpolation. A target displaced in u only should have vertical lines of constant phase. This section looks at the work carried out to find the form of the bistatic 'Stolt' interpolation to transform the phase into this form.

6.3.1 Empirical approach

Initial investigations were focused towards the form of the phase after the match filtering process. Simple interpolations were applied with the aim of achieving the linear form of the phase as described above. The process adopted can be seen in Figure 6-2.

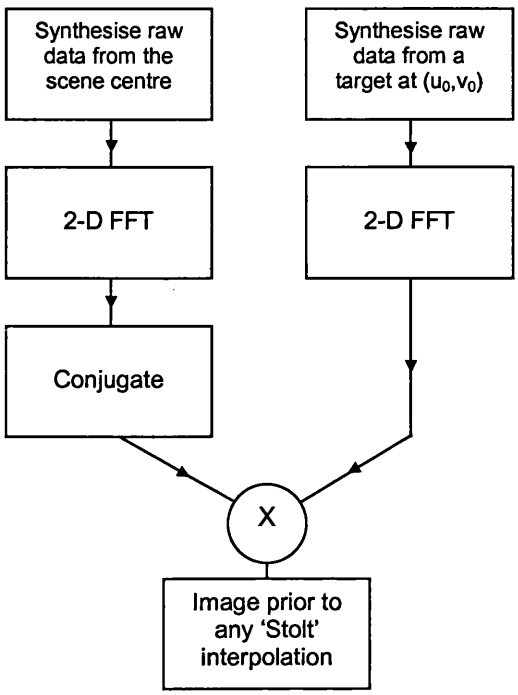

Figure 6-2 Trial and error process

Applying this process to monostatic data produces phase which has a residual curvature for targets displaced in y, but no curvature for targets displaced in x, as seen in Figure 6-3. These graphs show a vertical cross section of the phase for targets displaced in y (and later v) or a horizontal cross section of phase for targets displaced in x (or later u). It is only meant as an aid to see residual phase curvature of different targets at different stages of the process. Where the phase is curved, this curve appears wrapped around and gives the false impression of discontinuities.

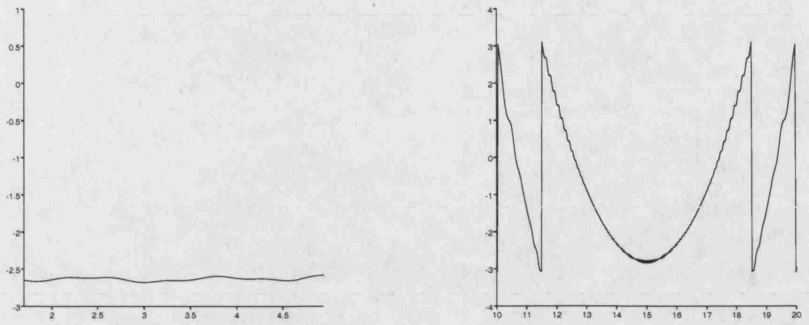

(a) *(b)*

Figure 6-3 Phase after matched filtering of a target displaced in (a) x and (b) y

The Stolt interpolation, as described in equation *(37)*, is applied to the data. As it is intended, it removes the residual curvature in the *y*-direction, while the *x*-direction remains unchanged.

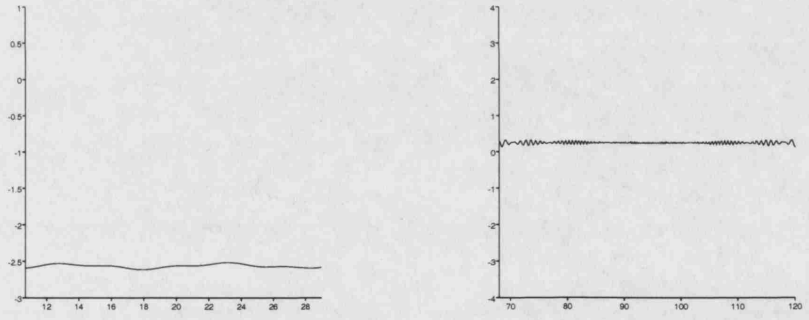

(a) *(b)*

Figure 6-4 Phase after Stolt interpolation of a target displaced in (a) x and (b) y

The next stage was to apply this process to bistatic data where the transmitter and receiver have equal angular momentum around the scene centre. The phase from targets displaced in the *x*-direction only and in the *y*-direction only after the matched filter stage can be seen in Figure 6-5. The phase of the target displaced in *x* appears to have a very slight curvature on it. The phase from the target displaced in *y* has more curvature than in the monostatic case.

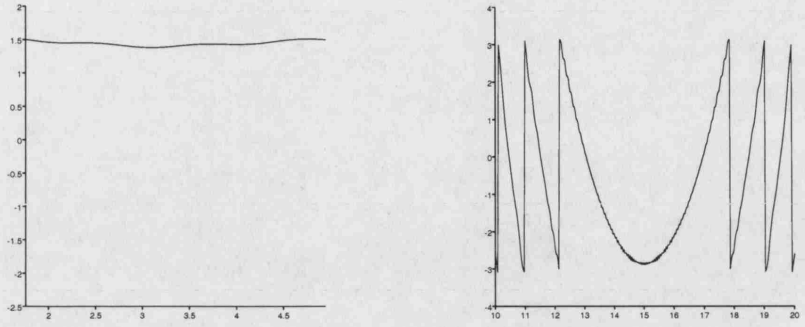

(a) *(b)*

Figure 6-5 Phase from targets displaced in (a) x and (b) y after matched filter stage

Here, it was found that applying the monostatic Stolt interpolation left a very small amount of residual phase curvature for targets displaced in both the *x*-direction and the *y*-direction. This implies that the bistatic form of the Stolt interpolator is probably two-dimensional, although the curvature in the *x*-direction is minimal.

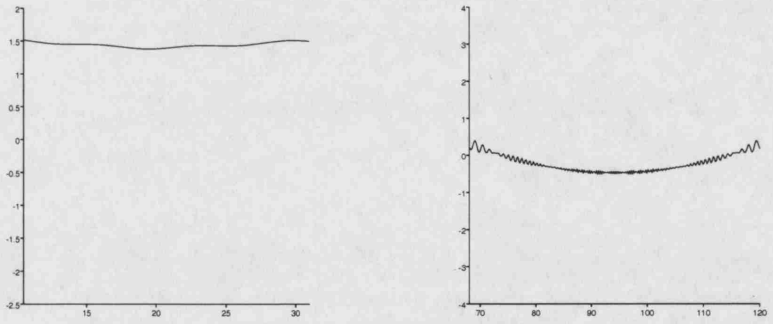

(a) *(b)*

Figure 6-6 Phase after Stolt interpolation of a target displaced in (a) x and (b) y

This slight curvature can be straightened by rescaling along each axis. The amount to rescale the axes by changes for different target locations and different geometries. There is no obvious pattern.

This process has also been applied to the generic bistatic case described on page 68. Although it is clear that the processor should be working in the (u,v) coordinate frame, the process was applied to targets displaced only in each of u, v, x and y. The phase after the matched filter appears to be almost linear for the targets displaced in x or u. However, for a target displaced in y there is considerable curvature on the phase. For a target displaced in v, a similar amount of curvature remains as for the equal angular momentum case. However, the turning point of this curve has moved from the centre of the data. These results are demonstrated in Figure 6-7 and Figure 6-8.

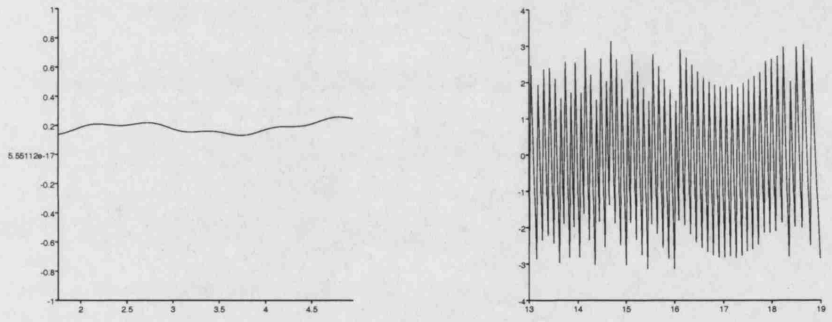

(a) *(b)*

Figure 6-7 Phase after matched filtering for a target displaced in (a) x and (b) y

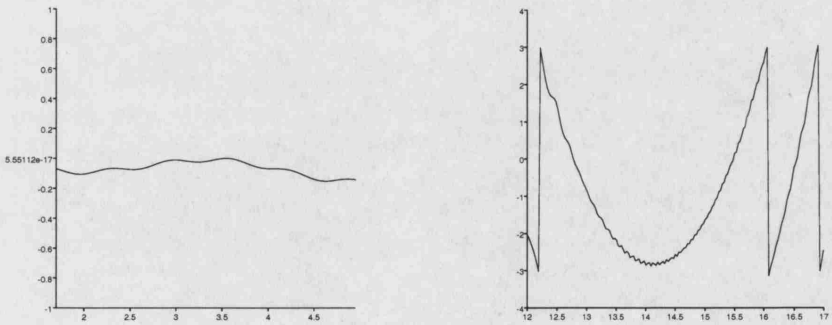

(a) *(b)*

Figure 6-8 Phase after matched filtering for targets displaced in (a) u and (b) v

The next stage was to apply the monostatic Stolt interpolation to this data and examine the residual curvature after it. This had the effect of moving the data support. A linear shift has been included in order to record the data. The phase of a target displaced in u or x remains unchanged. The phase of a target displaced in y changes rapidly throughout the image. The effect of this 'Stolt' interpolation on the phase of a target displaced in v remains curved, although the turning point of the curve has moved. These results are demonstrated in Figure 6-9 and Figure 6-10.

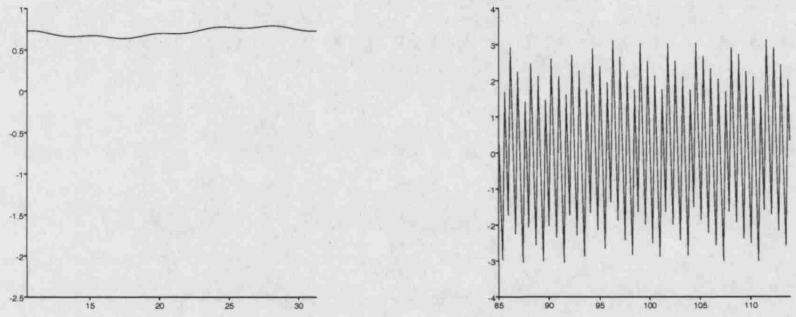

(a) *(b)*

Figure 6-9 Phase after Stolt interpolation for a target displaced in (a) x and (b) y

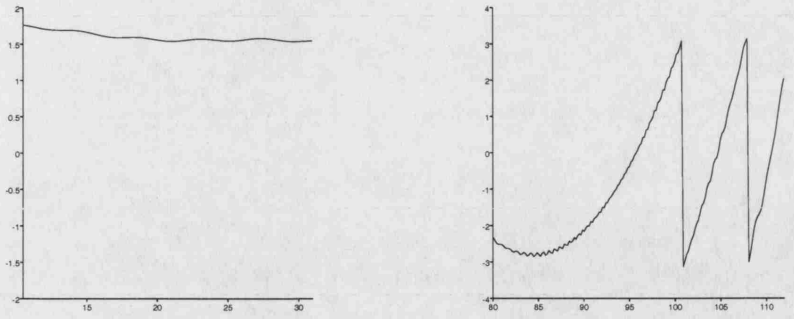

(a) *(b)*

Figure 6-10 Phase after Stolt interpolation for targets displaced in (a) u and (b) v

The matched filter image was then distorted using prior knowledge of bistatic work. This included a transformation in the u and v coordinates as well as the scaling of K_R to include a factor of $\cos(\beta/2)$. For targets close to scene centre, the phase appeared straight although not with the desired gradient, Figure 6-11. Applying a simple rotation to the data solved this. However as the target was moved further away from the scene centre the curvature of the phase at the extremes of the data became more significant, as shown in Figure 6-12. It is clear that this is not a solution to the problem.

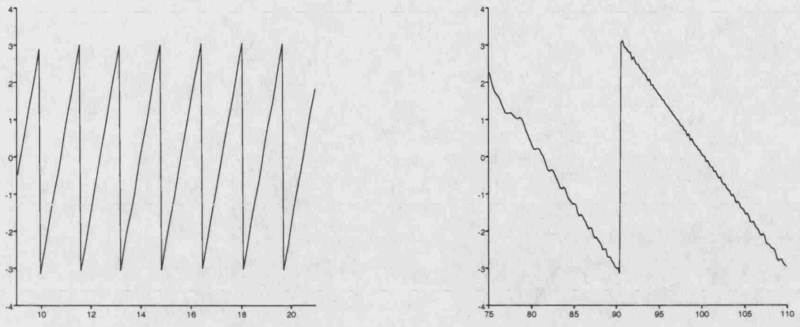

(a) *(b)*

Figure 6-11 Phase after (u,v) transformation of a target displaced 10m in (a) x and (b) y

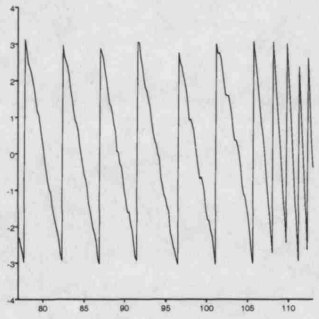

Figure 6-12 Phase after (u,v) interpolation of a target displaced 30m in y the direction

Through this study, it became clear that it was not possible to simply extract the form of the 'Stolt' interpolation from the form of the phase after matched filtering. A more systematic approach was needed. However, some conclusions could be drawn:

- As with monostatic, the scene centre response must be unaffected by the 'Stolt' interpolation.
- For the equal angular momentum case, only a small distortion is required.

- The bistatic form of the 'Stolt' is probably two-dimensional.

6.3.2 Curve fitting approach

A more systematic approach has been adopted to find the form of the 'Stolt'. The same process is employed to perform the matched filter operation as described previously. The image is then subjected to a distortion. This data is then Fourier transformed back into the image domain. The contrast of this image is used as a cost function to optimise a parameter set. Then this parameter set is applied to the distortion and the process is repeated until the change in the parameter set is less than a specified tolerance. A full outline of the method is shown in Figure 6-13.

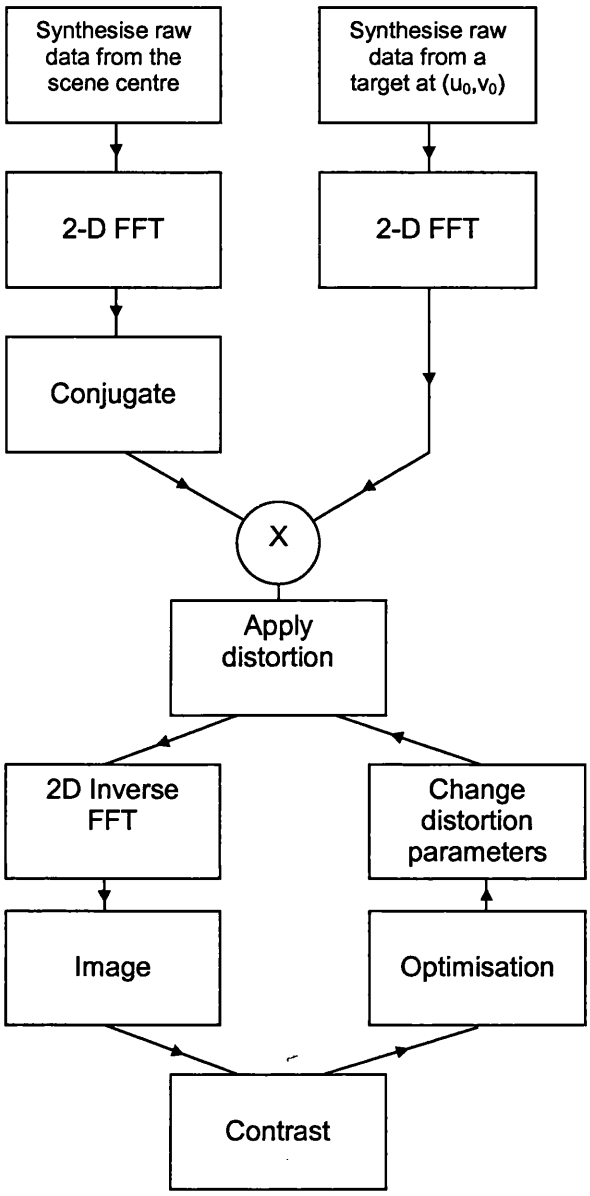

Figure 6-13 Optimisation routine

In all cases, this method was set up to test a particular distortion. This distortion always involved the original monostatic Stolt equation as a factor.

Initially this approach was tested on monostatic data. Here the curve used for fitting was $K_Y \rightarrow A.\sqrt{K_R^2 - K_X^2} + B.K_X + C.K_Y$, with no distortion in K_X and the tolerance set to 0.1. This process gave the results A=1.0625, B=0.0625, and

C=0.0625, implying that the Stolt interpolation alone gives the best image. This is as expected and shows that this method works.

The approach was then used on the generic bistatic scenario described earlier. Through the development of PFA, a bistatic equation for K_R was developed as $K_R=4\pi f.\cos(\varphi/2)/c$, where φ is the bistatic angle. This factor of $\cos(\varphi/2)$ has been included in this RMA work. Initially, the raw data was set up to have a single target displaced from scene centre in the x, y, u or v direction respectively. The model used for fitting was :

$$K_Y \rightarrow A.\sqrt{K_R^{\,2} - K_X^{\,2}} + B.K_x + C.K_Y + D.K_X^2 + E.K_Y^2 + F.K_X K_Y ,$$

again with no distortion in K_X.

	A	B	C	D	E	F
x	0.0625	0.3125	0.0625	0.25	0.0625	0.0625
y	0.0625	0.3125	0.0625	0.3125	0.0625	0.0625
u	0.0625	0.125	0.0625	0.3125	0.0625	0.0625
v	1.1875	0.0625	-0.0625	0.0625	0.0625	0.0625

Table 6-1 Parameter set for bistatic geometry

In all cases, parameters C, E, and F are insignificant. Parameter A appears to be insignificant for targets displaced in x, y and u but the most significant for targets displaced in v.

As a single distortion is required for all targets in the scene, this method was then tested on scenes involving a grid of nine targets. The geometry was simplified by setting each aircraft to fly along the same track with only horizontal separation, Figure 6-14.

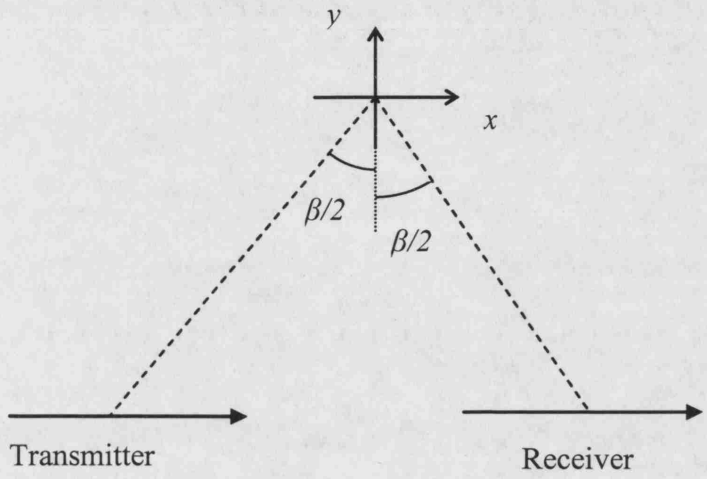

Figure 6-14 Parallel bistatic geometry

Initially, a simple model was used in the fitting process, namely $K_V \to A.\sqrt{K_R^{\,2} - K_X^{\,2}} + B.K_x + C.K_Y$. The results of this process gave the parameters as A=0.0625, B=1.0, C=0.8125, implying that the monostatic Stolt interpolation is the least significant term. A quadratic distortion in K_Y was then added as in the previous example *i.e.* $K_V \to A.\sqrt{K_R^{\,2} - K_X^{\,2}} + B.K_x + C.K_Y + D.K_X^2 + E.K_Y^2 + F.K_X K_Y$. This process gave the parameters as A=0.0625, B=0.0625, C=0.0625, D=1.5625, E=0.0625 and F=0.0625, implying that only the K_X^2 term is significant. The process was repeated, but this time including a constant term in the parameter fit *i.e.* $K_V \to A.\sqrt{K_R^{\,2} - K_X^{\,2}} + B.K_x + C.K_Y + D.K_X^2 + E.K_Y^2 + F.K_X K_Y + G$. This seems to

give a contrasting result to before; A=0.0625, B=0.0625, C=0.0625, D=0.0625, E=0.0625, F=0.0625 and G=-0.4375, only the constant being significant.

A linear two-dimensional distortion was then passed through this fitting process. In this case $K_Y \rightarrow A.\sqrt{K_R^2 - K_X^2} + B.K_x + C.K_Y + G$ and $K_U \rightarrow H.K_X + I.K_Y + J$. This gave results as A=0.0625, B=0.0625, C=1.0625, G=-0.3125 implying that the monostatic Stolt distortion is not significant nor is the K_X term. Also, H=0.0625, I=0.0625, and J=0.0625, implying that no distortion in u gives better results than a linear one, to this level of accuracy. A quadratic two-dimensional distortion, in K_U and K_V, has been implemented. However, due to the computational inefficiency of the method, no results are available at this time. For high-resolution imagery, an accurate approximation for the bistatic equivalent of the Stolt interpolation is required. From the results presented, it is clear that the distortion required is not a simple expression nor can it be approximated by one.

6.4 Summary

The range migration algorithm (RMA) is an almost exact solution in the monostatic case, subject only to the stationary phase approximation. As such, it does not have the scene size limitations of PFA. This made it the preferred choice for the bistatic SAR processing engine.

The difficulty with trying to adapt the RMA for bistatic geometries lies in the more complicated bistatic expression for phase. An analytical expression for this phase after matched filtering is not available. This leaves the form of the bistatic equivalent of the Stolt interpolation unclear.

Initial work has examined the phase of targets after the matched filtering stage. Simple forms of distortion have been applied and the phase of the output examined. A systematic optimisation approach has been implemented, but this has been unsuccessful. It is unlikely that this method would reveal a good enough approximation for the distortion for high-resolution images to be obtained.

It appears that simplifications would have to be made to adapt the RMA for bistatic geometries. What approximations these are and their effect on the scene size limitations are unclear. It is possible that these approximations will introduce scene size limitations comparable to those seen in the bistatic variant of the Polar Format Algorithm (PFA) discussed in the previous chapter. It was decided that this bistatic variant of the PFA would be used to process the data.

Chapter 7. Bistatic SAR demonstration

7.1 Introduction

A key element of this work was a full-scale airborne demonstration of bistatic SAR using two experimental radars. This chapter describes the activities undertaken in the lead up to this demonstration, the details of the trial itself and the imagery produced through the novel bistatic processor written by Andrew Horne based on his variation of the PFA tested in Chapter 5.

7.2 Experimental equipment

7.2.1 Radars

QinetiQ has access to two experimental radar systems: the QinetiQ owned Enhanced Surveillance Radar (ESR), flown in a BAC1-11 aircraft, and the QinetiQ/Thales' Airborne Data Acquisition System (ADAS) radar, flown in a civilian helicopter. Both radars operate at X-band with their centre frequencies aligned. The trials configuration is pictured in Figure 7-1 and uses the ESR as the bistatic illuminator and the ADAS radar on the helicopter as a bistatic receiver. This takes advantage of the higher transmit power of the ESR.

Both radars record raw data and auxiliary information to wide bandwidth tape for laboratory analysis and processing. This auxiliary data includes time stamped navigation data, which is required to form motion estimates for both the illuminator and the receiver antenna phase centres. ESR essentially operated

in a normal monostatic mode and was thus able to form a monostatic image to validate radar operation, check the illumination point, and provide a time coincident monostatic image of the scene for comparison of characteristics. The ADAS receiver also operated in a normal monostatic mode but with the transmitter disabled. The radars operated at precisely the same PRF which is digitally synthesised on both systems.

Both radars were operated in a spotlight mode, whereby each antenna is steered to a fixed geographic location, the centre of the scene. In this way the requirements to synchronise imaging legs are greatly relaxed. The drawback is that the precise squint angles at which data will be acquired are not known prior to acquiring the data. This is acceptable provided the processing algorithm is capable of processing squinted data. There are, however, tighter requirements on platform positioning at higher resolutions to ensure the required scene falls within the receive range window. A spotlight experiment of this type can be achieved without pulse chasing (where the receiving beam rapidly scans across the footprint of transmitting beam as it propagates), again greatly simplifying the equipment required.

The experimental equipment allows for direct path synchronisation at some imaging geometries. This is an important aspect of the experiment but is not essential for useful results to be obtained. As discussed in [29], the direct path allows for the oscillator phase noise correction. It could also be used to synchronise the radars. The implementation of an omni-directional receive antenna on the helicopter has been incorporated into the modifications to allow for the direct path to be recorded.

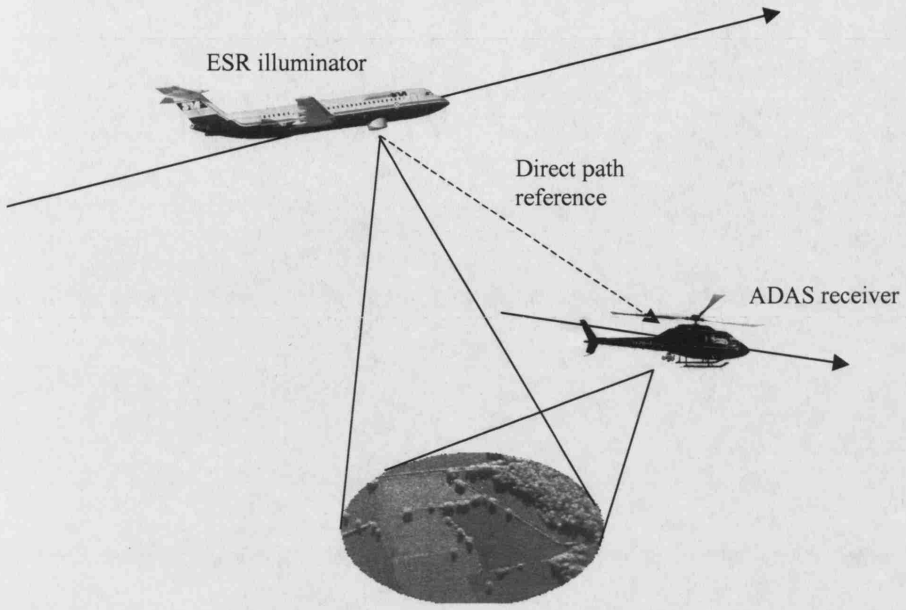

Figure 7-1 Demonstration approach

In addition it should be noted that both radars were operating in well-established modes that have been extensively tested through previous trials work. All image formation processing is carried out on the ground, separating processing software development and validation from the execution of the experiments themselves.

7.2.2 Synchronisation equipment

Synchronisation was maintained using a pair of caesium atomic clocks. This frequency standard was chosen because it appeared able to meet the synchronisation requirements of the experiment and it is probably the simplest to implement, particularly during the experimental phases.

The frequency accuracy of the clock is typically achieved after a 30 minute warm-up, with no calibration or operator intervention required. The performance and environmental conditions are adequate for the experiments

proposed. It is accepted that drifts may occur through relativistic effects as discussed in reference [29]. If so, these can be compensated for in the processing stage (by using recorded height, velocity and manoeuvre history during the sortie which is available in the navigation data stream of both radars).

The atomic clocks include the following outputs which were used in the experiment:

1. a 10MHz low phase noise oscillator output (locked to the atomic standard);
2. a logic level one pulse per second (pps) timing reference;
3. a serial link that can convey actual time (hours, minutes, seconds).

The clock provides automatic synchronisation to within 50ns of a reference pulse, for example from another co-located atomic clock. A manual "SLEW" command is also available to time synchronise the two clocks to greater accuracy.

The clock also has an in-built battery to support 45 minutes of operation. This is sufficient to allow the clocks to be transported from a laboratory (where alignment can take place) to their respective aircraft. Transition from mains operation, to battery, and back to an external DC supply on the aircraft does not affect timing accuracy. It was hoped that this facility would allow a simple synchronisation procedure avoiding the use of communications links or external timing references. The clocks could have been simply brought together in the laboratory before flight to synchronise and measure the delay, and then installed

on the aircraft, under battery power, and used in the experiments. Afterwards they could have been brought back to the laboratory to measure the time drift to provide confidence in performance and to validate the relativistic effects. However, due to airworthiness constraints, manufacturing costs and installation time (the clock only has 45 minutes of battery power), both clocks had to be installed on their respective aircraft prior to the trial. This meant the synchronisation procedure required the helicopter and BAC 1-11 to be close to each other, and the clocks to be connected via a long cable with a known propagation delay. The synchronisation itself had to be performed via a communications link. The procedure is then:

1. warm up the clocks under aircraft/ground power;
2. connect the clocks via a long cable and use automatic synchronisation to get an initial 50nS alignment via long cable;
3. remove the propagation delay for the long cable;
4. use manual slewing and laboratory test equipment to achieve full alignment accuracy;
5. transfer to aircraft power (if using ground power);
6. fly the sortie;
7. bring helicopter and BAC 1-11 back together and connect clock via long cable;
8. measure the time drift (allowing for propagation delays) to provide confidence in performance and to validate relativistic corrections.

7.2.3 Interface of atomic clocks to the radar

Another area for development was the interface of the atomic clocks to the radars, and the synchronisation of the radars to the outputs of the atomic clocks. This synchronisation involves three aspects:

1. The synchronisation of pulse repetition interval (PRI) of the two radars, *i.e.* ensuring that each radar starts at precisely the same time so that a conventional timing offset of the receive window of the receiving radar records bistatic data from the scene at the expected place.
2. Synchronisation of the navigation streams of the two radars. This requires knowledge as to *which* PRI on one radar corresponds to a PRI of the other.
3. The use of the atomic clock's frequency reference as the timing reference of the radar. Both radars use a single timing reference to which all other frequencies and timing signals are locked. Thus synchronising the master oscillator guarantees coherence subject only to the clock's phase noise, and the continuation of time synchronisation once it has been established.

A dedicated interface unit is required to interface the atomic clock to each radar. This allows the radar operator in each aircraft to agree (over the air-to-air radio) a precise time at which the two radars will automatically synchronise. This will generally be the start of the data acquisition period on each imaging leg. The advantages of the separate interface unit are that it removes the need for costly

software and user interface modifications to the radars, and only one design is required to serve the two radars. The interface unit essentially gates the one pulse per second timing signal from the atomic clock to provide a single shot reset pulse to each radar at a precise time agreed by the two operators. Finally the 10MHz frequency reference is passed directly to each radar.

Modifications to the radars are thus limited to:

1. locking the master oscillator to the external frequency reference (or replacing the internal reference with a feed from the external reference);
2. resetting the PRI counter in response to a single external pulse;
3. tagging at least one PRI with the reset pulse or atomic clock time.

These radar modifications were carried out by the manufacturers of each radar, along with the inclusion of an omni-direction antenna to record the direct path signal on ADAS.

The design and manufacture of the interface unit was designed and built in-house (as a student project) using battery power to eliminate any safety-critical interfaces to aircraft power. This was relatively simple – a microprocessor reading time from the atomic clock over the serial link, comparing it with a user-entered time and a hardware gating of the one pulse per second timing pulse.

7.3 Planned progressive demonstration

Flight trials are very expensive to organise and execute. It was thus essential that there was high confidence that trials would succeed before they were carried out. This required a carefully thought out progression of experiments. This was to be achieved through the following stages:

1. laboratory clock time and frequency stability experiments;
2. laboratory (or on the aircraft) validation of the synchronisation of each radar;
3. combined radar hanger test without radiating;
4. ground radiating test across the airfield;
5. flight trials.

Stage 1 was completed using the two clocks together in the laboratory. The clocks were synchronised then left to run over a period of 24 hours with the time difference being recorded from the 1pps outputs. This was repeated to measure the average drift over the 24 hour period. Stage 2 was completed as part of the hardware modifications to each of the radars. Bench tests using the atomic clock were performed on each radar separately. Stages 3 and 4 were completed at Boscombe Down airfield and detailed in section 7.4. Due to the success of the stages before it, stage 5 went ahead as planned and is detailed in section 7.5.

7.4 Ground trial

Following the independent testing of the modifications made to each radar, the two systems were tested together at QinetiQ's Boscombe Down airfield. The

ADAS radar was mounted in the back of a van to avoid costly aircraft fitting. Initial experiments were to check the synchronisation procedure and to test that the radars could be synchronised. This involved bringing the ADAS radar close to the BAC1-11, connecting the clocks and synchronising to agreed times via a communications link. The delay between ESR's detected RF and ADAS' range zero was measured and calibrated to be zero, in order to align the radars as closely as possible. The time difference between the clocks was checked over repeated synchronisations. This was found to be stable, and within the tolerances expected. Both radar systems were shown to be locked to the exact PRI with no jitter. As this was successful the ground trial proceeded as planned with ESR radiating on the ground.

The ground trial was an opportunity to fully test the hardware modifications of each radar in unison, in other words that the radars were synchronised in time, so the pulses were consistently recorded at the correct range so that the PRF's were locked. Also to test that the radars were synchronised in phase, *i.e.* the Fourier transformed data should be centred around dc with acceptable phase noise levels.

The set up for the ground trial is shown in Figure 7-2. ESR remained in the same position to the south of the site throughout the experiment. After initial loop back and calibration tests, ADAS was driven to ESR where the clocks were connected and the synchronisation procedure took place.

ADAS then moved to position 1, where it stayed for the majority of the trial, with its antennas (both the new omni-directional and the conventional horn antenna) pointing directly at ESR. Placed close to ADAS were corner reflectors

(trihedrals) and small spheres in the hope that ESR would pick up a return signal to verify it was operating correctly.

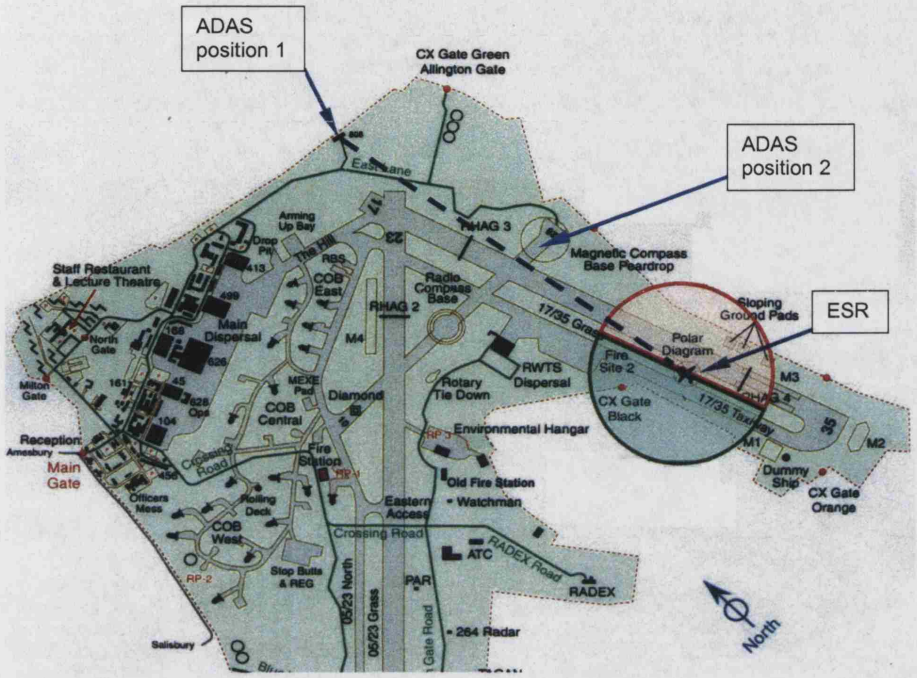

Figure 7-2 Ground trial map

Data was recorded from ADAS at the correct range. Both waveforms planned for the air trial were tested. This data was analysed in the laboratory on site to confirm that it was as expected. The signal quality appeared fairly poor, but this could be explained by multipath effects from the radars being so close to the ground.

After the data was recorded at the correct range, the next test was to see if it was possible to range compress it. This was also done on site at Boscombe Down. The pulse compressed data appeared to have a double peak, this could also be due to multipath effects.

With these tests complete, ADAS was then moved to position 2 in line with ESR and pointing at some targets located close to ADAS' position 1. It was hoped that this would demonstrate a bistatic return from ESR to ADAS via the targets. ADAS was unable to pick up a clear signal from the targets. However a good signal was picked up via the omni-direction antenna and the analysis of this signal is shown here. Figure 7-3 shows the result of range compression of the signal captured through the omni-directional antenna. The peak of each return remains in the same range bin with successive pulses, this shows that there is no PRI jitter between the two radars.

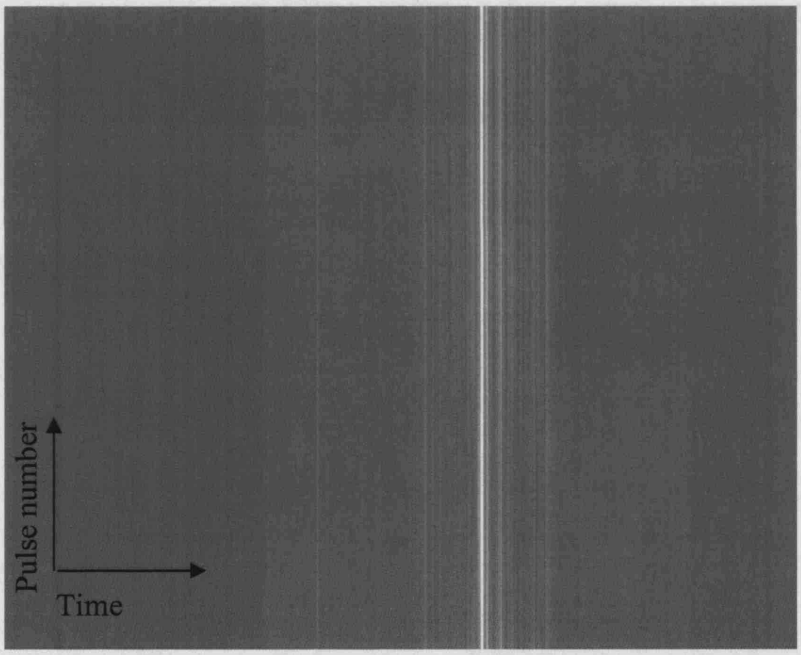

Figure 7-3 Range compressed data from ground trial

Taking a single return from the above range compressed data gives the range profile shown in Figure 7-4. Here it can be seen that the sidelobes are about 20dBs down from the mainlobe. As both radars are fairly close to the ground, it

was expected that the signal would be affected by multipath returns. The higher than expected sidelobes are consistent with multipath corruption

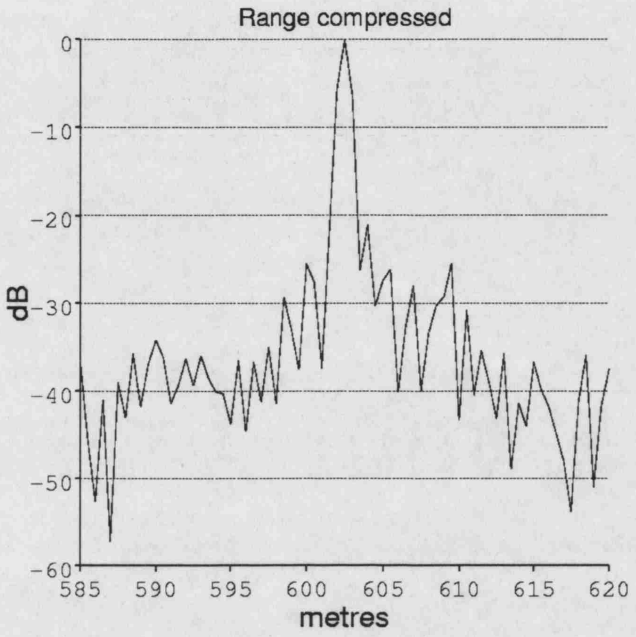

Figure 7-4 Single range profile from ground trial

The phase noise of the system is obtained by taking a slice along the peak of the image data and Fourier transforming it in pulse number. The result of this can be seen in Figure 7-5 alongside an example of the monostatic phase noise. Both plots are of power in decibels against frequency in hertz.

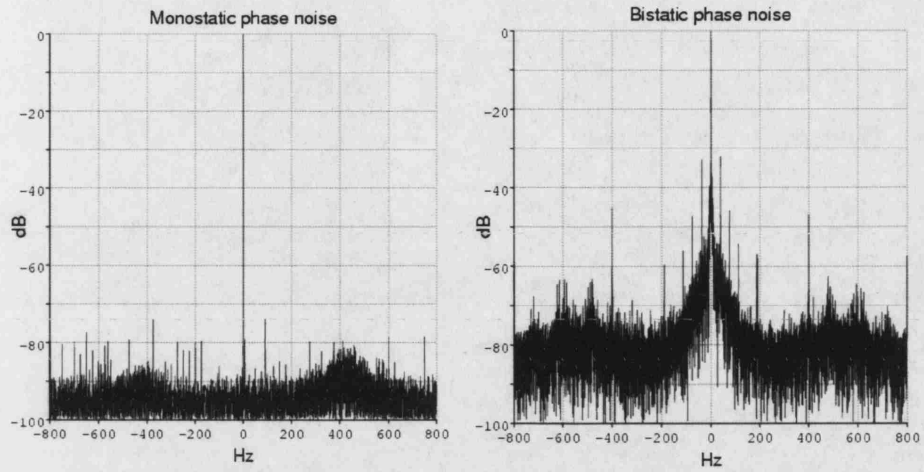

Figure 7-5 Monostatic and bistatic phase noise from ground trial

The monostatic plot is taken from ADAS loopback tests performed at the ground trial (ADAS using one atomic clock as described previously). There is a very sharp peak in the centre of the plot at dc. The sidelobes are generally more than 80dB down. The bistatic phase noise plot is taken from the ground trial with ADAS in position 2 receiving the direct path signal from ESR through the omni-directional antenna. This shows the phase noise introduced by using two different atomic clocks as send and receive oscillators and using the different systems to send and receive the signal. The highest sidelobes are more than 30dB down with the main bulk of the sidelobes better than 70dBs down.

Monostatic SAR uses the same master oscillator to generate the reference frequencies used in both up-conversion and down-conversion. Low frequency components of phase noise have little effect on system performance as they change very little from the time of transmission to the time of reception of the signal, and therefore tend to cancel out when the received signal is mixed to baseband using the same master oscillator. With the bistatic system, separate oscillators are involved in the transmitter and receiver and each will exhibit

independent realisations of phase noise. Thus the bistatic system is susceptible to the whole spectrum including the close to carrier component. The plots of phase noise are as predicted in the theory presented in reference [27].

The effect of this additional source of phase noise, from the two independent master oscillators, is to cause image degradation. Degradation takes the form of defocus, high image sidelobes and multiplicative noise. This source of phase noise will be indistinguishable, in terms of its effect on imagery, from phase noise of different origins e.g. from unsensed platform motion. Any autofocus techniques used to estimate other phase errors should be equally applicable to correcting oscillator phase noise.

After the trial the atomic clocks were brought together again (approximately 6 hours after synchronisation) and the time drift was measured as less than 1ns. The trial was considered a success and accordingly the airborne trial went ahead as planned.

7.5 Air trial

The full airborne demonstration took place during September 2002. The plan was to use a lower bandwidth on the first day, and if this was successful proceed to a higher bandwidth on the second day. This was a lower risk option as the reduced bandwidth means that a larger scene size (of lower resolution) is recorded and puts less stringent demands on the time synchronisation of the two radars. Unfortunately, data from the first day was unable to be recorded on ADAS. However, the day was invaluable allowing calculations to be made and ensuring the second day ran more smoothly.

This meant that the second day had to encompass a range of bistatic geometries at both the lower resolution and using the higher resolution bandwidth. A list of the planned geometry from day 2 for the imaging legs characterised within this thesis is given in Table 7-1.

7.5.1 Targets

The target for the experiment was centred around Copehill Down village on Salisbury Plain, *Figure 7-6*. This area was chosen as it is a controlled urban environment surrounded by fields. This allowed analysis of the effect of bistatic imaging on both urban structures and clutter regions. Two sets of calibration targets were placed in the scene. The first were static trihedrals used for measuring the resolution from the monostatic ESR image. The second were particular targets to investigate how they would perform under bistatic imaging. These included trihedrals with their boresight pointing on a bearing bisecting the bistatic angle inclined at 9°, spheres, and dihedrals with their seam angle horizontal, tilting up at 9°, again pointing on a bearing bisecting the bistatic angle.

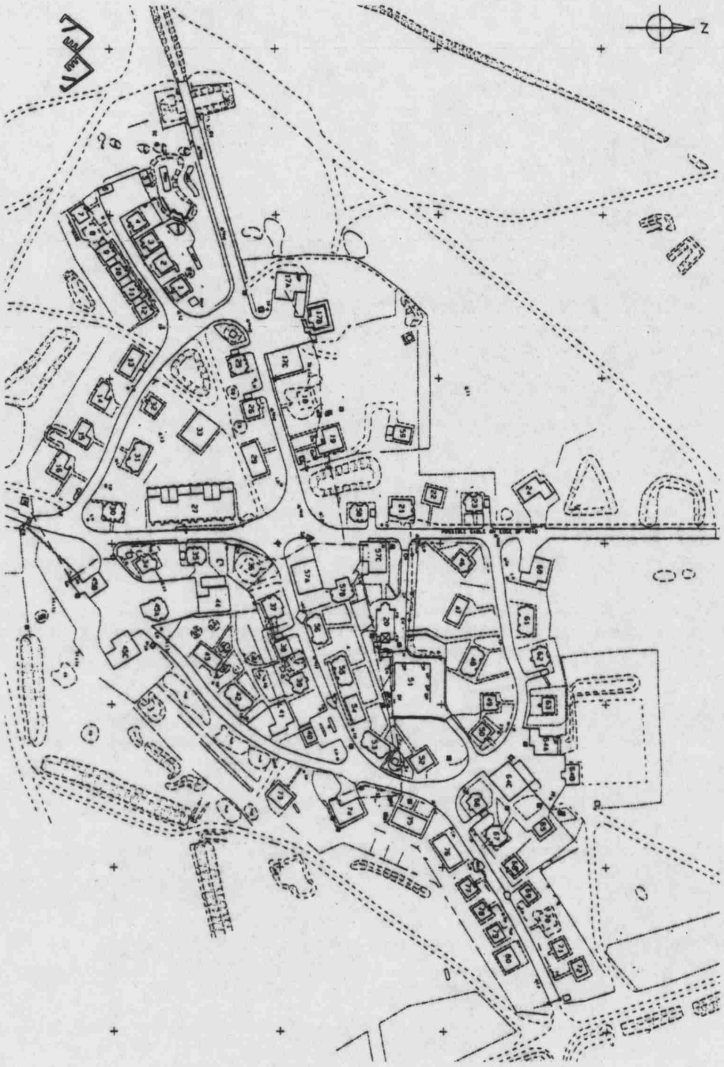

Figure 7-6 Map of target scene

7.5.2 Planned experiments

Table 7-1 provides an account of the planned imaging legs for the second day of the airborne trial which have imagery discussed within this thesis. It is only a broad approximation to what was actually flown. An 'L' in the bandwidth column indicates the lower bandwidth, with an 'H' representing the higher bandwidth used on the trial. In the table, speed is taken to be positive in the clockwise sense and is given in metres per second. That is, although the aircraft

were flying nominally straight tracks, ESR flying to the south of the scene from east to west is taken as being in a positive sense. ADAS' antenna is not fully rotatable in flight, it has to be fixed to look to one side. This meant the helicopter always had to fly in the same sense (*i.e.* clockwise). Most of the even numbered legs were with the helicopter hovering although some were used to demonstrate retrograde motion (when the transmitter and receiver are flying in opposite senses). Differing grazing angles were flown to demonstrate out of plane motion and highlight different shadowing effects. Different grazing angles were also used to simulate the effects of different stand off ranges. A platform at a lower grazing angle simulates a long-range stand off radar, with higher grazing angles simulating short/mid-range operation.

			ADAS		ESR	
Leg	β	band-width	grazing angle	ground speed	grazing angle	ground speed
3	30°	L	9°	13m/s	9°	125m/s
7	30°	H	9°	25m/s	9°	125m/s
10	30°	H	27°	0m/s	9°	125m/s
11	60°	H	27°	13m/s	9°	125m/s
13	60°	H	9°	25m/s	9°	125m/s
14	60°	H	9°	8m/s	9°	125m/s

Table 7-1 Planned imaging geometries for imagery presented in this thesis

ESR flew the same imaging runs throughout the trial; on a heading of 270° for the odd number legs and 090° for the even numbered. ADAS, being onboard a more manoeuvrable platform, adjusted its flight pattern to allow the collection of the different bistatic geometries an example of which is illustrated in Figure 7-7.

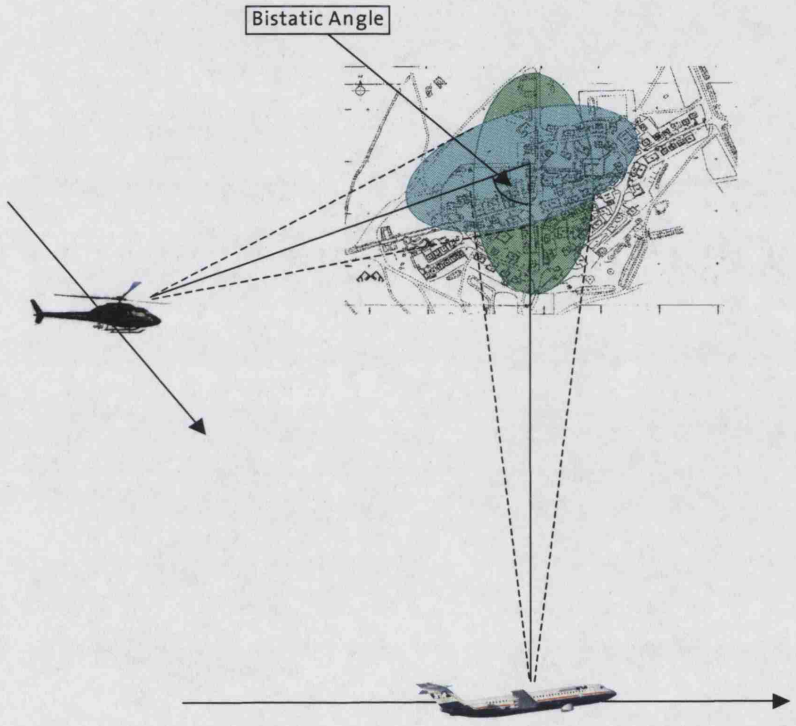

Figure 7-7 Imaging geometry

7.6 Processed results

This section aims to present the imagery processed through the novel bistatic processor (written by Andrew Horne) based around his novel bistatic version of PFA evaluated in Chapter 5. In particular it will discuss the imagery in terms of the processing issues, the autofocus, the resolution and the phase noise effects on image quality. The comparison of the bistatic images with the corresponding

monostatic images, plus a discussion of image characteristics and utility will be presented in the following chapter.

The omni-directional antenna on ADAS was set up to record the direct path signal at the 30° bistatic angle case. This would also give part of the direct path signal at 60° bistatic angle. The direct path signal does not appear to have been recorded in any of the legs. This appears to be a hardware problem with the delay required by ADAS to shift the two antenna range windows. Consequently, the direct signal cannot be used to help process any of the imagery.

The image is always formed using the option to process the data giving orthogonal sidelobes, with the image orientated along the vector bisecting the bistatic angle. The data is always inscribed out of the K-space support producing less resolution than the optimum theoretical resolution. This means that there is no need for the image to be (image-space) interpolated and that, since the sidelobes are orthogonal, resolution can be measured straight from the image.

The different angular rates of each platform affect azimuth resolution. The equation for azimuth resolution was developed in Chapter 3. The table below, Table 7-2, shows the effect of platform velocity on aperture length requirements. In all cases the aperture time shown is that required to produce a theoretical azimuth resolution of 1m. In each case the bistatic angle is 30°, the only quantity changing is the velocity of ADAS. Each of the ADAS/ESR velocity combinations is taken from the planned imaging runs.

ADAS velocity	ESR velocity	Required aperture time
25 m/s	125 m/s	1.6 s
13 m/s	125 m/s	2.4 s
0 m/s	125 m/s	4.5 s
-8 m/s	125 m/s	8.0 s

Table 7-2 Effect of platform speed on data requirements

This shows that processing the retrograde motion legs (ADAS' velocity of –8m/s) requires five times the data of the fast case with ADAS' velocity at 25m/s. Although this does not cause any fundamental problems, it puts a greater strain on the processing tools such as the motion compensation and autofocus. Any errors in these will become significant over this length of aperture.

7.6.1 Motion compensation solution

Within the scope of this work, a motion compensation (moco) solution for ADAS has been developed. This used the output from the platform's Global Positioning System (GPS) and Inertial Measurement Unit (IMU). The GPS unit outputs a position approximately twice a second. To accurately process SAR data with a PRI of fractions of a second, accurate positional information of the phase centre at the time each pulse is transmitted is required.

The output from the IMU consists of three delta velocities, three delta angles and a time. It has no sense of absolute position, velocity or orientation. The

output from the IMU is recorded at approximately 400 Hz. The moco solution is formed through an optimisation routine. An initial position, velocity and orientation (plus quantities such as a gravity vector and errors in the IMU readings) are 'guessed' from the GPS readings. These initial guesses are then altered so as to minimise the difference between the IMU realisation of position and the GPS recordings.

Unfortunately, there were problems with the recording of the navigation data. The GPS was not working in its most accurate mode. This meant that there were typical errors of the order of 10m on each GPS recording. Often the GPS dropped out completely and no values were recorded. The IMU had bit errors in the recording. These were in the form of swapped bits as well as sticking bits. Both of these led to problems forming an accurate moco solution. This had serious effects of the quality of the bistatic SAR imagery. It also puts additional strain on the autofocus solution.

7.6.2 Autofocus

The image that is formed by the experimental processor is then autofocused using the algorithm developed by Robert Middleton; details of which can be found in reference [29].

The autofocus is run on the processed image. This means that it is equally applicable to both monostatic and bistatic imagery. It is based on the Phase Gradient Autofocus (PGA), [30]. The PGA exploits the fact that all scatterers are defocused by the same phase error. It estimates the phase perturbation of the brightest scatterer in each range bin of the image and combines them to maximise the signal-to-noise ratio in the phase error estimate. The data is

corrected using the phase error estimate and the image is reformed. The process is repeated as necessary. A typical result from the autofocus can be seen in Figure 7-8 and Figure 7-9.

Figure 7-8 Bistatic SAR image before autofocus

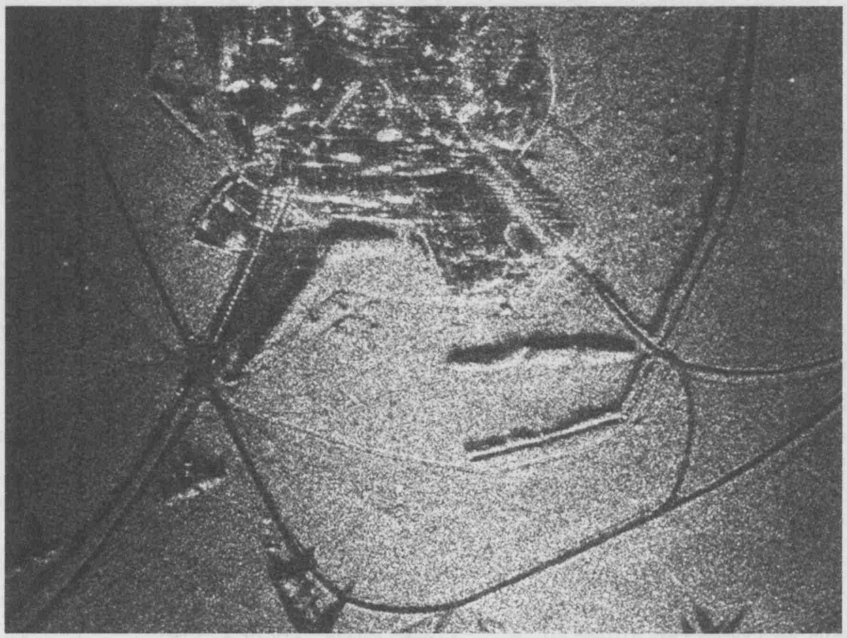

Figure 7-9 Bistatic SAR image after autofocus

7.6.3 Beam antenna pattern removal

In each bistatic image there is a strong return from the mainlobe-on-mainlobe interaction, illustrated in Figure 7-7. An example of this can be seen in Figure 7-9, with the brighter oval shape in the centre of the image. This is because the intensity in the image is affected by areas where the transmitted mainlobe antenna footprint overlaps the receiver mainlobe antenna footprint. This increased power can obscure parts of the image. This beam shape has to be removed in order to analyse the imagery. This has been removed by applying a filter to the focused image. As yet, this is not done accurately and leads to some low spatial frequency amplitude modulation effects in the image. It was found that if this filter was applied before the autofocus stage, the focusing algorithm did not work as well. This is probably due to the increased noise content of the imagery where high corrective gains have been applied.

7.6.4 Final imagery

An example image from the trial is shown in Figure 7-10. The data was processed from imaging leg 7. This was a high bandwidth imaging leg. The data was collected with both platforms nominally at 9° grazing angle around a nominal bistatic angle of 30°.

Due to problems with the navigation equipment on ADAS, only data very late on in the imaging run has been processed. This image, Figure 7-10, is formed with ADAS flying at a faster angular rate than ESR, in the same direction. As shown in Table 7-2, this requires less aperture data to process the image in azimuth. This requires a less accurate motion compensation solution for each platform.

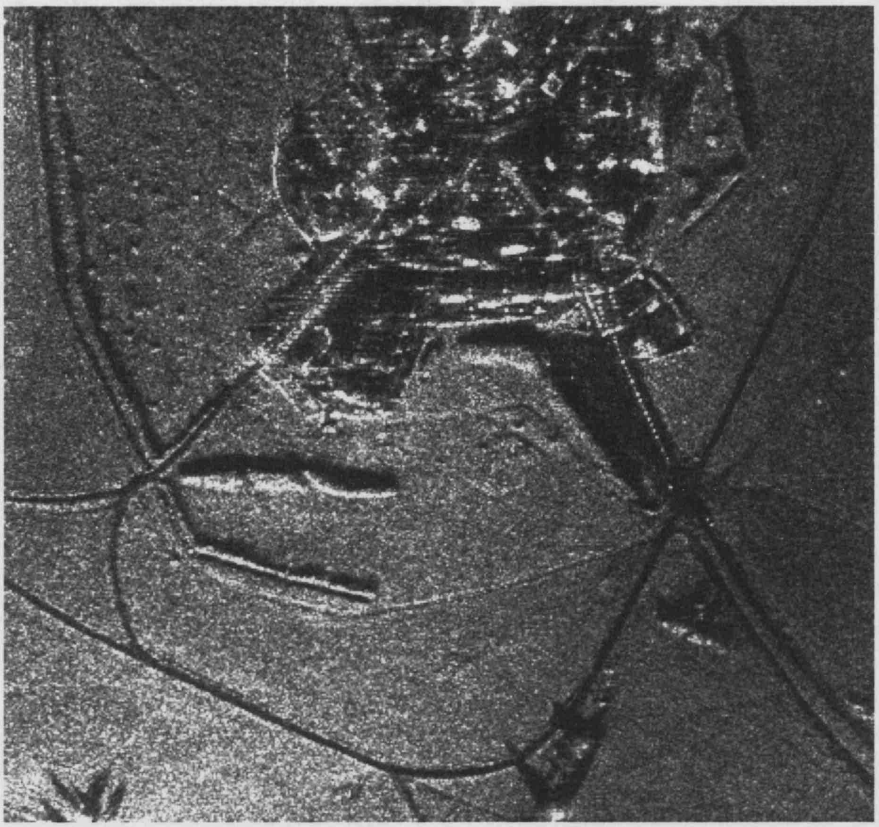

Figure 7-10 Bistatic image from leg 7

The resolution requested in the processor is in broad agreement with that measured from the image.

Although the autofocus has worked well on the car park area to the south of the scene (where the resolution was measured from), the buildings are out of focus. This is probably due to the fact that the autofocus can only fit one solution to the whole of the image. It tends to ignore high frequency phase errors which could be affecting the whole of the image, but would be more apparent in the urban area.

7.7 Summary

This chapter has detailed the route taken in getting to the full airborne trial of bistatic SAR along with the trial itself. This has included ground trials with analysis of the data to derisk the airborne demonstration. Details of some of the experiments flown at the full airborne trial have been given, along with an example of the processed imagery. This image is a high-resolution bistatic SAR image. As such it represents a considerable advance in SAR technology. Imagery from other imaging legs can be found in Appendix D.

Chapter 8. Bistatic SAR characteristics

8.1 Introduction

This chapter aims to characterise the imagery presented in Appendix D, to compare it with the equivalent monostatic imagery and examine some of the key features. A labelled monostatic image from leg 4 is presented in *Figure 8-1*. This has been labelled with key features which will be discussed when examining later images.

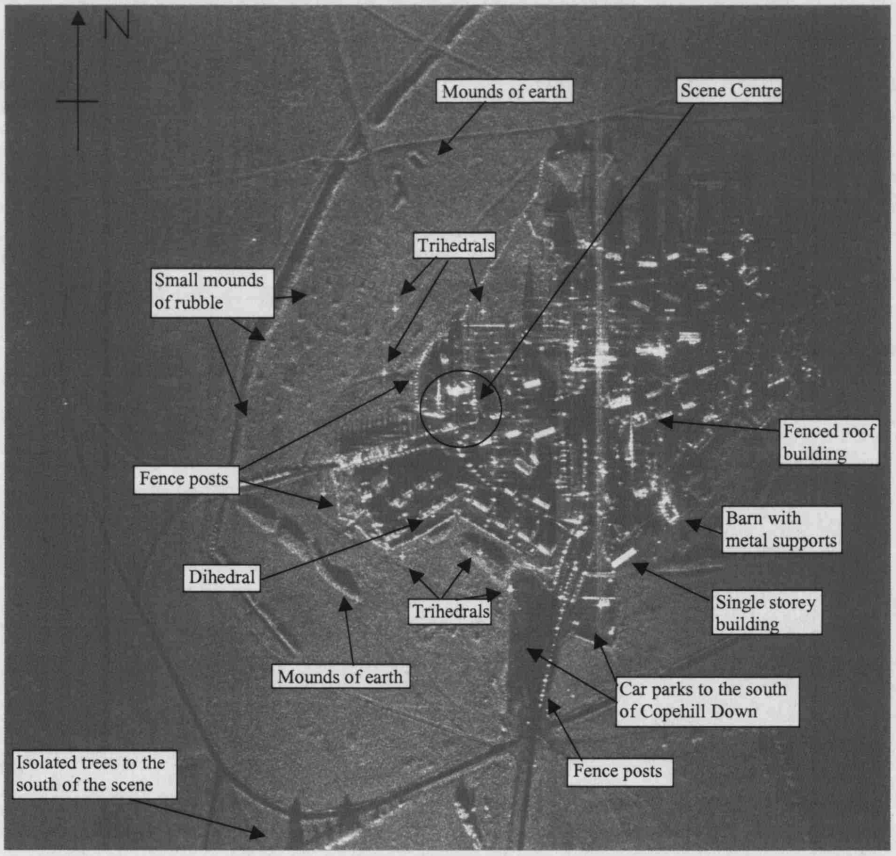

Figure 8-1 Monostatic image from leg 4

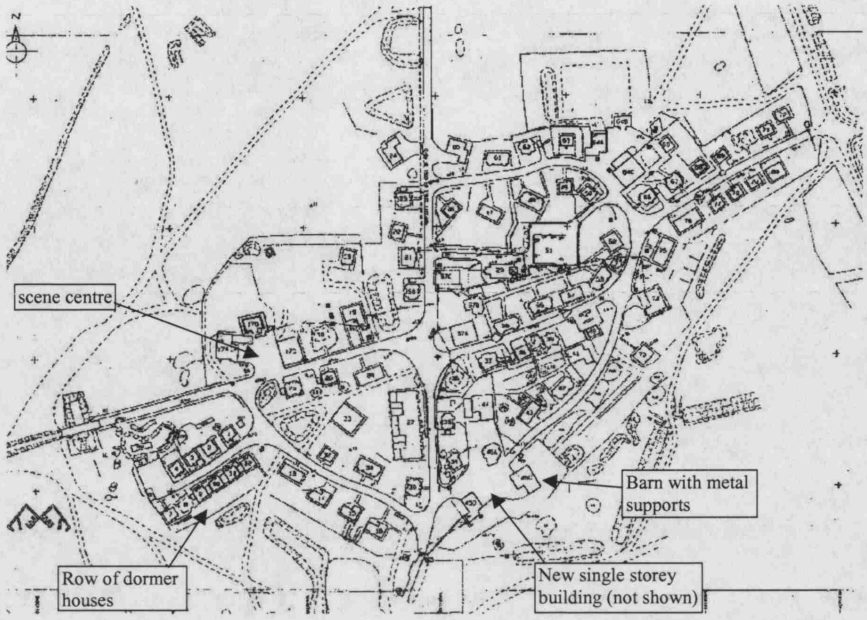

Figure 8-2 Map of target area

Since ESR was imaging from the south, the imagery in Figure 8-1 appears orientated the same way as the map shown in Figure 8-2 above. This map is slightly out of date as it does not have the new single storey building shown. A photograph of this building can be seen in Figure F-27. Figure 8-3 shows an aerial photograph of the whole of the site. This gives a good idea of the buildings in the area. However, again this is slightly out of date without the single storey building towards the south of the site. There are also now train carriages parked across the road exiting the village to the west.

Figure 8-3 Aerial photo (Cities Revealed aerial photography copyright The GeoInformation Group)

This section contains imagery from four different imaging legs of the airborne trial. In each case, the imagery appears orientated along the vector bisecting the bistatic angle with orthogonal sidelobes. Details of the planned flight of each leg were given in Table 7-1. Where small pieces of the image have been extracted for more detailed examination, they have been highlighted in larger images by a dashed rectangle.

8.2 Imaging leg 3

This was one of the lower bandwidth legs. Both platforms were flying at approximately the same angular velocity.

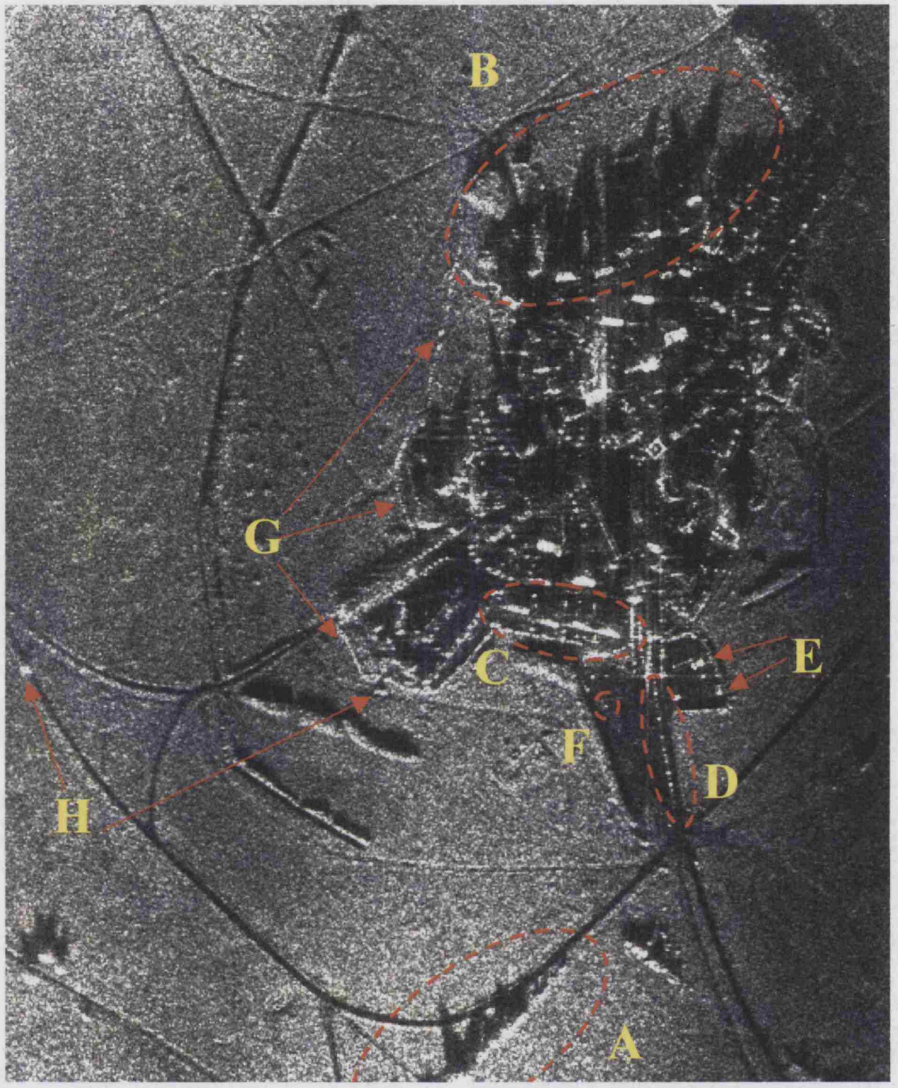

Figure 8-4 Bistatic image from leg 3

The row of trees at the bottom of the image, labelled A, is producing two shadows - one from the transmitter and one from the receiver. The shadows are of similar length as both platforms are at approximately 9° grazing angle. There are also double shadows visible from the buildings at the back of the village, labelled B. The front rows of houses, labelled C, show up well as they are visible from both radars.

The poles in the car park can be seen with some vehicles in the right-hand, smaller, car park, labelled D and E respectively. The small sphere is visible in the larger car park, and labelled F, but none of the other point targets are visible. The metal fence surrounding the village is clearly visible, parts are highlighted with the label G. There appears to be two vehicles on the tracks around the village, labelled H.

To characterise this image, it is constructive to compare it with the corresponding monostatic image. There are three choices for the definition of 'corresponding' monostatic image, illustrated in *Figure 8-5*. Image one provides a time coincident image, so the scene would be identical in both images. Image two provides an image orientated the same way as the bistatic one (although there are options in the processor to do this without moving the imaging platform position). Image 3 would provide the corresponding image from the receiver's position. Positions 1 and 3 give the two shadows seen in the bistatic image.

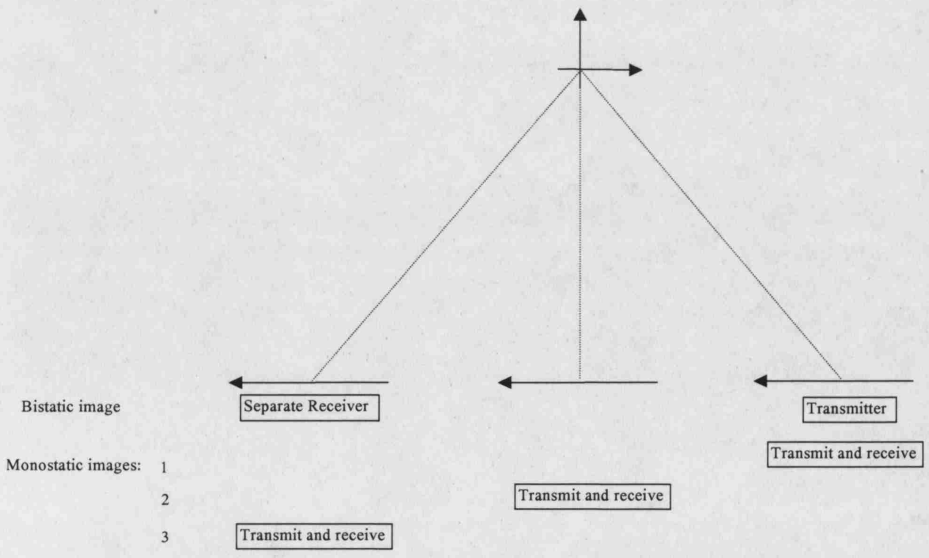

Figure 8-5 Three options for 'corresponding' monostatic imagery

Due to the length of the tracks flown, the monostatic image corresponding to the receiver's position (3) is not available for any of the legs currently processed. It should also be noted that position 2 is not necessarily the broadside image from the transmitter, and is a squinted image in the example given below. The monostatic image for position 2, the bisecting bistatic angle, and position 1, the time coincident position, are shown in Figure 8-6 and Figure 8-7. Both have been processed to the same resolution as the bistatic image.

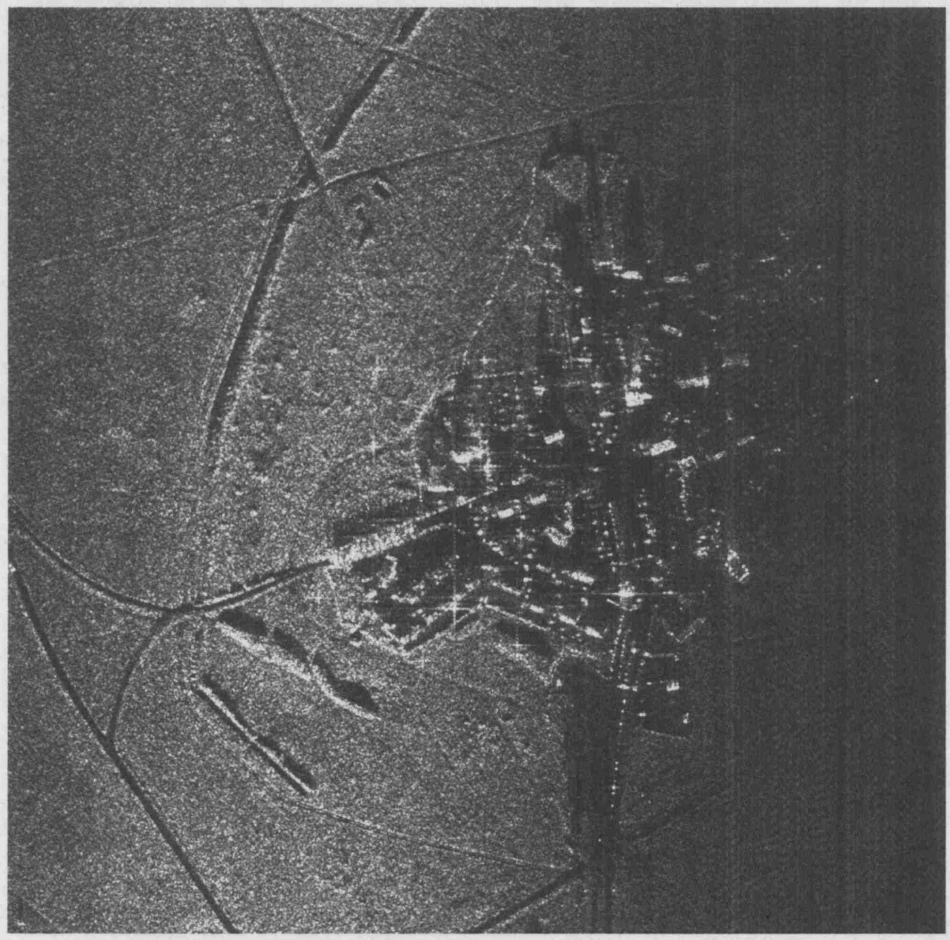

Figure 8-6 Monostatic image from the same time as the bistatic image formation (position 1)

The quality of the image is not good. There appears to be a strange striping effect on the right hand edge. The intensity of the image also falls away considerably to the right of the image. This is likely to be caused by lack of signal energy. It appears that the beam is centred on an incorrect position, as the designated scene centre location is not in the centre of the illumination.

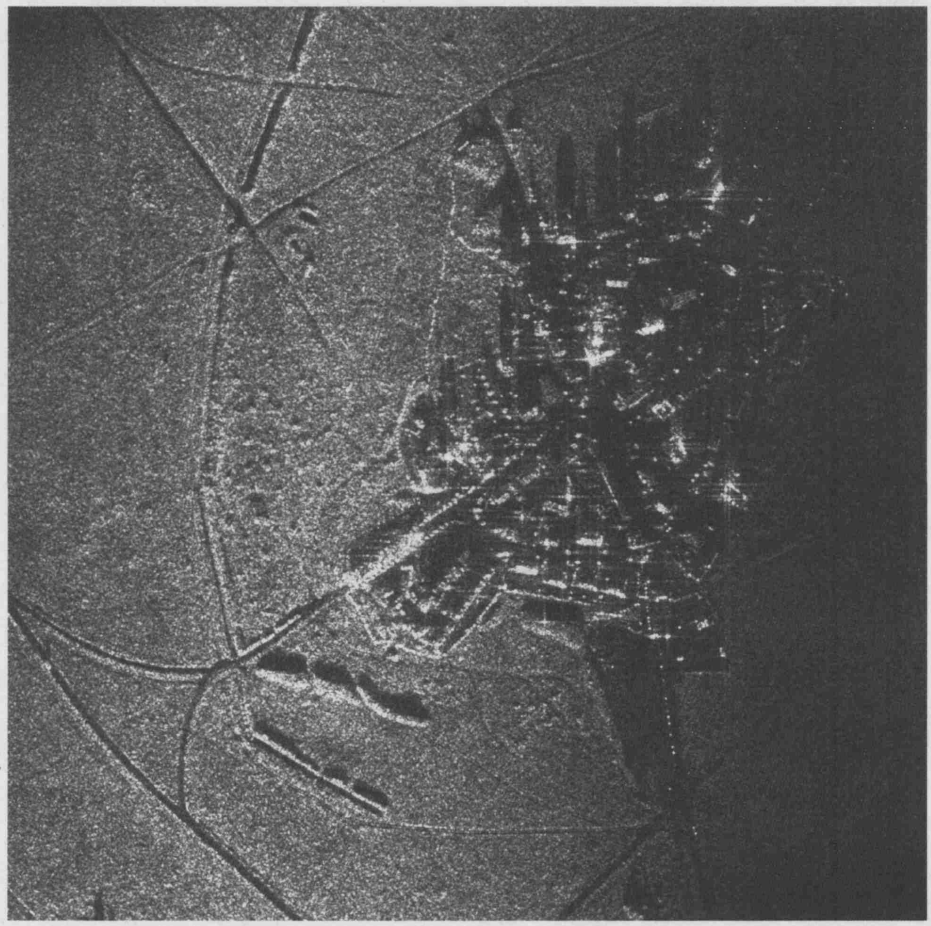

Figure 8-7 Monostatic image from data around bisecting bistatic angle (position 2)

This image is of better quality than the first monostatic one, although the intensity also drops away to the right of the image.

The trihedrals and dihedrals are more visible in the first monostatic image. The intensity of the return from the trihedral is of the same order in each image. Due to the viewing angle the return is slightly lower in the second image, it is the contrast within the image which makes them appear less bright. Forming successive monostatic images along the aperture shows that the return from the roofs of the buildings flashes on and off. This is probably due to a Bragg scattering effect from the corrugated roof tiles. The imagery being so dependent on viewing angle makes comparison of images formed at slightly different look angles difficult.

There is more dynamic range in the monostatic image than in the bistatic one *i.e.* the brightest parts of the monostatic image are relatively brighter compared to other parts of the image, such as the clutter areas. The bright returns have the effect of suppressing the contrast in the other areas of the image. For example, the poles in the car parks are clearer in the bistatic image. It is also possible to see the sphere in the bistatic image. However, this has the effect of making the clutter areas look more speckled in the bistatic image.

The village part of the scene has been cut out of the monostatic image from position 2 and is shown in Figure 8-8 next to the corresponding bistatic image. A dashed rectangle is marked on both images. This is the car park area of the village and is looked at in greater detail in Figure 8-9.

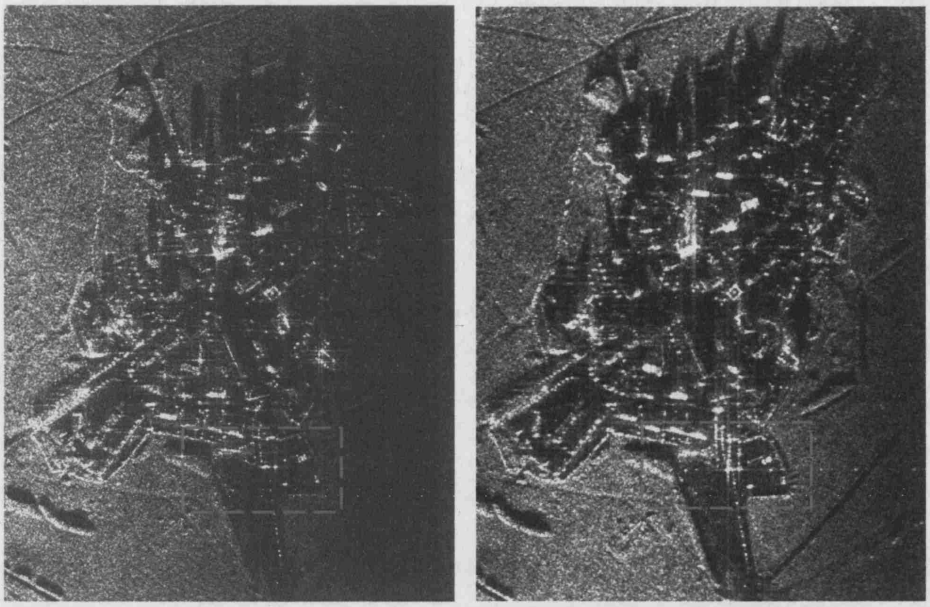

Figure 8-8 Comparison of monostatic and bistatic images, respectively, of the village from leg 3 with car park area highlighted

It is easy to note that the image on the right is bistatic due to the 'V' shaped shadows of the buildings at the top of the village. The shadowing around the mounds at the front left of the image is also different. The two shadows (one from each platform) lead to more of the image being in shadow. Here both of the platforms are at fairly low grazing angles, (both approximately 9°, note the similar length shadows), giving long shadows.

The row of houses at the bottom of the village and the row going towards the bottom left appear similar in both images. The intensity of the bistatic image does not appear to drop off to the right as it does in the monostatic image.

As the monostatic image is formed about a position bisecting the bistatic angle, similar buildings appear bright in both images. Generally, any house that is bright in the monostatic image is also bright in the bistatic image. However,

more houses appear bright in the bistatic image. This may simply be due to the parameters chosen to present the imagery.

From these images it is clear that the monostatic image is better focussed than the bistatic one. There is no autofocus applied to the monostatic image, as it does not appear to need it, and yet it still appears crisp. This is due to the BAC1-11's ability to fly very straight trajectories, higher quality navigation data and the motion compensation solution being more robust. The focus of the bistatic image is not as good, even though an autofocus solution has been applied. This is for three possible reasons. Firstly, it involves two platforms with different motion compensation solutions. Any errors in these will have a compounding effect on the bistatic image. Second, the receiver was onboard a helicopter which flies very erratic trajectories (plus the recording of the navigation equipment had significant errors on the helicopter) and third due to the additional phase noise putting additional emphasis on the autofocus.

It can be seen that buildings return different signatures in the two images. Both images have the fenced-roof building and the barn with metal supports clearly visible. The brightest return is also the same building. More of the roofs are visible in the bistatic image, probably due to their particular orientation acting like a flat plate between the transmitter to receiver.

Figure 8-9 focuses on the car parks from each image. In the monostatic image it is clear that there are three vehicles parked closely together. In the bistatic image it is not so obvious. The three vehicles are still resolved, but it is not so clear. Plotting a line of intensity through the middle of the three vehicles, does

give three distinct peaks. It is just the contrast in the image which makes this difficult to observe.

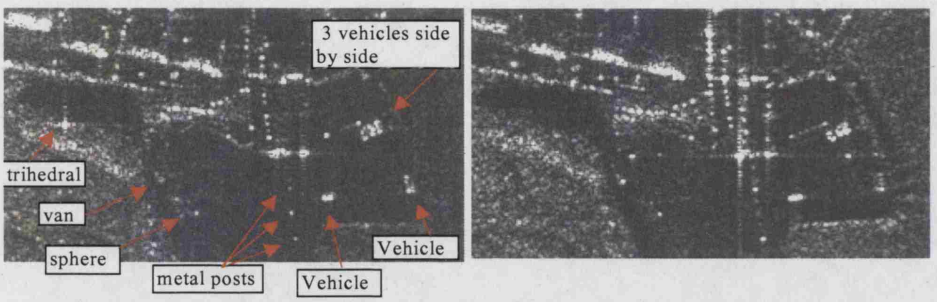

Figure 8-9 Car parks from monostatic and bistatic images

The imagery will be discussed further using high-resolution images from different legs in the following sections.

Another comparison of the two images is to analyse the clutter characteristics. Three fields have been used which appear in both the bistatic and monostatic images. The goodness of fit of the probability distribution is given as a Kolmogorov-Smirnoff test probability. The distributions that have been fitted to the data were the negative exponential, the Weibull, the log-normal and the K.

Field 1	Negative exponential	Weibull	Log-normal	K
Monostatic	1.5e-84	5.5e-10	1.4e-116	0.2
Bistatic	5.3e-18	2.1e-04	1.7e-150	0.8

Table 8-1 Kolmogorov-Smirnoff test fit probability results for field 1

It can be seen from this table that the best fit is the K distribution in each case. In the bistatic case it gets almost a 80% fit probability, but in the monostatic it is just below 16%. The cumulative density function (cdf) can be plotted for each

of the statistical plots against the data and is shown in Figure 8-10 for the monostatic case. Alongside this plot is an extract of the majority of the data from the first plot.

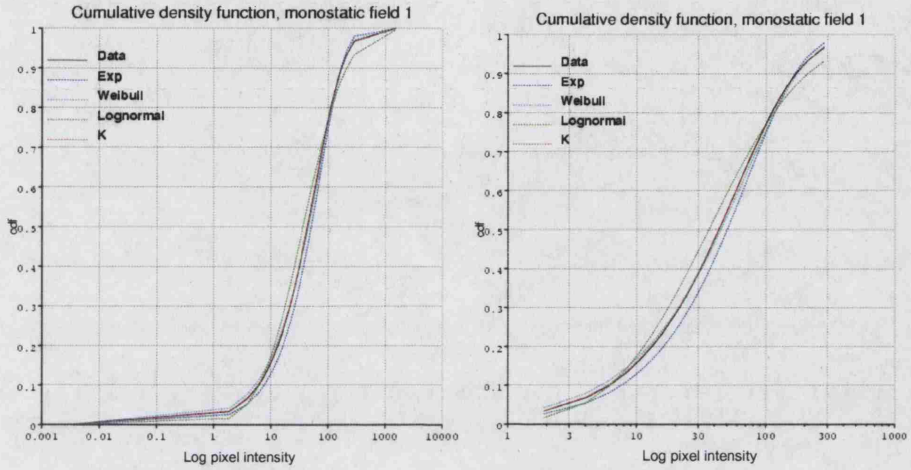

Figure 8-10 Cdf plots for statistics fitted in Table 8-1 plotted against data

As the K distribution is clearly the best fit for both the monostatic and bistatic data, the two sets of data cdf's are plotted against the best fitting K plot in Figure 8-11. The monostatic K plot has an order parameter, ν, of 4.27, whereas the bistatic K distribution has a ν value of 10.1.

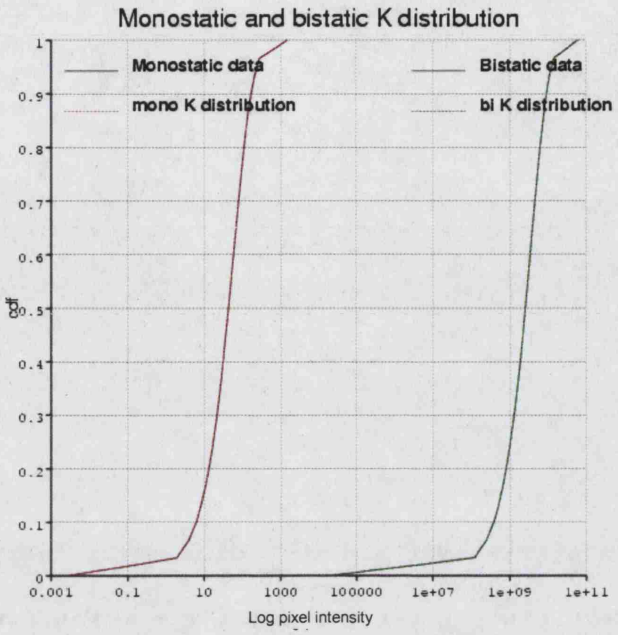

Figure 8-11 Monostatic and bistatic K distributions against data

This type of analysis is very dependent on the data used. For further comparison, two other fields have been examined.

Field 2	negative exponential	Weibull	Log-normal	K
Monostatic	9.1e-27	2.6e-03	3.0e-68	0.8
Bistatic	3.0e-37	2.8e-04	1.8e-109	0.6

Table 8-2 Kolmogorov-Smirnoff results for field 2

Field 3	negative exponential	Weibull	Log-normal	K
Monostatic	5.3e-127	2.2e-13	3.6e-130	0.5
Bistatic	2.4e-44	3.4e-07	5.0e-123	0.4

Table 8-3 Kolmogorov-Smirnoff results for field 3

In each of the three cases both the monostatic and bistatic data are best fitted by the K distribution. The summary of the goodness of fit and the parameters of each K distribution are shown in the table below.

	Monostatic		Bistatic	
	Fit	ν	Fit	ν
Field 1	16%	4.27	80%	10.1
Field 2	72%	6.02	58%	6.25
Field 3	46%	4.10	44%	5.64

Table 8-4 K distribution for clutter comparison

This shows the goodness of fit is dependent on the piece of data used. The value of ν, the shape parameter, is broadly similar throughout all the fields for both monostatic and bistatic data. The shape parameter is lower in the monostatic case *i.e.* the clutter appears spikier. This means that point target detectors could be more sensitive in the bistatic imagery, providing the targets have the same characteristics as in monostatic imagery.

This analysis shows that both monostatic clutter and bistatic clutter characteristics are best described by the K distribution and are not fundamentally different from each other.

8.3 Imaging leg 7

This image in Figure 8-12 is formed when ADAS is flying at a faster angular rate than ESR, in the same direction.

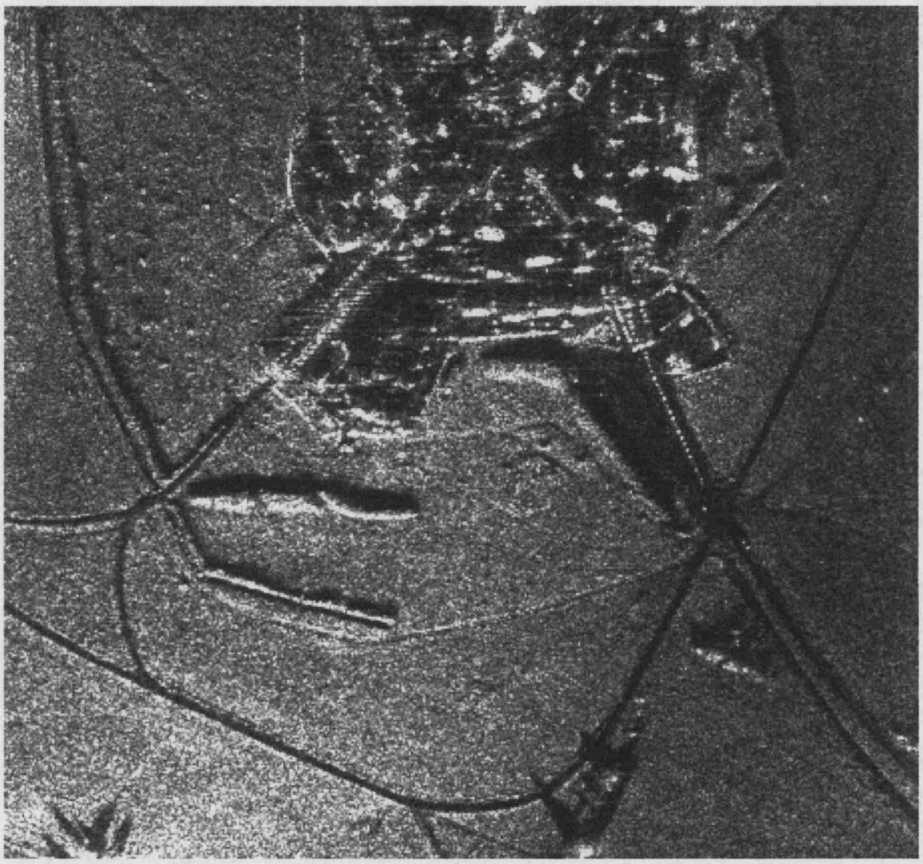

Figure 8-12 Bistatic image from leg 7

The two shadows from the trees at the bottom are clearly visible in the image. Both shadows are of similar lengths showing that the grazing angles of each platform are similar. The angle between the shadows is greater than in leg 3 as this image has a greater bistatic angle. The larger the bistatic angle, the less the two shadows overlap and so more of the image will be in shadow. When the bistatic angle approaches 90° the two shadows will become totally distinct and

the maximum amount of shadow is reached. The shadows are emphasised here, as the grazing angle of both platforms is only approximately 9°.

The sphere in the car park is again visible. The sphere at the nominal scene centre is also visible towards the top of the image. Again, none of the trihedrals or dihedrals are visible in the image, as expected.

The monostatic image presented in Figure 8-13 is the time coincident (position 1) image taken from ESR during this leg.

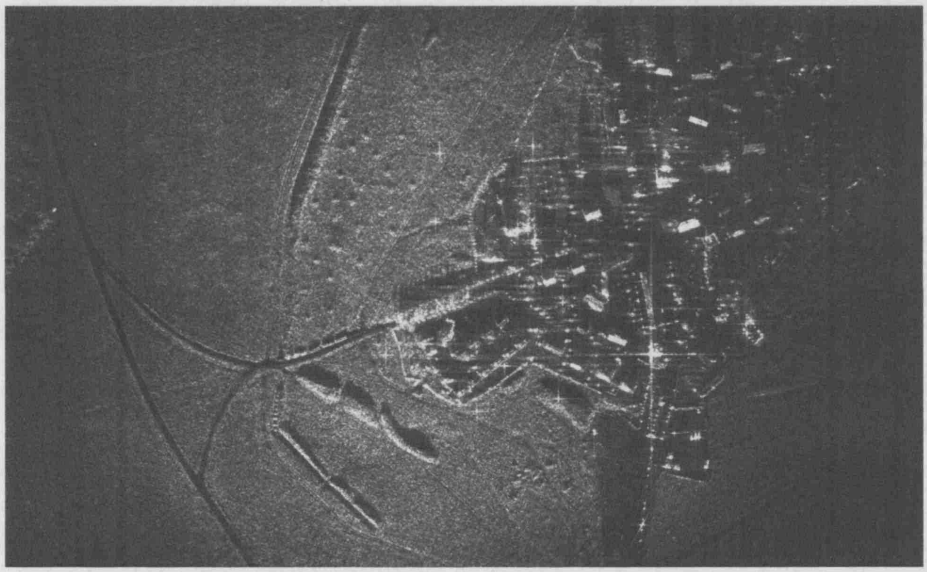

Figure 8-13 Monostatic image from leg 7

For the next few images comparing particular features of the target, the monostatic image has been rotated to be orientated along the same vector as the bistatic one.

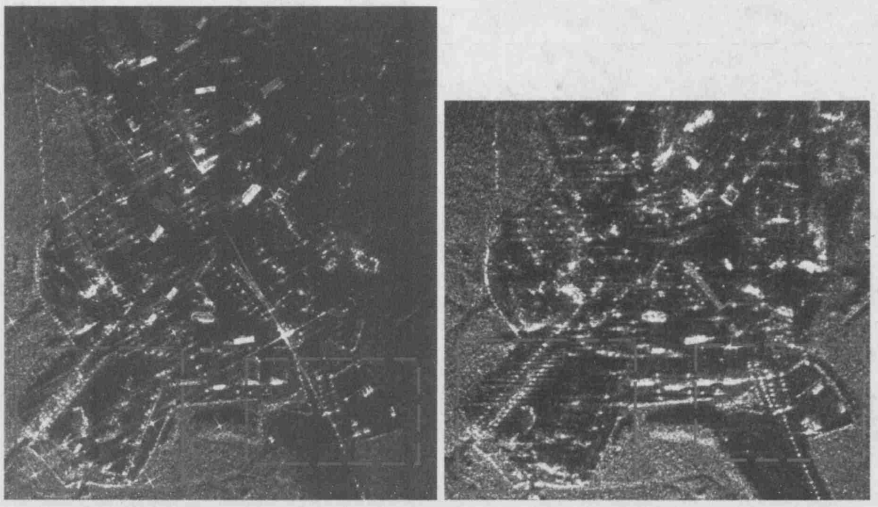

Figure 8-14 Monostatic and bistatic village from leg 7

There are less bright sidelobes in the bistatic image than in the monostatic one. This manifests as smears from each bright point in the monostatic image. This makes the bistatic image clearer, and easier to interpret. Again, due to the fairly low grazing angle of both platforms, there is considerable shadowing inside the village.

It can be seen that similar buildings are providing the bright returns in both images. The structure of the roof is complicated by its corrugated nature. The main return is from the roofs when they are orientated so their normal approximately bisects the bistatic angle (hence it is the houses whose roofs appear as approximately horizontal in bistatic imagery which provide the high returns). This is only approximate with a few degrees of acceptance in this orientation. Again, the fenced roof building is visible towards the top of both images. The barn with metal supports is again clearly visible in the monostatic image, but its return is different in the bistatic one. It seems that the bistatic return is from part of the roof at this particular geometry.

Since the monostatic image is time coincident, from position 1, rather than bisecting the bistatic angle, position 2, different buildings return the brightest signal from their roof. In both cases it is the roofs around the bisector of the imaging geometry.

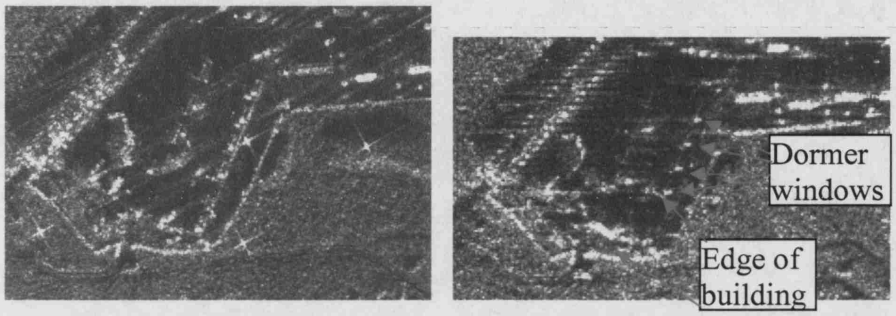

Figure 8-15 Monostatic and bistatic image from leg 7, dormer houses

The row of dormer houses returns an unusual signature in the bistatic image, Figure 8-15. The first row (towards the bottom-right of the image) shows a return from the side of the first house furthest to the left plus a return from the front edge. Then there is a gap where there used to be a house. The next house along shows a return similar to the first with both the side and front edges being visible. The rest of the row has a very slight return from the front of each house. The main return from each house in that row is from the centre of each building. This return is from the dormer window in each of the roofs, showing up as a flash in the centre of each house. The second row of houses is not as clearly visible, with only a small return from the front of each house plus the side of the first one. This is because on this row, the dormer windows are on the other side (facing north) and so are not visible.

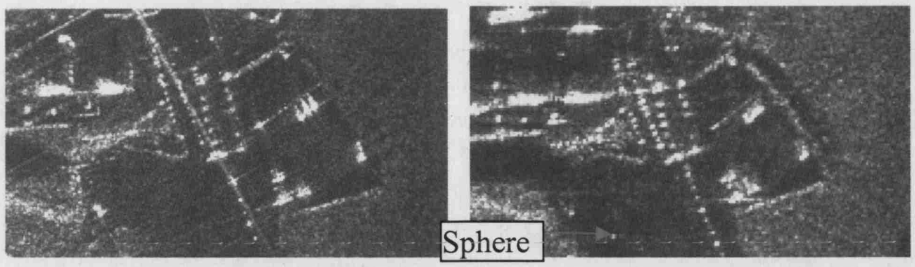

Figure 8-16 Monostatic and bistatic image from leg 7, car park

The southern sphere in the car park can be seen in the bistatic image (towards the bottom left of the dark car parks), Figure 8-16, but the position of the other sphere is not clear. It is not really possible to see either sphere in the monostatic image. Up and left of the sphere is a van, more visible in the monostatic image. In the right hand side of the car park, 7 vehicles can be made out from the monostatic image. The three vehicles parked together towards the top right of the car park are not distinguishable in the bistatic image. The three vehicles towards the bottom of the image are also not as well defined as in the monostatic image.

8.4 Imaging leg 11

Again data was collected with ESR transmitting the higher bandwidth, now with ADAS at a higher grazing angle, approximately three times that of ESR. The data recorded is to the south of scene centre. The bistatic image can be seen in Figure E-9. Parts of this image have been extracted for closer analysis.

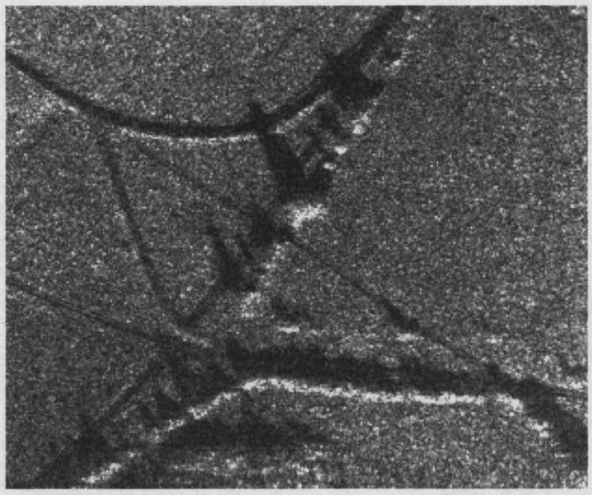

Figure 8-17 Extract from the bistatic image from leg 11

Figure 8-17 shows that shadows from the trees at the bottom of the image have noticeably changed. The long shadow pointing up and left remains the same (from ESR), however the shadow pointing up and right is noticeably shortened by the high grazing angle of ADAS.

With this higher grazing angle, more of the urban area is visible (as it is not in the receiver shadow). Also, the three vehicles in the car park have now been clearly resolved into three objects. However, the sphere in the car park is not so clearly visible.

To look at the effects of higher grazing angles, imagery from legs 7 and 11 are compared in Figure 8-18. Leg 7 has a similar bistatic angle with both platforms at 9° grazing angle. Due to the speeds of the platforms, the image from leg 7 requires less data than that from leg 11. There was also an antenna pointing problem with ADAS on leg 11 which is likely to be the cause of the car park appearing less dark than in leg 7.

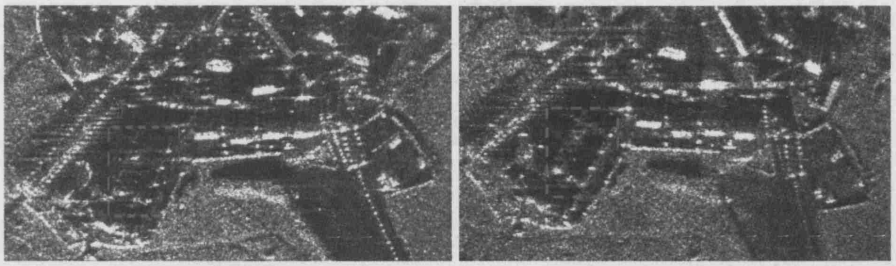

Figure 8-18 Bistatic legs 7 and 11 images of the village

Only a small part of the village is available in the processed image from leg 11. The buildings that return the brightest signatures in image 7 are also visible in image 11. In the image from leg 11 the single storey building is also visible.. The vehicles in the car park in leg 11 are easier to interpret, however this could be due to the contrast settings in the image display. The return from the dormer houses is noticeably different. In the lower receiver grazing angle case, the main return is from the dormer windows in the middle of each roof. At the higher grazing angle the dormer windows are not visible, the main return is from the side of the building.

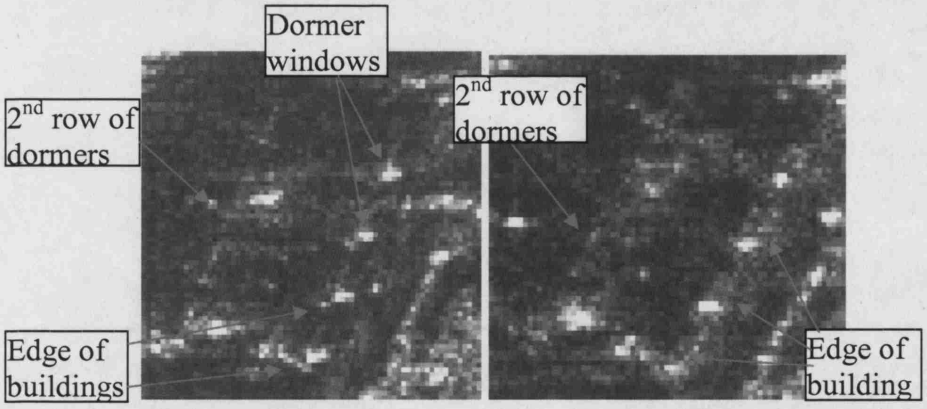

Figure 8-19 Dormers from bistatic images from leg 7 and 11

The corresponding leg 11 monostatic image from position 1, *i.e.* time coincident, has been processed to the same resolution as the bistatic image. The data used to process the monostatic image is collected slightly to the north of

the previous images. The car parks are close to the bottom of the image and appear blurred. In the next images, the time coincident monostatic image has been rotated to be orientated in the same direction as the bistatic one. The first image, Figure 8-20, is of the part of the village from the bistatic image.

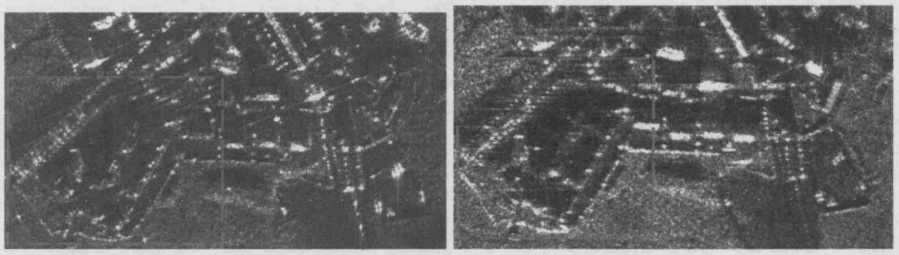

Figure 8-20 Monostatic and bistatic image of village from leg11

The cars in the car park look similar in both images. In the monostatic image they are brighter, but this causes high sidelobes and slight saturation. As they are close to the end of the recording window they are also starting to appear blurred. Again, the trihedrals are not visible in the bistatic image.

For the first time, the long single storey building is visible in the bistatic image. Its return in the coincident monostatic image is not as bright, but still visible. It both cases it is marked by the oval in Figure 8-20. Both images look remarkably similar. This is because the main shadow is from the transmitter, which is the same in both images. The bistatic image has less variation in the strength of scatterers which tends to bring up the contrast within the fields and make them appear more speckled.

Rotating the monostatic image makes the sidelobes more obvious. The sidelobe level in the monostatic image now appears to be greater than in the bistatic

image. However, the monostatic image does not have an autofocus solution applied to it.

Although the whole of the village is not visible in this image, it is possible to tell that the interpretability is greatly increased by the reduction in shadowing from the receiver being at high grazing angles.

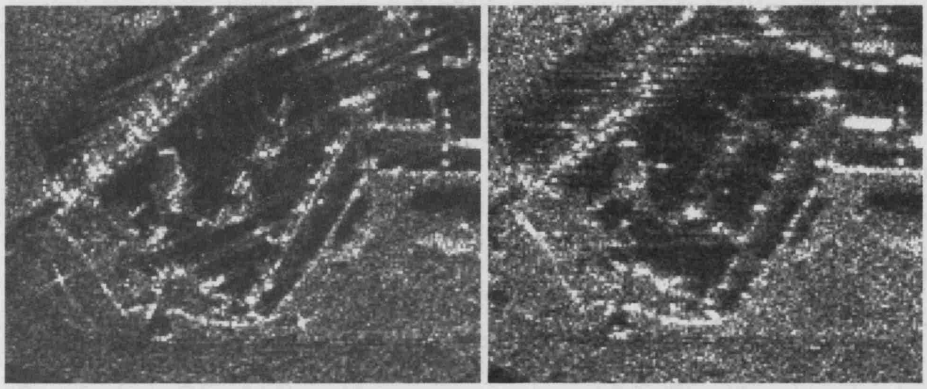

Figure 8-21 Monostatic and bistatic image of dormers from leg 11

In the bistatic image the return from the row of dormer houses is mainly from the left edge of each building. The flash from the dormer window is not visible with ADAS at the higher grazing angle. The second row of dormers has a flash from the end of the last house, but very little return from the rest of the row although it is possible to work out where they are. In the monostatic image both rows are clearly visible.

8.5 Imaging leg 13

For this imaging run, ESR was transmitting the higher bandwidth. ADAS flying at a fast rate in the same sense as ESR, with both platforms at 9° grazing angle.

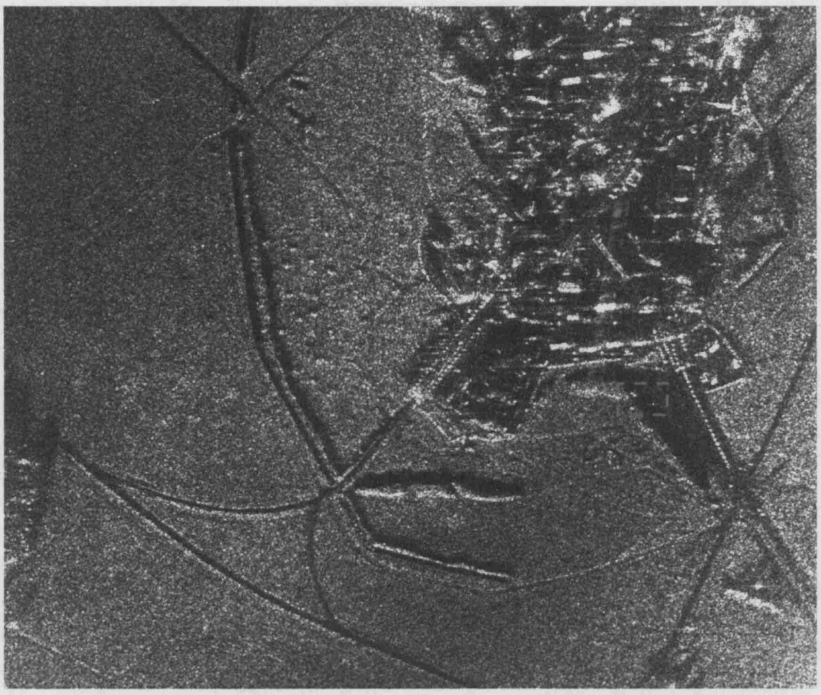

Figure 8-22 Bistatic image from leg 13

From the tree at the very bottom of the image it is possible to tell that the two platforms are at similar grazing angles as the two shadows are the same length. The sphere is visible in the car park in front of the van, highlighted by the dashed square in Figure 8-22.

Figure 8-23 shows the coincident monostatic image from leg 13, processed to the same resolution as the bistatic one above.

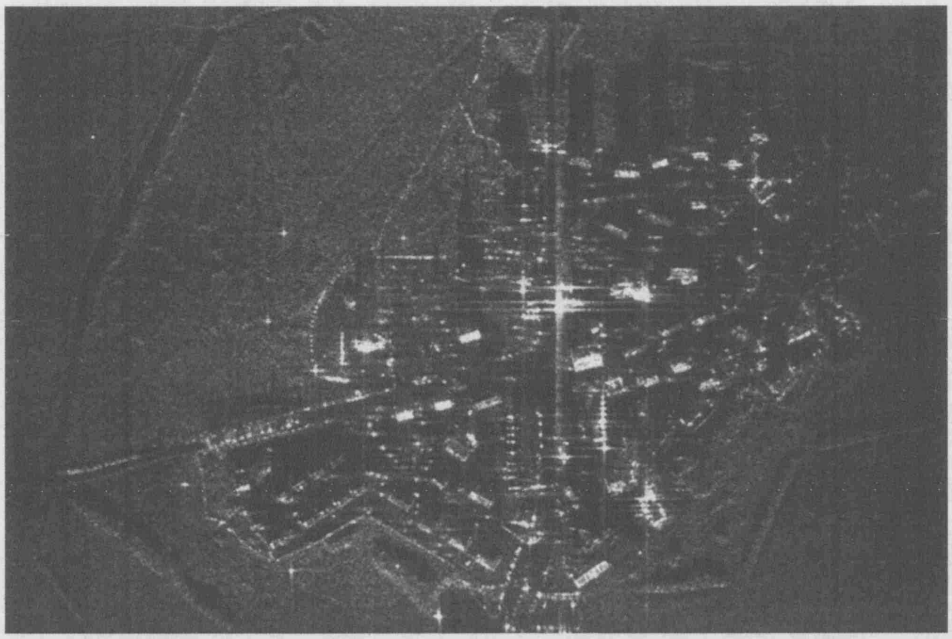

Figure 8-23 Monostatic image from leg 13

The posts marking the scene centre are visible. There is a flash from a large barn towards the centre of the village, which is slightly saturating the image. This has the effect of obscuring the area around it with sidelobe energy. The return from the barn with metal supports plus other buildings is also starting to saturate the image.

In the following images, the time coincident monostatic image above is rotated to be orientated the same way as the bistatic image. Specific areas of the images have been used for comparison. Firstly, the village itself.

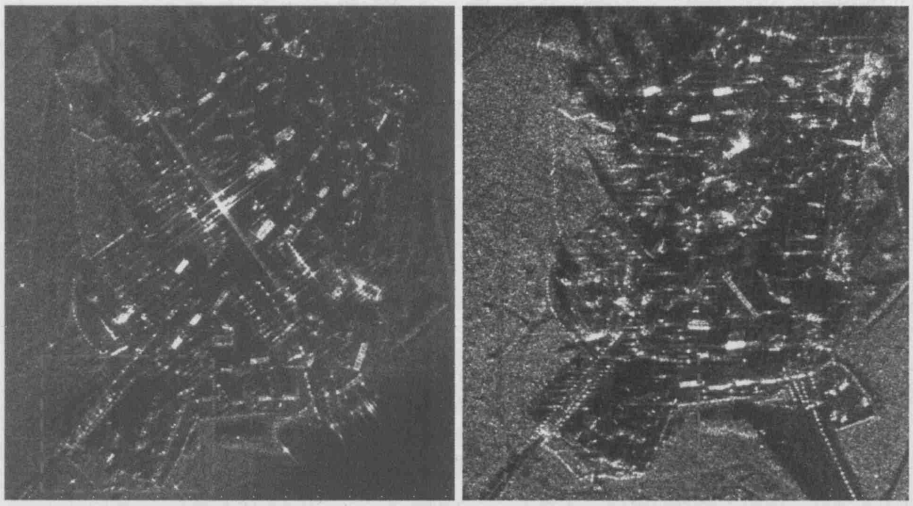

Figure 8-24 Monostatic and bistatic images of village from leg 13

There is no bright flash in the bistatic image. The building to the right and up slightly from this bright flash appears the same in both images. The barn with metal supports is clearly visible in the monostatic image, but is not in the bistatic image. Generally it is different roofs which appear bright in the different images. Within an image, the roofs that show up the brightest have a similar orientation. This orientation is around the centre of the aperture in the monostatic case and around the bisector of the bistatic angle in the bistatic case.

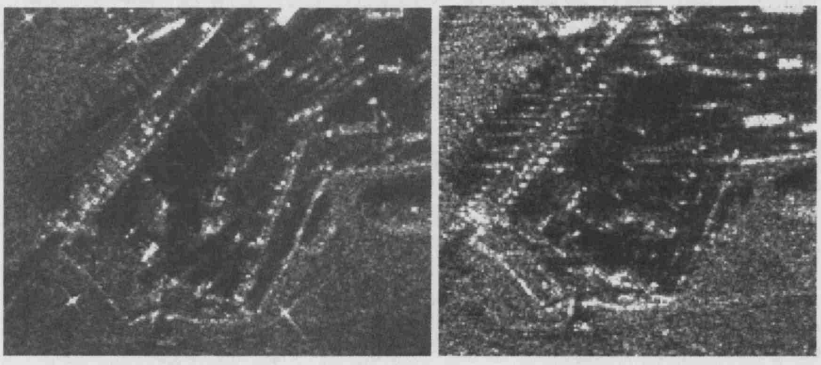

Figure 8-25 Monostatic and bistatic image of dormers from leg 13

In the bistatic image in Figure 8-25, the main return is flashes from the dormer windows in the roof, but there is a small return from the side of the houses. Again the return from the second row of dormers is markedly less. There is just the weak return from the side of each building. In the monostatic image both rows of houses are visible.

8.6 Conclusions

This work has tried to characterise some of the features of bistatic SAR imagery. Due to the nature of the target, it is hard to draw any specific conclusions. As shown in the monostatic imagery, viewing the scene from slightly different angles changes the brightness of the features in the image. The highly complicated structure of the corrugated tiled roof is highlighted, becoming bright and then fading again within fractions of a degree of aperture squint. This work has been able to show that there are many similarities between the bistatic image and the corresponding monostatic one. A clear difference is that none of the trihedrals and dihedrals are visible in the bistatic images presented, as expected. Also, the intensity of data appears to have less variation in the bistatic images

The clutter characteristics from both images have been analysed. Both were shown to fit the K probability distribution well. This shows that there is a similar scattering mechanism in both the bistatic imaging and monostatic imaging. The monostatic imagery appears to come from a K distribution with a larger shape parameter than the bistatic imagery, *i.e.* the monostatic clutter is spikier than the bistatic. This may mean that point targets are more detectable in bistatic imagery than monostatic imagery.

The nature of the two shadows will affect the utility of the image. More of the scene in shadow could obscure important information. The amount of shadow depends on the bistatic angle and both platform grazing angles. The higher the grazing angle and the lower the bistatic angle the less shadow. Imagery has been presented at different bistatic angles and different grazing angles to demonstrate this.

Chapter 9. Modelling of bistatic SAR target characteristics

9.1 Introduction

This section examines the characteristics of bistatic SAR imagery through the utilisation of scattering prediction code. The work uses simulated ISAR imagery of a CAD model of a simplified T72 tank. The bistatic images are compared to the corresponding monostatic ones. A wall is introduced into the CAD model to demonstrate the effect of shadowing in bistatic imagery.

The simulated ISAR imagery in this section has been produced by Daniel Andre.

9.2 Radar cross section (RCS) prediction code.

There are two main RCS prediction tools with the functionality of producing bistatic plots. These are FACETS™, reference [32], and Spectre (formerly RESPECT, [33]).

FACETS™ is a well documented and established tool. However, it requires prior knowledge of scattering interactions between objects (or facets) *i.e.* multipath. As the prediction code is being used to model complex objects bistatically, this information is not known. Indeed this is part of what is under investigation.

Spectre is a high frequency RCS prediction tool developed by QinetiQ at Portsdown West to model the RCS of large complex targets. The code has been in operation for over ten years and has been thoroughly validated against measured data. Spectre requires minimal intervention from the user. For example, unlike FACETS™, the multipath interacting facets are all found automatically. For this reason Spectre was chosen as the prediction tool for this work.

Spectre models scattering effects through a combination of geometrical optics (GO) and physical optics (PO). Spectre also incorporates the physical theory of diffraction (PTD) when required.

All plots are given in terms of a rotation angle of the CAD model α. Results are obtained by rotating the CAD model around while keeping the transmitter and receiver stationary.

9.3 Canonical scatterers

Initially simple point target scatterers were used. This allowed the results from Spectre to be compared with analytical expressions for RCS calculated by Daniel Andre. This served to validate the results from Spectre. A flat plate and a dihedral were examined. The results from Spectre and the analytical work were found to be in agreement. Details of this work can be found in [29].

9.4 Complex scatterers

This section presents ISAR image Spectre predictions for a simplified CAD model of a T72 shown in Figure 9-1.

In the prediction runs, the multipath interaction order was set to *three*, *i.e.* up to three bounces were modelled. Multipath interactions of higher order were ignored as setting the interaction order much higher considerably increases the program run-time. It is hoped that the brightest multipath interactions are accounted for, and that the main bistatic multipath features will be visible, and interpretable, to some extent.

The T72 ISAR images can be seen in Figure 9-2 through to Figure 9-5. The resolution is 10cm in both range and azimuth and the centre frequency is 9.75GHz. Both the platforms have an elevation of 9°. The image is always formed by modelling the radar to be up-the-page from the CAD model. In the monostatic case, the transceiver is always directly up the page. In the bistatic case, the transmitter is top right, and the receiver is top left. The bistatic image is formed along the bisector of the bistatic angle.

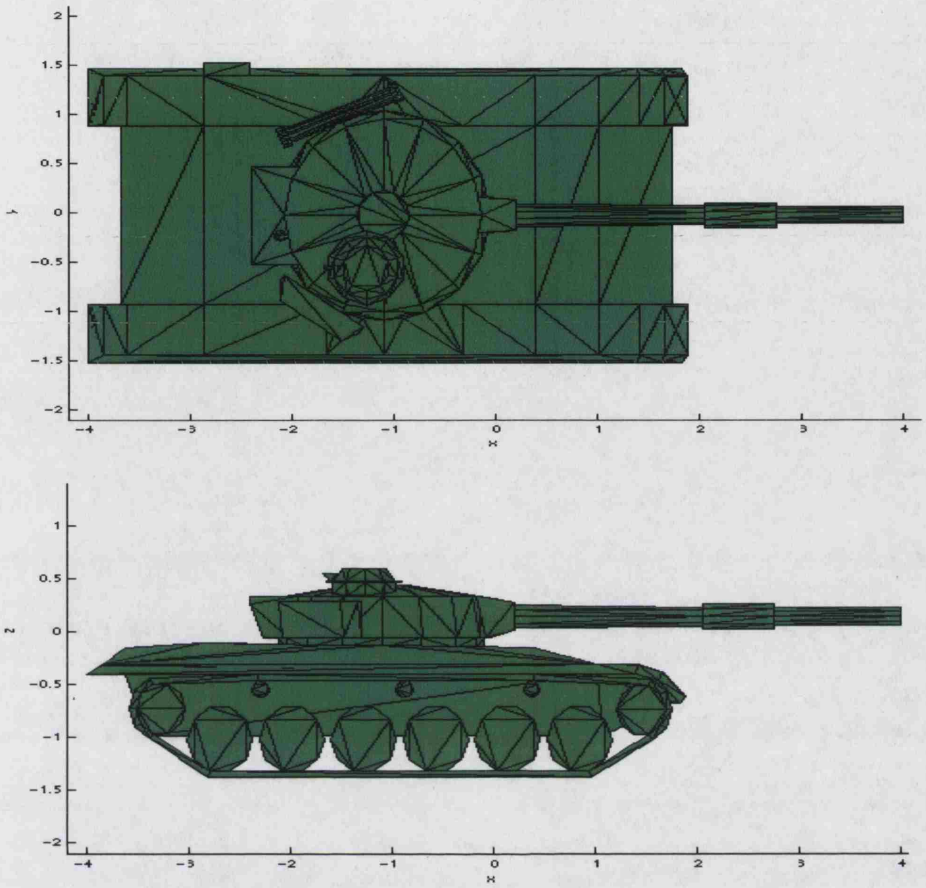

Figure 9-1 CAD model of simplified T72

In each of the sets of ISAR images, the left-hand image is the monostatic results (β=0), the centre image is with β=30° and the image on the right is using β=60°. The first ISAR image is with the tank facing upwards. In successive images, the CAD model is rotated anticlockwise by 22.5°.

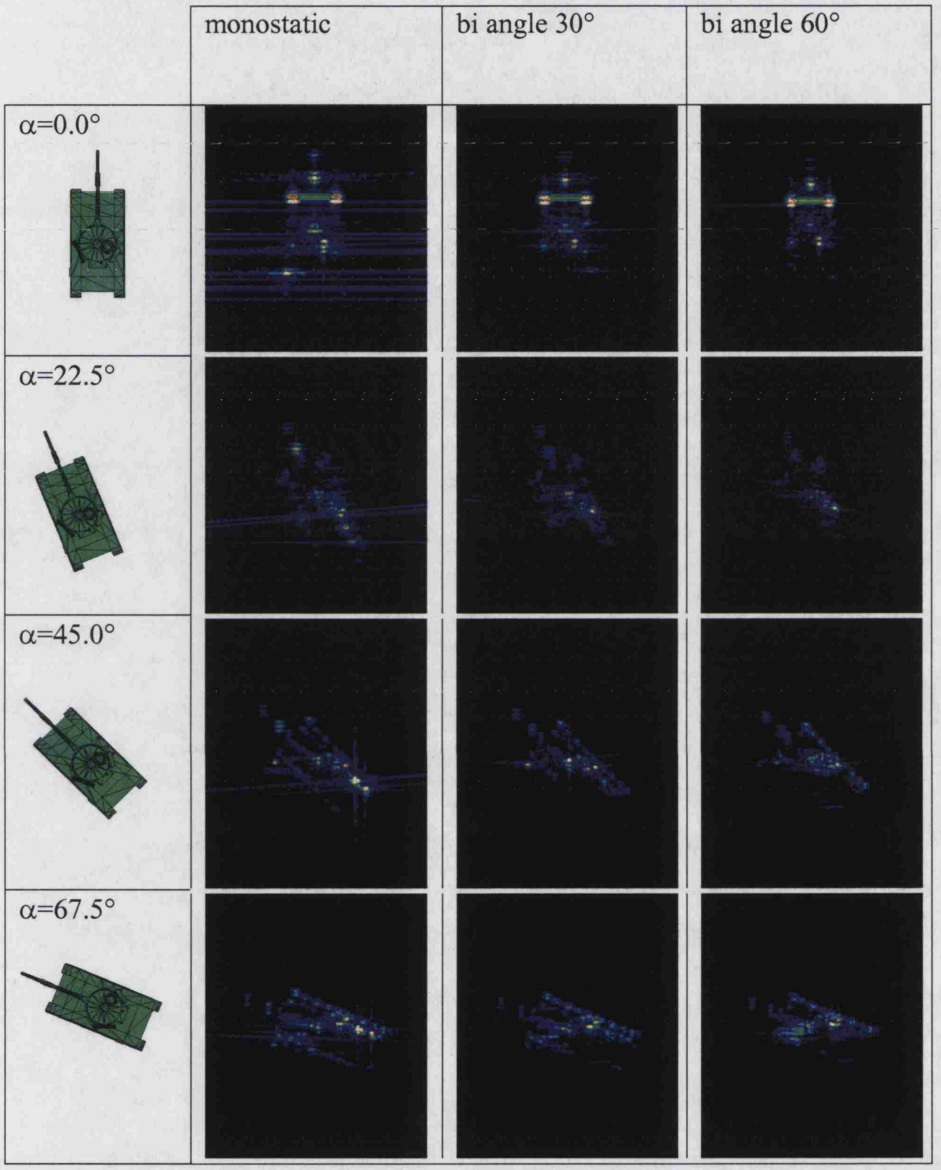

Figure 9-2 SAR images of T72 for α=0° to 67.5°, in 22.5° steps.

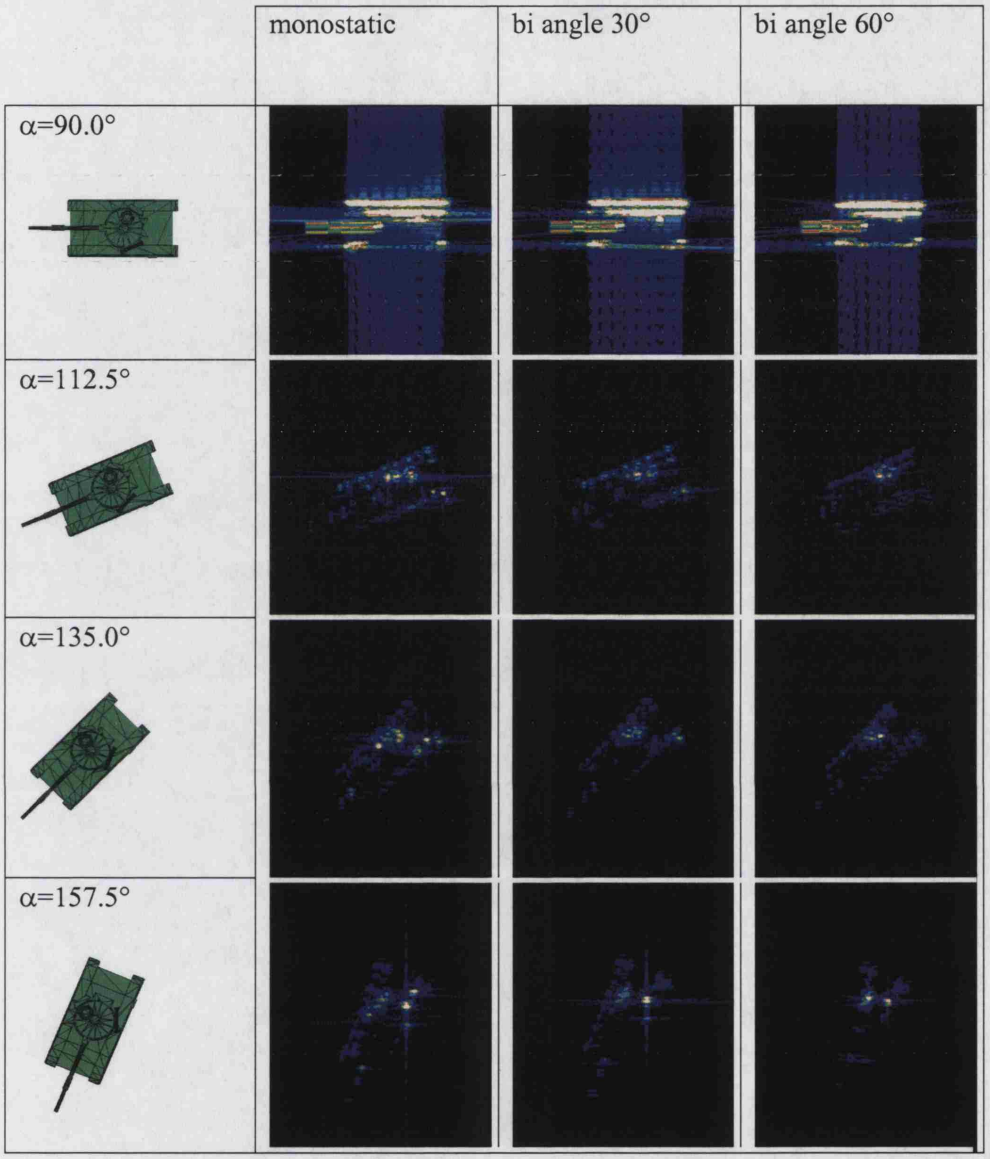

Figure 9-3 SAR images of T72 for α=90° to 157.5°, in 22.5° steps

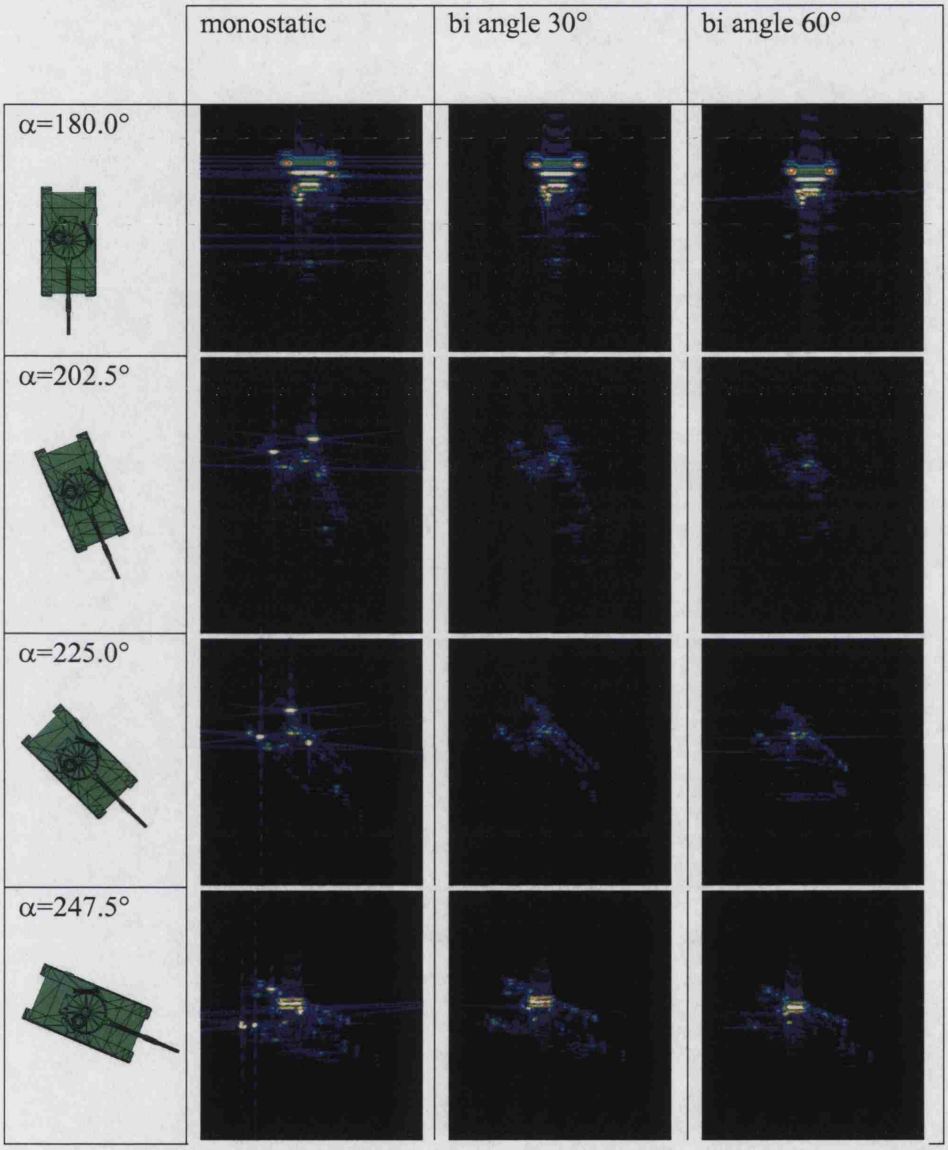

Figure 9-4 SAR images of T72 for α=180° to 247.5°, in 22.5° steps

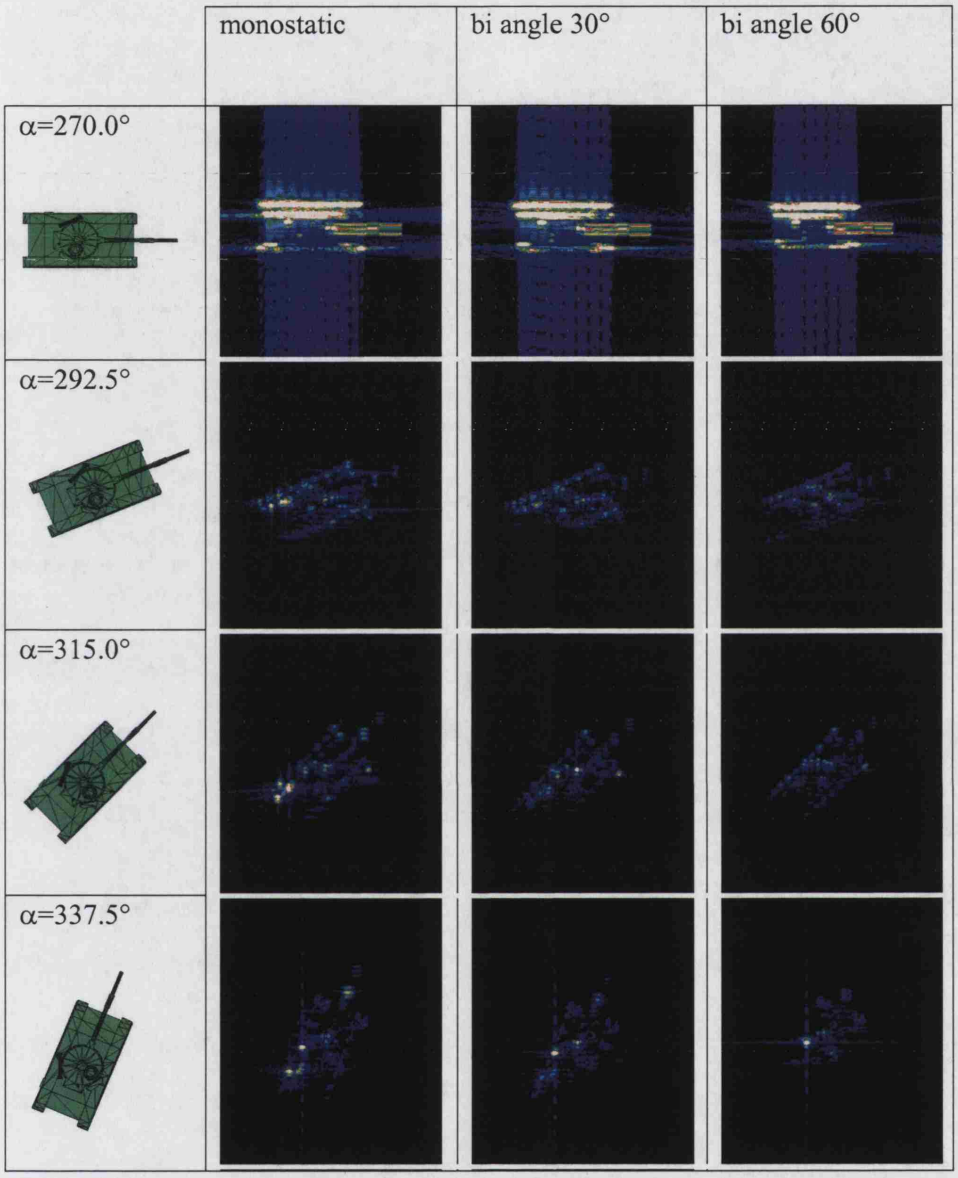

Figure 9-5 SAR images of T72 for α=270° to 337.5°, in 22.5° steps

All the images have the same scaling, making their displayed colour scale comparable. The monostatic return is generally brighter than the bistatic one. This is shown, for example, by the sidelobes in the monostatic image at α=0. The amplitude of the return decreases with increasing bistatic angle.

The bistatic images suffer from more self-shadowing. That is, due to the separate transmitter and receiver, more parts of the T72 are shadowed by other parts of it. As the bistatic angle increases the amount of self shadowing also increases, and less of the target can be seen.

With α=225°, in Figure 9-4, multipath is noticeable on the 60° bistatic angle case. This is probably coming from multipath under the tank. This is highlighted in the repeated image in Figure 9-6.

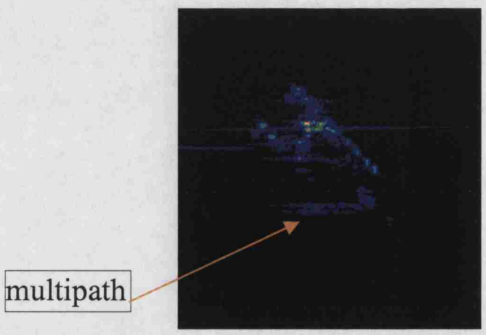

Figure 9-6 SAR image of a T72 with α =225°, β=60° with multipath highlighted

In the image with α=247.5°, in Figure 9-4, the small snorkel towards the back of the tank produces a bright return with all three bistatic angles. An example with bistatic angle of 30° is shown in Figure 9-7.

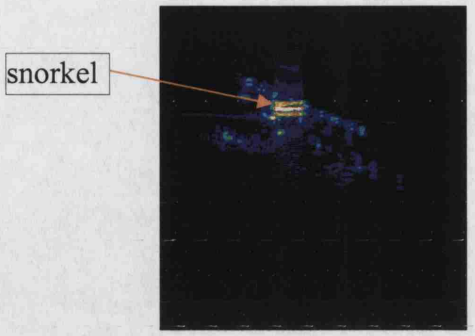

Figure 9-7 SAR image of a T72 with α =247.5°, β=30° with snorkel highlighted

To understand better bistatic shadowing and multipath effects, simulations were carried out with a wall placed next to the T72 CAD model, Figure 9-8. This also simulates targets within an urban environment. The wall is situated 2.5m from the tank. It is modelled as a flat, perfectly conducting plate of width is 9m, and height is 4m. When the radar platform elevation is 9°, the wall can completely obscure the T72. Due to diffraction effects, the ends of the wall can often be seen in the image.

In the prediction runs, the multipath interaction order was again set to *three*. The T72 ISAR images can be seen in Figure 9-9 through to Figure 9-12. The resolution is 10cm and the centre frequency is 9.75GHz. The radar platform elevation is 9° for both platforms.

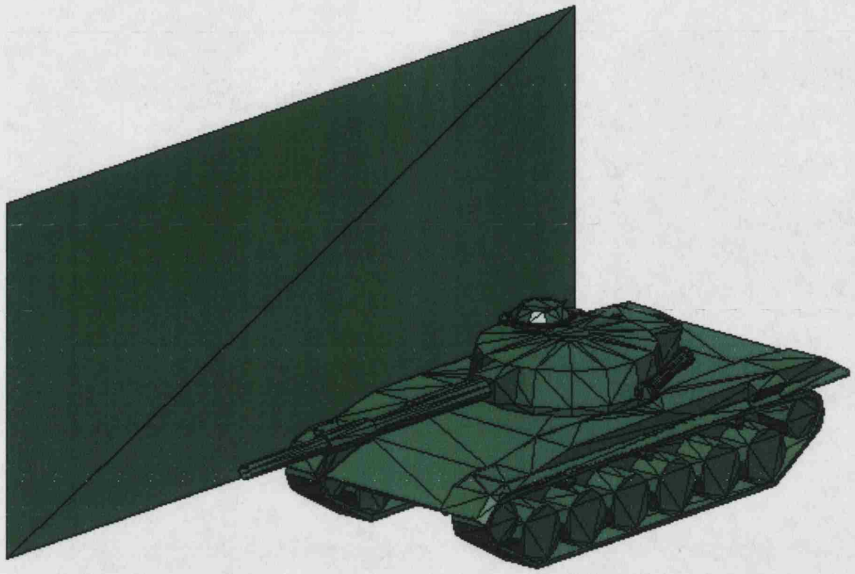

Figure 9-8 A 3-D view of a CAD model of the simplified T72 tank next to a wall.

Figure 9-9 through to Figure 9-11 show the SAR images of the T72 by a wall for bistatic angle, β, of a)0°, b)30°, c)60° (from left to right). The first image is orientated with α=0°. At α=0° the wall is to the right of the T72 and the front of the T72 is facing the top of the page. Again, the model is then rotated anticlockwise to produce the successive images spaced at rotations of 22.5°.

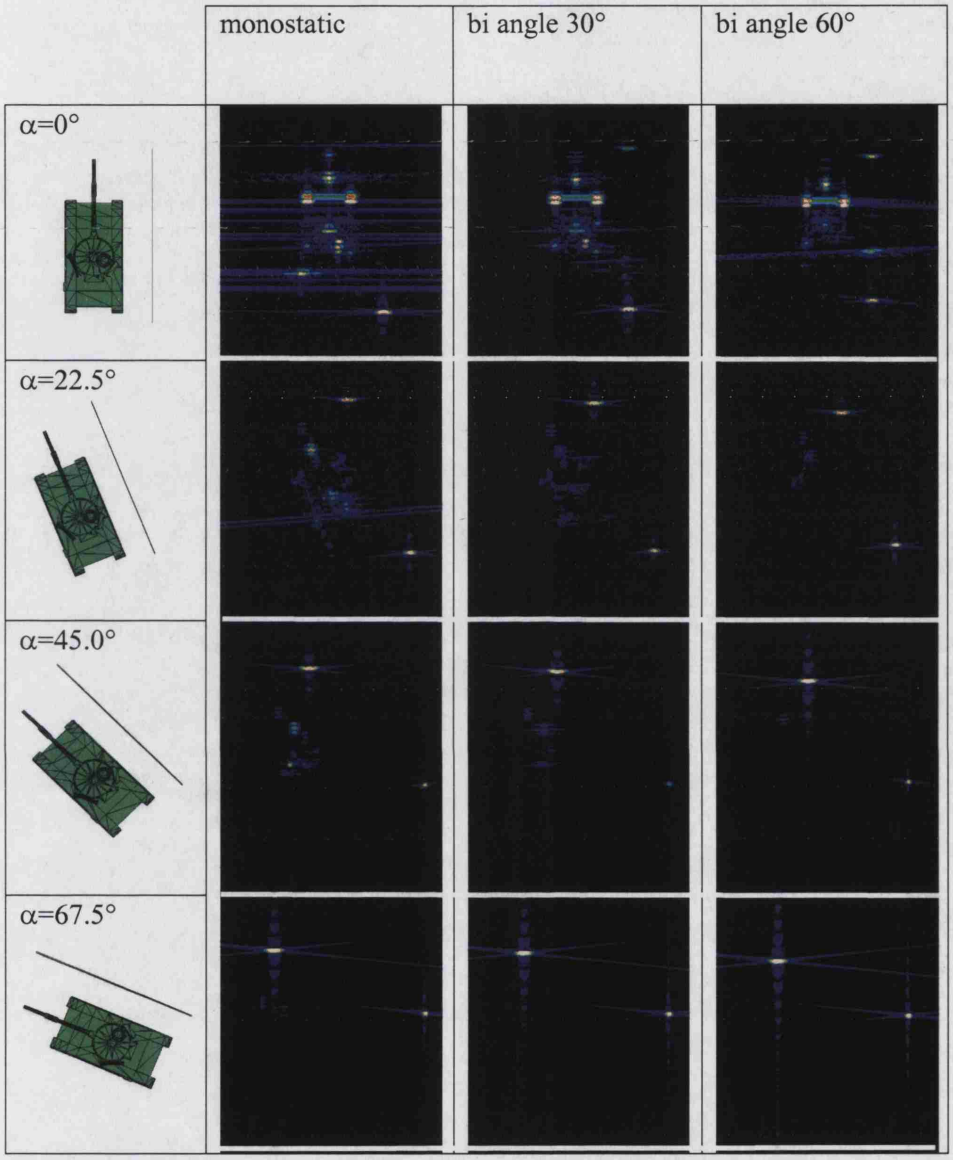

Figure 9-9 SAR images of T72 next to a wall for α=0° to 67.5°, in 22.5° steps.

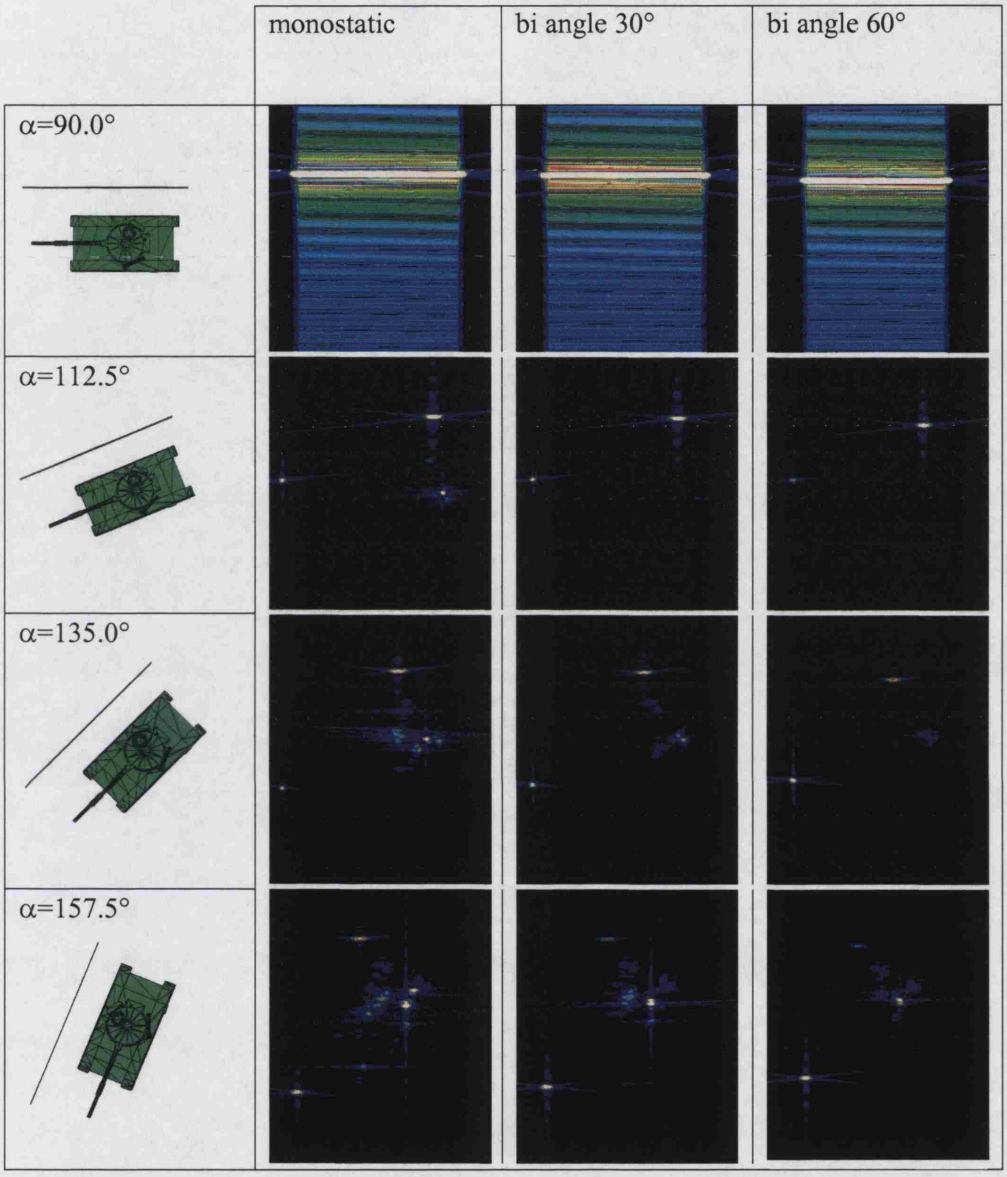

Figure 9-10 SAR images of T72 next to a wall for α=90° to 157.5°, in 22.5° steps

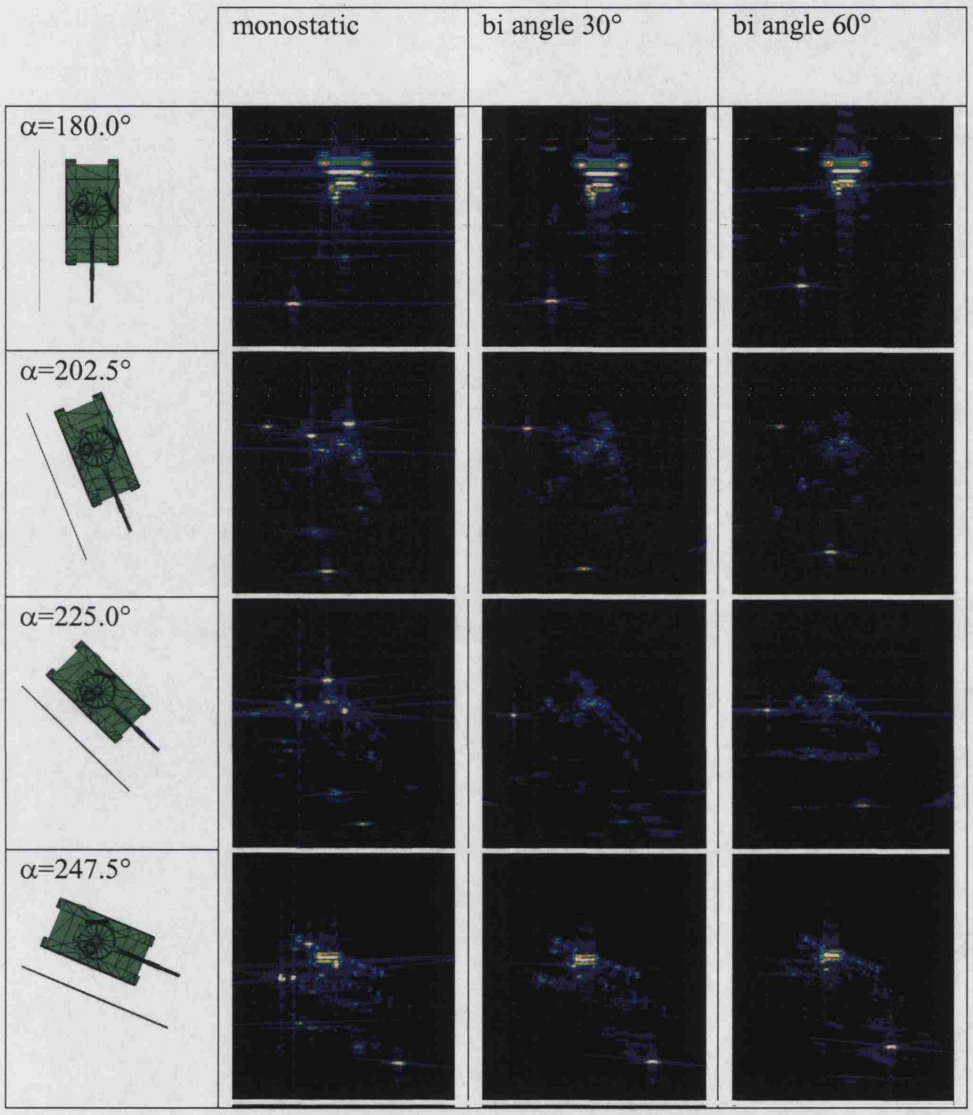

Figure 9-11 SAR images of T72 next to a wall for α=180° to 247.5°, in 22.5° steps

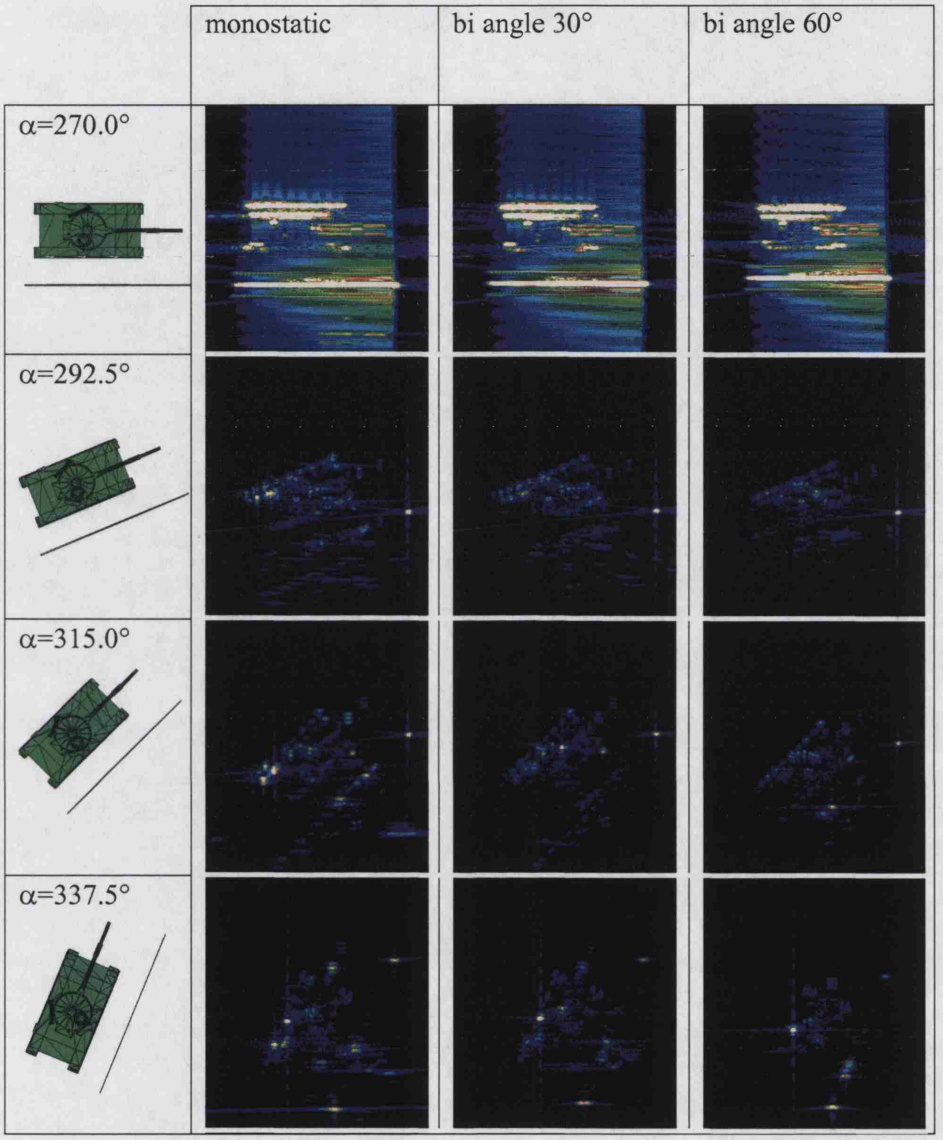

Figure 9-12 SAR images of T72 next to a wall for α=270° to 337.5°, in 22.5° steps.

The first two figures, Figure 9-9 and Figure 9-10, have the wall generally above the tank. These show the additional shadowing effects introduced by the wall. With the latter two images, Figure 9-11 and Figure 9-12, the wall is generally below the tank. Here the tank is inside the dihedral formed by the wall and the ground, so these images suffer more from multipath effects.

Again, the fact that the monostatic return is higher than the bistatic one is apparent from the images. With $\alpha=0°$, the monostatic image appears to have high sidelobes due to the scaling of the images. In the first images with $\alpha=0$, the diffracting effect of both ends of the wall can be seen.

The effects of the shadowing can easily be seen. The inclusion of the wall means that the tank is often in shadow. The amount of shadow increases as the bistatic angle increases from 0° to 60°. This is obvious in Figure 9-10 with $\alpha=135°$ and a bistatic angle of 60° where very little of the tank is visible. Whereas in the monostatic case considerably more of the tank is recognisable.

In Figure 9-11, the multipath effects appear more apparent in the bistatic cases. For example, with a bistatic angle of 60° and $\alpha=180°$, there are appears to be a return to the left where there are no scatterers. This is multipath. This is also obvious when $\alpha=225°$ in both bistatic cases.

With Figure 9-12, there appear to be more multipath effects in the monostatic case than in the bistatic cases. This is because of the imaging geometry. The monostatic images are formed along a vector bisecting the bistatic angle. Another comparison would be to compare the monostatic images formed along the bistatic transmitter or receiver vectors.

9.5 Summary

This work examined the scattering characteristics of complex scatterers, in this case a T72 tank. The tank has been modelled monostatically and with bistatic angles of 30° and 60°.

The bistatic images are subject to additional shadowing from the two separated platforms. In the analysis of the T72 on its own, this took the form of self-shadowing. This might be able to give additional information about the relative heights of different parts of the vehicle and aid ATR.

A wall was then added to the CAD model of the T72 tank. This work has demonstrated the shadowing effects inherent in bistatic SAR imaging. It has also given more insight into the multipath effects.

The modelling work shows that the image utility of bistatic SAR is comparable with monostatic SAR. This confirms the results from the bistatic experiment. The only additional burden on image interpretability comes from the extra shadow and the multipath effects.

More investigation is required to increase the understanding of the nature of the complex bistatic scattering in the simulated ISAR imagery, *i.e.* the multipath scattering centres. Only three bounces have been considered due to the computation run times involved. The effect of additional bounces would provide additional information.

Further study is also required to gain a better understanding of the utility of bistatic SAR imagery. It is currently unclear as to whether the bistatic image offers any real advantages over the monostatic image (for the case where both

images are available). For example the reduced clutter from dihedrals may aid target detection for bistatic imaging. Also questions such as what additional information could be gained if both the monostatic and bistatic images were available need to be examined.

Chapter 10. Conclusions

The theory of bistatic SAR resolution has been developed analytically. This has shown the effect of platform velocity and bistatic angle on the resolution obtainable. The expressions have been verified using a simple 'point by point' processor. This is a processor in its simplest form. It works accurately, but is computationally inefficient. To create a system that is operationally viable, faster image processing is required. For this reason, the adaptation of existing processing algorithms used in monostatic SAR has been investigated.

The PFA interpolation has been adapted for bistatic use via three different approaches. The results have been compared in terms of scene size limitations. The novel mathematical approach developed by Andrew Horne has been shown to be far superior to the other methods examined here.

The inclusion of altitude in the problem has been addressed. The resulting out-of-plane motion has, as expected, produced tighter constraints on scene size. The radius of an acceptable scene has decreased from approximately 150m to 50m in some cases. Although this would be limiting, this section shows that PFA is a viable option for bistatic operation.

The scene size limitation is a known drawback of monostatic PFA. This leads us to look at a more advanced processing algorithm, namely the Range Migration Algorithm (RMA) which, monostatically, does not suffer from such scene size limitations. The difficulty with trying to adapt the RMA for bistatic

geometries lies in the more complicated expression for phase. An analytical expression for the phase after matched filtering is not available. This leaves the form of the bistatic equivalent of the Stolt interpolation unclear. Work has examined the phase of targets after the matched filtering stage. Simple forms of distortion have been applied and the phase of the output examined. A systematic optimisation approach has been implemented, but this has been unsuccessful. It is unlikely that this method would reveal a good enough approximation for the distortion for high-resolution images to be obtained. The way forward with the bistatic adaptation of RMA is, as yet, unclear.

A sophisticated fully versatile bistatic SAR processor has been written by Andrew Horne based around his bistatic variation of the polar format image formation algorithm. The processor is completely independent of the imaging geometry or radars used. The processor has been used to process the bistatic data from the fully airborne demonstration. Examining this imagery, the scene size limitations imposed by using PFA seem to have no noticeable effect.

Due to time constraints a simple, versatile stand-alone autofocus has been implemented. This autofocus is equally applicable to monostatic and bistatic SAR imagery. However, it is apparent from the imagery that some regions are better focused than others, and some types of structure are better focused than others. The regional dependence is related to the type of scatterers in that region and how their signature is affected by the defocusing phase errors, and to the phase errors that defocus any dominating targets.

The route taken in realising the full airborne trial of bistatic SAR along with the trial itself has been detailed. This has included ground trials with analysis of the

data to derisk the airborne demonstration. Details of some of the experiments flown at the full airborne trial have been given, along with the processed imagery from some of the legs.

The results of the fully airborne bistatic SAR trial presented in Chapter 7 are a UK first. High-resolution bistatic SAR imagery has been formed using two separate airborne platforms not constrained to flying any particular trajectory using considerable bistatic angles and squint angles. This demonstrated capability has major implications for counter jamming and counter vulnerability of future SAR sensors.

The imagery from the trial has been examined in detail and compared with the corresponding monostatic imagery. This work has tried to characterise some of the features of bistatic SAR imagery. Due to the nature of the target (an urban environment), it is hard to draw any specific conclusions. As shown in the monostatic imagery, viewing the scene from slightly different angles changes the main features in the image. The highly complex structure of the tiled roofs show a Bragg scattering effect, becoming bright and then fading again within fractions of a degree of aperture squint. A clear difference is that none of the trihedrals are visible in the bistatic images. Also, the intensity of data appears to have less variation in the bistatic images.

This work has been able to show that there are many similarities between the bistatic image and the corresponding monostatic one. For example, the clutter characteristics from both the monostatic and bistatic images from the trial have been analysed. Both were shown to be consistent with the K probability density

function. This suggests that there is a similar scattering mechanism in both the bistatic imaging and monostatic imaging scenarios.

The nature of the two shadows will affect the utility and interpretability of the image. The amount of shadow is dependent on the bistatic angle and both platform grazing angles. The higher the grazing angle and the lower the bistatic angle the less shadow formed. Imagery has been presented at different bistatic angles and different grazing angles to demonstrate this.

The prediction code Spectre has been used to form simulated ISAR imagery in order to look at the scattering characteristics of more complex scatterers, in this case a T72 tank. Simulated ISAR imagery of A CAD model of T72 has been modelled monostatically and with bistatic angles of 30° and 60°. The bistatic images are subject to additional shadowing from the two separated platforms. In the analysis of the T72 on its own, this took the form of self-shadowing. This might be able to give additional information about the relative heights of different parts of the vehicle and aid ATR. A wall was then added to the CAD model of the T72 tank. This work has demonstrated the shadowing effects inherent in bistatic SAR imaging. It has also given more insight into the multipath effects.

The modelling work shows that the image utility of bistatic SAR is comparable with monostatic SAR. This confirms the results from the bistatic experiment. It appears that the only additional burden on image interpretability comes from the extra shadow. Effects such as multipath have a different realisation in bistatic imaging. More investigation is required to increase the understanding of the nature of the complex bistatic scattering in the simulated SAR imagery, *i.e.* the

multipath scattering centres. Only three bounces have been considered due to the computation run times involved. The effect of additional bounces would provide additional information.

Chapter 11. Future work

The following topics are being examined to further the bistatic SAR work presented here:

- Using the bistatic imagery from the fully airborne demonstration, calculate radar cross section (RCS) values for the fields and urban areas in the imagery. The effect of bistatic angle and grazing angle on RCS could be examined. This would provide some quantitative analysis on the imagery and the effect of bistatic angle and grazing angle.

- To extend the RCS prediction work on bistatic SAR target characteristics to examine real ISAR data. Bistatic measurements have been taken of vehicles on a turntable. These need to be processed and the target characteristics analysed.

- To further the utility of bistatic SAR imagery by examining effects such as the shadowing, layover (where objects out of the ground plane appear closer to the radar) and multipath to see if bistatic imaging can help to reduce these effects.

- To use the RCS prediction tool to model ISAR imagery from urban areas. It is hoped this will provide a greater understanding of the scattering mechanisms present in the complex urban environment.

- To study the additional utility of SAR imagery if both the monostatic and bistatic images are available. This includes using the additional shadowing information to estimate an object's height, to provide more information on the terrain. This extends to looking at how to use multiple images (from multistatic operation) for optimum utility.

Other topic which need to explored further for bistatic SAR to become a viable imaging scenario are:

- To develop a robust autofocus which can correct motion errors in both platform positions.

- To develop a deeper understanding of the effect of bistatic SAR imagery on existing SAR image interpretation tools such as Automatic Target Recognition (ATR). Ultimately these tools will need to be adapted so that they are equally applicable to monostatic or bistatic SAR imagery.

- More robust and operational methods of synchronising the two platforms needs to be developed. Particularly to allow bistatic imaging to occur when both platforms are operating from different locations (that is they cannot be brought together prior to the imaging run).

- The effect of polarimetry in bistatic imaging would also be an interesting topic to explore.

A Monostatic SAR resolution theory

Assume that the platform is moving parallel to the x-axis, with a point scatterer at position (x_t, y_t). R_0 denotes the broadside range from the platform to scene centre, R denotes the range from the platform's current position, at a displacement x from broadside, to the target.

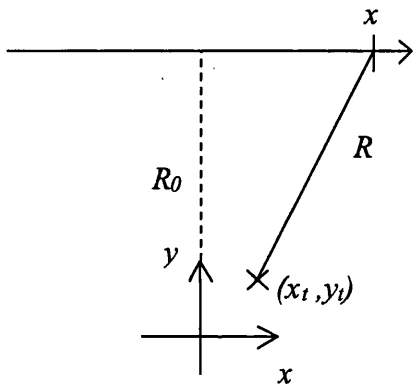

Figure A-1 Monostatic geometry

From Pythagoras' Theorem:

$$R_t^2 = (R_0 - y_t)^2 + (x - x_t)^2, \tag{39}$$

or

$$R_t = (R_0 - y_t)\sqrt{1 + \frac{(x - x_t)^2}{(R_0 - y_t)^2}}. \tag{40}$$

Mixing out the returns from scene centre:

$$\Delta R = (R_0 - y_t)\sqrt{1+\frac{(x-x_t)^2}{(R_0-y_t)^2}} - R_0\sqrt{1+\frac{x^2}{{R_0}^2}}. \qquad (41)$$

Using the binomial theorem to expand equation *(41)*, neglecting terms of order $1/R_0^3$ and above gives:

$$\begin{aligned}\Delta R &\approx (R_0 - y_t)\left(1+\frac{1}{2}\frac{(x-x_t)^2}{(R_0-y_t)^2}\right) - R_0\left(1+\frac{1}{2}\frac{x^2}{{R_0}^2}\right) \\ &\approx -y_t + \frac{1}{2}\left(\frac{y_t x^2 - 2R_0 x_t x + R_0 {x_t}^2}{R_0(R_0-y_t)}\right).\end{aligned} \qquad (42)$$

The phase of the return signal takes the form:

$$s(f,t) = \exp(i\phi), \qquad (43)$$

where $\phi = \frac{4\pi}{c}\Delta R(f_0+f)$, $-\frac{B}{2} \le f \le +\frac{B}{2}$, B is the bandwidth, f_0 is the centre frequency and c is the speed of light.

Here $\phi = \frac{2\pi}{c}(f_0+f)\left(-2y_t + \frac{y_t x^2 - 2R_0 x_t x + R_0 {x_t}^2}{R_0(R_0-y_t)}\right)$.

Noting f_0, x_t, y_t are constants and letting $f_0, R_0 >> f, x, x_t, y_t$

$$\phi \approx \phi_0 + \frac{2\pi}{c}\left(-\frac{2f_0 x_t x}{R_0} - 2y_t f\right). \qquad (44)$$

Integrating this with a matched filter:

$$H(x,f) = \exp i\left(\frac{4\pi}{c}\frac{f_0 \sigma_x x}{R_0} + \frac{4\pi f}{c}\sigma_y\right), \qquad (45)$$

(where (σ_x, σ_y) is a hypothesised target) gives the response to the point target (neglecting the constant) of:

$$s(x,y)=\int_{-L/2}^{L/2}\exp\left(-i\frac{4\pi f\ x}{cR_0}(x_t-\sigma_x)\right)dx\int_{-B/2}^{B/2}\exp\left(-i\frac{4\pi f}{c}(y_t-\sigma_y)\right)df \qquad (46)$$

Evaluating the integrals gives:

$$s(x,y)\propto \operatorname{sinc}\left(\frac{2\pi f_0}{R_0 c}(x_t-\sigma_x)L\right)\operatorname{sinc}\left(\frac{2\pi}{c}(y_t-\sigma_y)B\right) \qquad (47)$$

This gives the zero-to-null resolutions in the azimuth and range dimensions as:

$$\rho_x=\frac{cR_0}{2f_0L} \text{ and}$$

$$\rho_y=\frac{c}{2B} \text{ respectively.}$$

B Explanation of mathematics between equations *(16)* and *(17)*

The aim of this appendix is to fill in a little of the detail from Chapter 3, between equation *(16)* and *(17)*. This is highly mathematical and would probably just confuse if it were given in the chapter. However, for those keen to follow the steps it is necessary to include this.

Equation *(16)* is repeated here:

$$\phi_{VAR} \approx \frac{-4\pi f}{c}\cos\left(\frac{\alpha_0-\beta_0}{2}\right)\left[x_t\cos\left(\frac{\alpha_0+\beta_0}{2}\right)+y_t\sin\left(\frac{\alpha_0+\beta_0}{2}\right)\right] + \frac{2\pi f_0 t}{c}\left[\frac{v_T x_t\sin\alpha_0 - v_T y_0\cos\alpha_0}{R_{0T}} + \frac{v_R x_t\sin\beta_0 - v_R y_t\cos\beta_0}{R_{0R}}\right]. \quad (48)$$

This can be rewritten as:

$$\phi_{VAR} \approx \frac{-4\pi f}{c}\cos\left(\frac{\alpha_0-\beta_0}{2}\right)\left[x_t\cos\left(\frac{\alpha_0+\beta_0}{2}\right)+y_t\sin\left(\frac{\alpha_0+\beta_0}{2}\right)\right] - \frac{2\pi f_0 t}{c}\left[-\left(\frac{v_T\sin\alpha_0}{R_{0T}}+\frac{v_R\sin\beta_0}{R_{0R}}\right)x_t+\left(\frac{v_T\cos\alpha_0}{R_{0T}}+\frac{v_R\cos\beta_0}{R_{0R}}\right)y_t\right]. \quad (49)$$

Now define a right angled triangle such that:

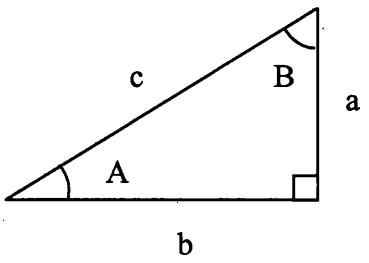

Figure B-2 Right-angled triangle

where $a = \frac{v_T \cos\alpha_0}{R_{0T}} + \frac{v_R \cos\beta_0}{R_{0R}}$, $b = \frac{v_T \sin\alpha_0}{R_{0T}} + \frac{v_R \sin\beta_0}{R_{0R}}$,

$c = \sqrt{a^2 + b^2}$. Noting that $\Delta\alpha = \frac{v_T}{R_{0T}}$ and $\Delta\beta = \frac{v_R}{R_{0R}}$. These can be rewritten as $a = \Delta\alpha\cos\alpha_0 + \Delta\beta\cos\beta_0$, $b = \Delta\alpha\sin\alpha_0 + \Delta\beta\sin\beta_0$.

Equation *(49)*, above, then becomes:

$$\phi_{VAR} \approx \frac{-4\pi f}{c}\cos\left(\frac{\alpha_0 - \beta_0}{2}\right)\left[x_t\cos\left(\frac{\alpha_0 + \beta_0}{2}\right) + y_t\sin\left(\frac{\alpha_0 + \beta_0}{2}\right)\right] - \frac{2\pi f_0 t}{c}\left[-bx_t + ay_t\right] \quad (50)$$

Which can also be written as:

$$\phi_{VAR} \approx \frac{-4\pi f}{c}\cos\left(\frac{\alpha_0 - \beta_0}{2}\right)\left[x_t\cos\left(\frac{\alpha_0 + \beta_0}{2}\right) + y_t\sin\left(\frac{\alpha_0 + \beta_0}{2}\right)\right] - \frac{2\pi f_0 t}{c}\sqrt{a^2 + b^2}\left[\frac{-bx_t}{\sqrt{a^2 + b^2}} + \frac{ay_t}{\sqrt{a^2 + b^2}}\right]. \quad (51)$$

This then simplifies to:

$$\phi_{VAR} \approx \frac{-4\pi f}{c}\cos\left(\frac{\alpha_0 - \beta_0}{2}\right)\left[x_t\cos\left(\frac{\alpha_0 + \beta_0}{2}\right) + y_t\sin\left(\frac{\alpha_0 + \beta_0}{2}\right)\right] - \frac{2\pi f_0 t}{c}\sqrt{a^2 + b^2}\left[-x_t\cos(A) + y_t\sin(A)\right] \quad (52)$$

From the triangle in Figure B-2, A=arctan*(a/b)*. Using this, equation (52) can be rewritten as:

$$\phi_{VAR} \approx \frac{-4\pi f}{c}\cos\left(\frac{\alpha_0 - \beta_0}{2}\right)\left[x_t\cos\left(\frac{\alpha_0 + \beta_0}{2}\right) + y_t\sin\left(\frac{\alpha_0 + \beta_0}{2}\right)\right] - \frac{2\pi f_0 t}{c}\sqrt{a^2 + b^2}\left[x_t\cos\left(\arctan\left(\frac{a}{b}\right)\right) - y_t\sin\left(\arctan\left(\frac{a}{b}\right)\right)\right]. \quad (53)$$

Which can also be written as:

$$\phi_{VAR} \approx \frac{-4\pi f}{c}\cos\left(\frac{\alpha_0-\beta_0}{2}\right)\left[x_t\cos\left(\frac{\alpha_0+\beta_0}{2}\right)+y_t\sin\left(\frac{\alpha_0+\beta_0}{2}\right)\right]$$
$$-\frac{2\pi f_0 t}{c}\sqrt{a^2+b^2}\left[x_t\cos\left(\arctan\left(-\frac{a}{b}\right)\right)+y_t\sin\left(\arctan\left(-\frac{a}{b}\right)\right)\right] \qquad (54)$$

Replacing *a, b* with their definitions from Figure B-2 gives an equation which is identical to equation *(17)* in the main body of the thesis.

C Zero-to-null resolution compared to -3dB

The point spread function is given by:

$$\rho(t) = \int_{-\infty}^{+\infty} e^{-2\pi f t i} A(f) \mathrm{d}f \qquad (55)$$

Here, the signal has the form:

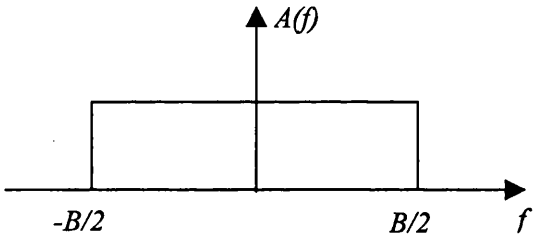

Figure C-3 Signal

Where *A(f)* equals 1 for *f* between *–B/2* and *B/2* and zero elsewhere (*B* is the bandwidth of the signal). So,

$$\rho(t) = \int_{-B/2}^{B/2} e^{-2\pi f t i} \mathrm{d}f$$

$$= \left[\frac{e^{-2\pi f t i}}{-2\pi t i} \right]_{-B/2}^{B/2}$$

$$= \frac{-1}{2\pi t i} \left[e^{-\pi B t i} - e^{\pi B t i} \right]$$

$$= \frac{1}{2\pi t} \sin(\pi B t)$$

$$= \frac{B}{2}\mathrm{sinc}(\pi Bt)$$

The -3dB value is half power which is $1/\sqrt{2}$ of the amplitude. The value of t is required when $\rho(t)=1/\sqrt{2}$, *i.e.*

$$\mathrm{sinc}(\pi Bt) = \frac{1}{\sqrt{2}} \tag{56}$$

or,

$$\sin(\pi Bt) = \pi Bt/\sqrt{2} \tag{57}$$

This has to be solved iteratively *i.e.*

$$t_{n+1} = \sqrt{2}\sin(\pi Bt_n)/\pi B \tag{58}$$

Substituting a bandwidth of 500MHz, an initial value for t_0, this converges to give t= 0.88589.

Thus the -3dB resolution is a factor of approximately 0.89 times the zero-to-null resolution, given by $c/2B$ in the monostatic range case.

D Ellipse extension of PFA

The equation of the tangent at scene centre of the iso-range ellipse which passes through scene centre is required. To do this, the coordinates of the scene centre in the (α,β) frame need to be found. This needs the understanding of the transformation required from one coordinate frame to the other.

Imagine the iso-range contour passing through scene centre. This is an ellipse with the transmitter and receiver as the foci, shown in Figure D-4. The transmitter has coordinates (x_T,y_T) and the receiver has coordinates (x_R,y_R) both in the (x,y) frame. As the platforms move, this ellipse changes. Below is one such ellipse.

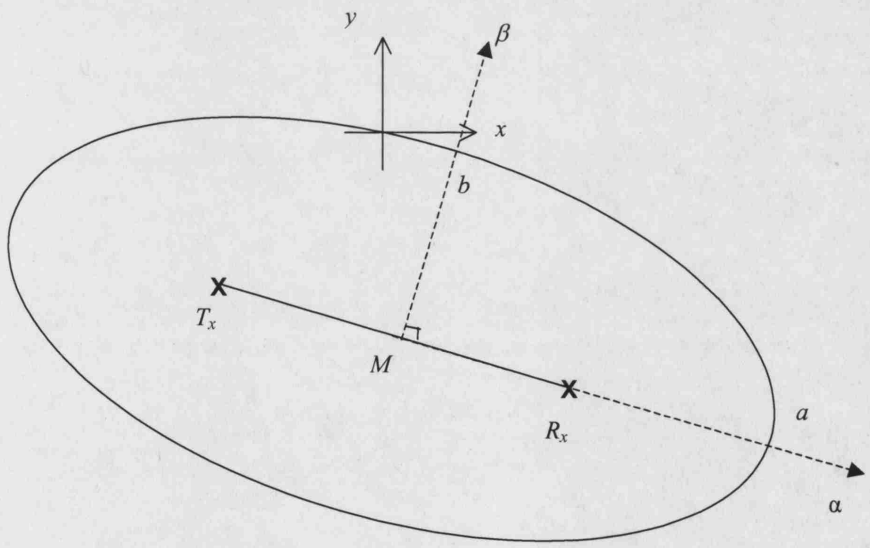

Figure D-4 Ellipse geometry

M is the mid point along the line joining the transmitter and receiver and has coordinates $((x_T+x_R)/2,(y_T+y_R)/2)$ in the (x,y) frame. The point a is where the ellipse crosses the α axis, b is where the ellipse crosses the β axis.

The equation of the ellipse in the (α,β) coordinate frame is given by:

$$\frac{\alpha^2}{a^2}+\frac{\beta^2}{b^2}=1 \qquad (59)$$

where $a=\frac{R_T+R_R}{2}$ or $\frac{\sqrt{x_T^{\,2}+y_T^{\,2}}+\sqrt{x_R^{\,2}+y_R^{\,2}}}{2}$ and $b=\sqrt{a^2-\left(\frac{x_T-x_R}{2}\right)^2-\left(\frac{y_T-y_R}{2}\right)^2}$.

Firstly this needs a coordinate transformation into the (x,y) scene frame. This requires a translation of this ellipse to move the point M to the origin of the (x,y) frame, then a rotation about the origin through an angle theta.

Firstly apply the translation; this is a shift by $-M$. It will help to label this intermediate coordinate frame by (α',β'), as shown in Figure D-5.

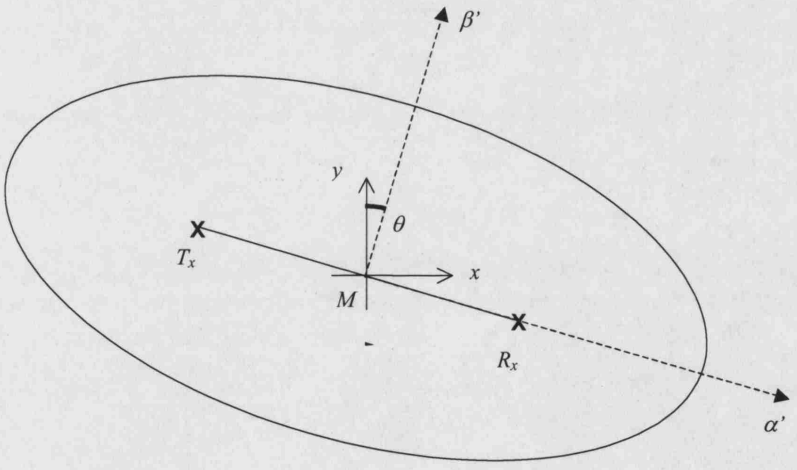

Figure D-5 Ellipse transformation

Then a rotation through angle θ, where $\theta = \arctan\left(\frac{y_T - y_R}{x_T - x_R}\right)$.

Thus the gradient of the ellipse $\frac{\alpha^2}{a^2} + \frac{\beta^2}{b^2} = 1$ at the point $\left(\frac{x_T + x_R}{2}\cos\theta - \frac{y_T + y_R}{2}\sin\theta, \frac{x_T + x_R}{2}\sin\theta + \frac{y_T + y_R}{2}\cos\theta\right)$ is required.

The equation for the ellipse can be written as:

$$\beta = b\sqrt{1 - \frac{\alpha^2}{a^2}} \tag{60}$$

The equation for the gradient is then given by:

$$\frac{d\beta}{d\alpha} = -\frac{\alpha b}{a^2}\left(1 - \frac{\alpha^2}{a^2}\right)^{-1/2} \tag{61}$$

Evaluating this at the point of interest gives the gradient as:

$$-\frac{\alpha_0 b}{a^2}\left(1 - \frac{\alpha_0^2}{a^2}\right)^{-1/2} \tag{62}$$

where $\alpha_0 = \frac{x_T + x_R}{2}\cos\theta - \frac{y_T + y_R}{2}\sin\theta$

$$\theta = \arctan\left(\frac{y_T - y_R}{x_T - x_R}\right)$$

$$a = \frac{\sqrt{x_T^2 + y_T^2} + \sqrt{x_R^2 + y_R^2}}{2}$$

$$b = \sqrt{a^2 - \left(\frac{x_T - x_R}{2}\right)^2 - \left(\frac{y_T - y_R}{2}\right)^2}\ .$$

E Bistatic imagery from the airborne demonstration

This appendix presents the imagery processed from the bistatic airborne SAR demonstration discussed in Chapter 7. Selected bistatic images are characterised and compared to the monostatic imagery in Chapter 8.

E.1.1 Imaging leg 3

This was one of the lower bandwidth legs. Both platforms were flying at approximately the same angular velocity, at the same grazing angle around a nominal bistatic angle of 30°. The imagery presented below, Figure E-6, is processed from early in the imaging leg. As this is the lower of the two bandwidths used, it means the imagery has a lower range resolution, but a greater scene size.

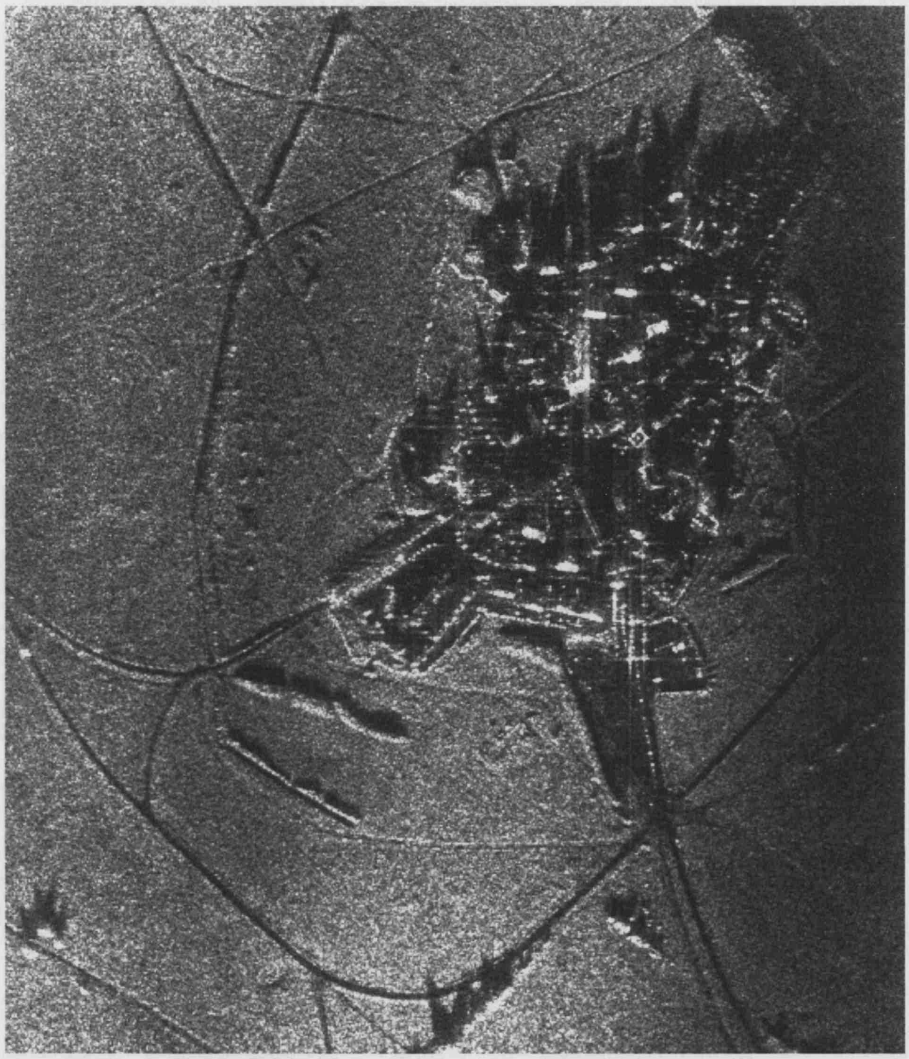

Figure E-6 Bistatic image from leg 3

The resolution measured from the image agrees, broadly, with the resolution requested in the processor. The image is generally well focused. The azimuth smears from the middle of the village on the left-hand side come from young tress. These are likely to be out of focus due to their movement rather than the failure of the autofocus.

As the shadows appear almost black, this implies that the sidelobes levels are sufficiently low and thus the phase noise is acceptable.

E.1.2 Imaging leg 7

This was a high bandwidth imaging leg, which allows a smaller scene to be recorded but the opportunity to process the data to a higher range resolution. The data was collected with both platforms at a similar grazing angle around a nominal bistatic angle of 30°.

Due to problems with the navigation equipment on ADAS, only data very late on in the imaging run has been processed. This means that both of the platforms are heavily squinted. This image, Figure E-7, is formed with ADAS is flying at a faster angular rate than ESR, in the same direction. As shown in Table 7-2, this requires less aperture data to process the image in azimuth. This requires a less accurate motion compensation solution for each platform.

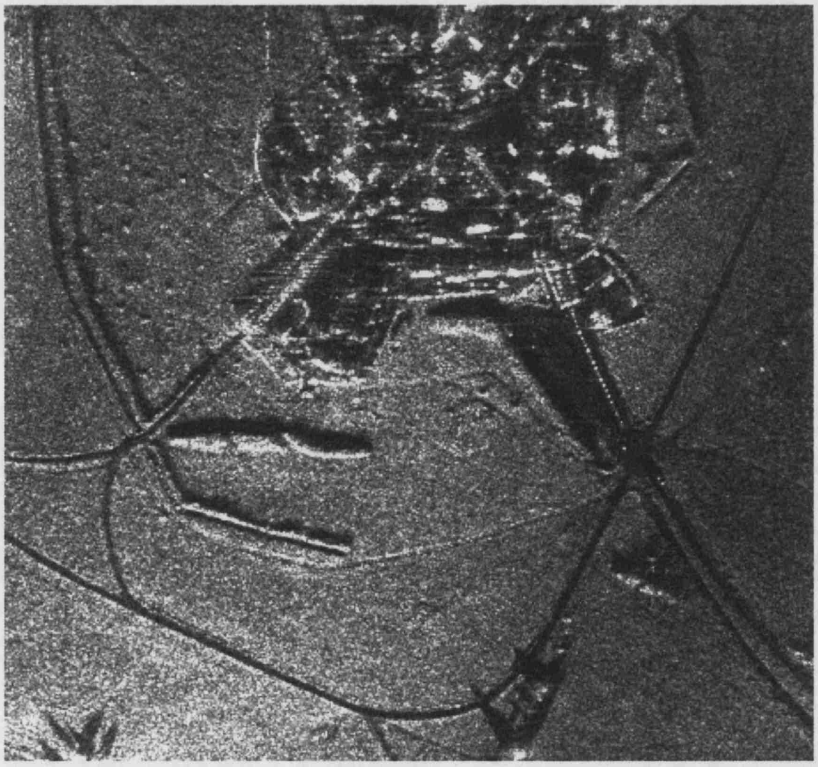

Figure E-7 Bistatic image from leg 7

The resolution requested in the processor in broad agreement with that measured from the image.

Although the autofocus has worked well on the car park area to the south of the scene (where the resolution was measured from), the buildings are out of focus. This is probably due to the fact that the autofocus can only fit one solution to the whole of the image. It tends to ignore high frequency phase errors which could be affecting the whole of the image, but would be more apparent in the urban area.

E.1.3 Imaging leg 10

This leg was with ADAS hovering. From Table 7-2 it can be seen that approximately three times as much data is needed to produce the imagery than in leg 7. Data was collected around a nominal bistatic angle of 30° with ADAS at a grazing angle approximately three times that of ESR. The bistatic image is shown in Figure E-8.

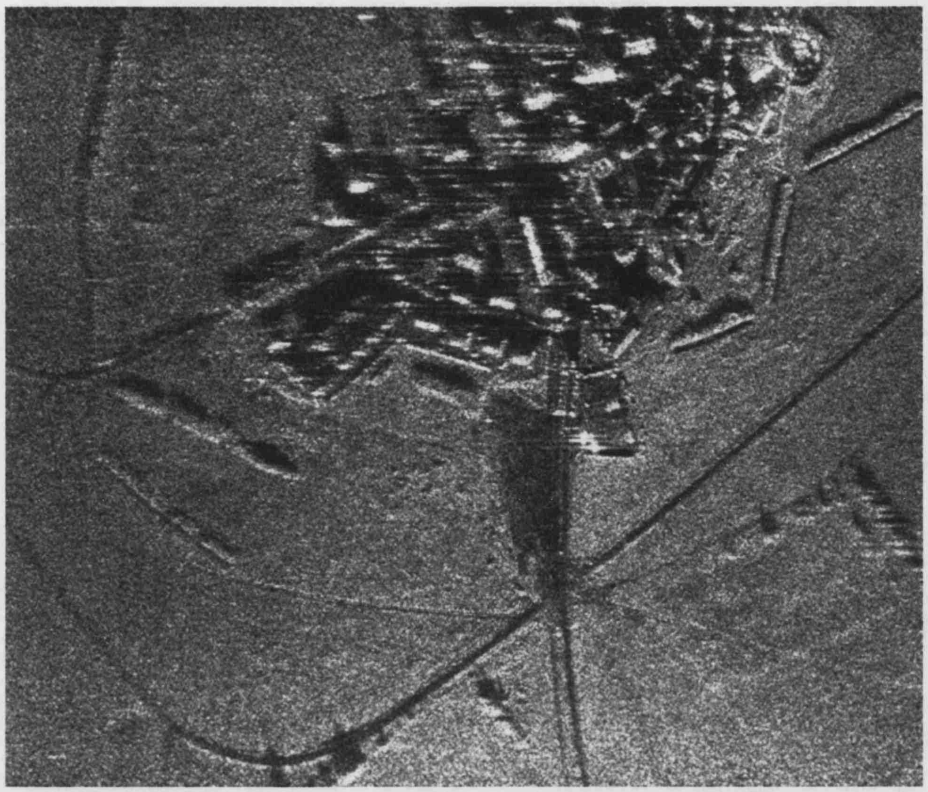

Figure E-8 Bistatic image from leg 10

The quality of this image is a lot poorer than previously presented. The operators of ADAS reported that a good spotlight was not achieved (the ADAS antenna is steered manually). This would reduce image quality as the mainlobe of the radar is not always pointing at the scene, so energy from sidelobes would be integrated up to form the image. The reduction in quality is also likely to be due to the addition data required to process the image. This implies that the motion compensation is adequate over short distances, but not accurate enough for long tracks. The car park area is noticeably not as dark as in previous imagery. This could be due to an increase in phase noise because of the longer aperture time.

There are no discernible point targets which could be used to measure resolution.

E.1.4 Imaging leg 11

Again data was collected with ESR transmitting the higher bandwidth, nominally with a bistatic angle of 30°, with ADAS at a grazing angle three times that of ESR.

The imagery in Figure E-9 is taken towards the beginning of the run. Since ADAS does not have a range variant option, the image is south-west of the target area, *i.e.* the data recording is made too early for scene centre.

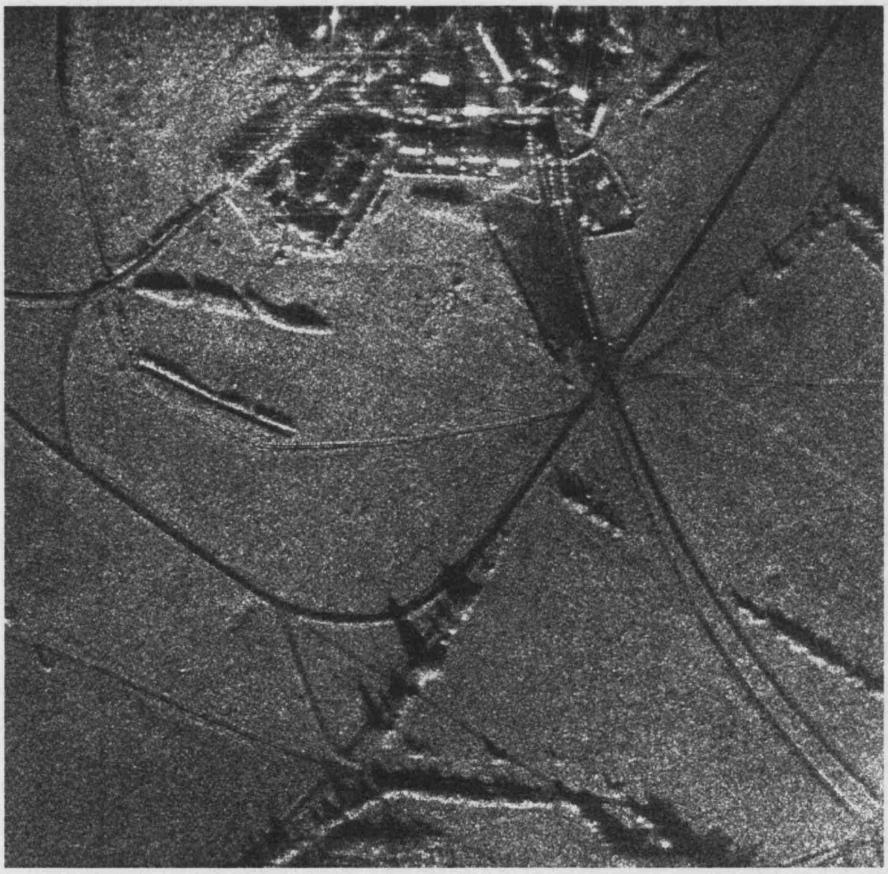

Figure E-9 Bistatic image of leg 11

Due to the lack of clear point targets in the image, it is difficult to measure the resolution accurately. However, using the brightest fence posts in the car park gives a resolution lower than requested in the processor. The image is not well focused. Again this is due to the longer aperture time causing problems with the motion compensation solution and the image quality suffering.

E.1.5 Imaging leg 13

For this imaging run, ESR was again transmitting the higher bandwidth. Data was collected around a nominal 60° bistatic angle with ADAS flying at a fast rate in the same sense as ESR, both platforms at the same grazing angle.

The image presented below in Figure E-10 is processed from data towards the end of the run.

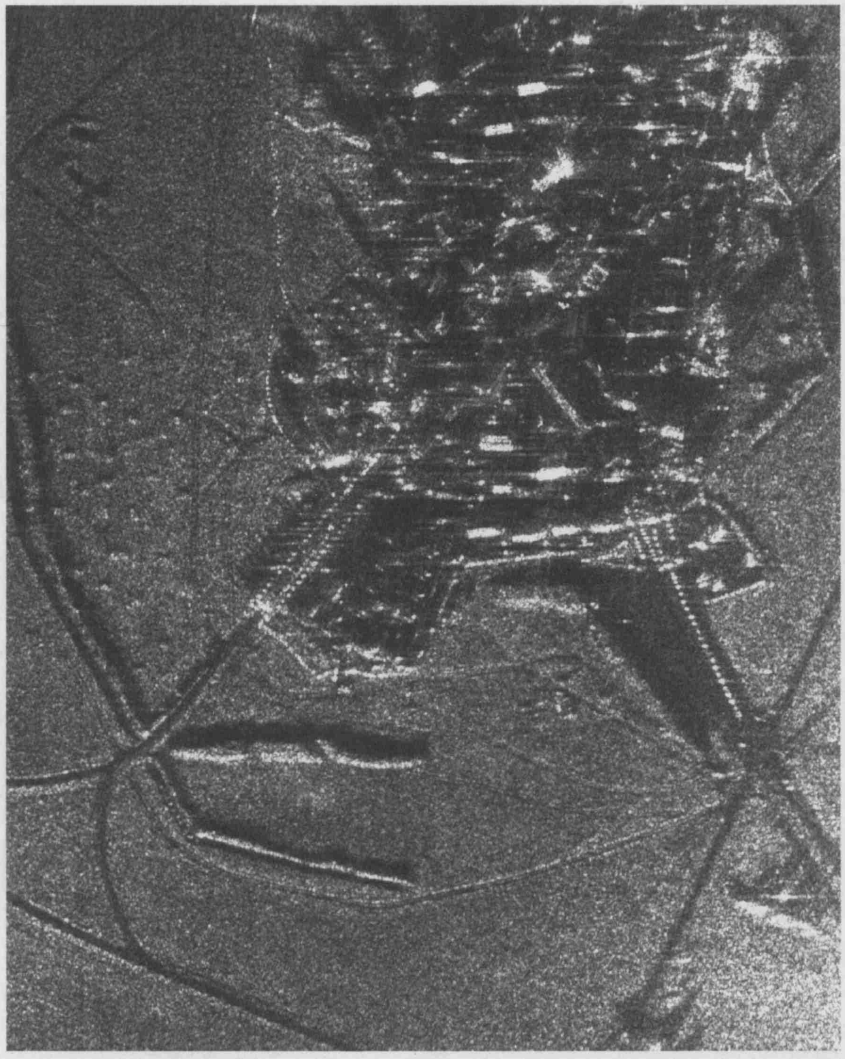

Figure E-10 Bistatic image from leg 13

Measuring the resolution from this image is close to the requested value. Once again the clutter areas appear well focused. The urban part remains slightly out of focus.

E.1.6 Imaging leg 14

This data shows the effects of retrograde motion with ADAS moving in the opposite sense to ESR. To form this image, large amounts of data need to be

processed. The image in Figure E-11 is only processed to a low resolution in both dimensions. For higher azimuth resolution, a longer aperture would need to be processed. With the current motion compensation solution for ADAS, this is not possible.

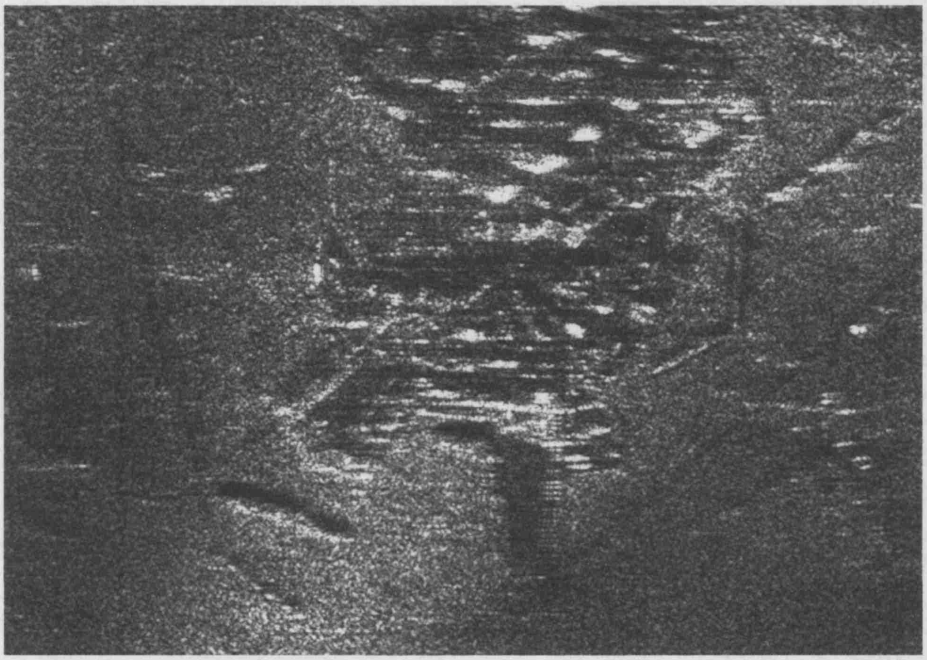

Figure E-11 Bistatic image from leg 14

Even processing this data to a fairly low-resolution image, it is clear that the motion compensation solution is introducing errors into the image. This could be due to the quality of the navigation data (known to have errors) or due to the solution formed from this data. The autofocus solution is also not able to focus any part of the image well. The image is still recognisable, but further development of the processing tools is required to produce better imagery.

F Photographs from the trials

This appendix presents a few photographs from both the ground and air trials. The first section is photographs from the ground trial showing the synchronisation procedure and the set up. F.1.2 presents photographs from the air trial. The first few of these show the synchronisation process. The latter ones show key features of the target scene which can be used as an aid to understanding the imagery presented in sections 7.6 and Chapter 8.

F.1.1 Photographs of key features from ground trial

The photographs in this section aim to aid understanding of the procedures taking place during the ground trial. Figure F-12 shows the installation of the atomic clock and interface unit next to the control unit of ESR.

Figure F-12 Atomic clock and interface unit installation onboard ESR

Figure F-13 shows the position for synchronisation on the first day of the ground trial. This was used for testing the synchronisation procedure and measuring the delay between the clocks.

Figure F-13 Initial synchronisation tests

Figure F-14 is a photograph taken during the atomic clock synchronisation process on the morning of the full ground trial with ESR in the position where it will later be radiating from.

Figure F-14 Synchronisation on day of ground trial

Figure F-15 is a photograph of ESR taken from approximately the direction inline with where ADAS will be in position 1. This shows how close the radar antenna is to the ground as well as the positioning of the front wheel of ESR.

Due to restrictions on the positioning of ESR, this was the furthest around the aircraft could turn.

Figure F-15 ESR ground clearance and position of front wheel

The photograph below shows ADAS in position 1, with the targets close by it.

Figure F-16 ADAS in position 1 with targets

Figure F-17 is a photograph taken from the targets with ADAS in position2 in front of ESR. This was to try and simulate the bistatic nature that the radars would be used in. Trying to recorded the bistatic path from ESR to the targets and back to ADAS. The direct path signal could also be recorded on the omni-directional antenna.

Figure F-17 Taken from targets, ADAS in position 2 in front of ESR

F.1.2 Synchronisation from air trial

The atomic clocks were previously installed onboard each aircraft and warmed up under ground power. The two aircraft were then brought close together so that the clocks could be connected via a cable for synchronisation. The pictures below show this process.

Figure F-18 Atomic clock synchronisation

F.1.2.1 Air trial target scene photographs

The photographs presented here show key features of the target scene which can be used as an aid to understanding the imagery presented in sections 7.6 and

Chapter 8. To aid identification, Figure 8-1, the monostatic image from leg 4, is repeated here. It is labelled with some key features of the target scene

Figure F-19 Monostatic image of scene

Aerial photographs have been taken from onboard ADAS during previous trials. Any personnel or vehicles in these photographs are not relevant to this imagery.

The area shown in Figure F-20 was set up as the scene centre. This was because the large open concrete area was a good base and allowed for bistatic targets to be placed there.

Figure F-20 Photograph showing the scene centre

During the bistatic trial this area was enclosed with a metal fence, shown in Figure F-22. A calibration target (sphere) was placed here in the middle of the scene. In order to try and maintain a good line of sight in both imaging scenarios (30° and 60° bistatic angles) the sphere had different positions marked by plastic poles. Note the third pole marks the best line of sight for 0° bistatic angle, although this geometry was not used. These three poles can be seen inside the circle in the monostatic image, with the sphere next to the most northern pole (although it is not obvious in the image).

Figure F-21 Fence and poles around scene centre, sphere in easterly position

The large sphere was secured using a tyre. The sphere was always in front of the marker pole as shown in Figure F-23

Figure F-22 Large sphere in scene centre

Below is an aerial photograph taken from the south-west of the village. It clearly shows the two rows of dormer houses. The most southerly row has dormer windows in the middle of each roof on the south side. The second row has dormer windows on the north side of the roof, although this cannot be seen in the photograph. This picture also gives an indication of the relative heights of the buildings in the south-west corner of the village.

Figure F-23 Photograph of village taken from the south-west looking north-east

Close-up pictures of the dormer houses are shown in the figure below.

Figure F-24 Individual dormer house and the row of dormer houses

Towards the bottom right of the monostatic image in Figure F-19, there is a large return from the barn pictured below. This return is from the metal supports which can clearly be seen in Figure F-26. The picture is from a previous trial, and the vehicles are not relevant to this experiment. The image is taken from the north-west of the building.

Figure F-25 Barn with metal supports

There is a new single storey building built towards the south of the village that produces a large return in the monostatic image. It is a fairly new building and does not appear in the plans, Figure 8-2 or aerial photograph in Figure 8-3.

Figure F-26 New single story building

Towards the centre of the village the building shown in Figure F-27 shows up in the radar imagery. This is due to the metal fencing around the top of it. In some of the better imagery each fence post can be seen.

Figure F-27 Fenced roof building

The roofs of the buildings in the village are made from large corrugated 'tiles'.

Figure F-28 Roof structure of buildings

References

1. Horne, A. M., Yates, G. A., "Bistatic synthetic aperture radar", Proceedings of the Radar 2002 Conference, Edinburgh, Scotland, October 2002, IEE publication No. 490, pp 6-10, October 2002.

2. Yates, G. A., Horne, A. M. *et al.*, "Bistatic SAR image formation". Proceedings of the EUSAR conference, Ulm, Germany, May 2004, pp 581-584.

3. Stimson, G. W., "Introduction to Airborne Radar", published by SciTech Publishing Inc, 1998.

4. Willis, Nicholas J., "Bistatic Radar", published by Artech House, 1991.

5. Skolnik, M., "Introduction to radar systems", published by Mcgraw-Hill, 1980.

6. Auterman, J. L., "Phase stability requirements for a bistatic SAR", IEEE Nat. Radar Conf. Atlanta March 1984, pp48-52.

7. Galati, G., "Advanced radar techniques and systems", published by Peter Peregrinus Ltd. Chapter 11, "Bistatic Radar", Dunsmore, M.R.B.

8. Jackson, M. C., "The geometry of bistatic radar systems", IEE Proceedings, Vol. 133, Pt. F, No. 7, December 1986, pp604-612.

9. Milne, K., "Principles and concepts of multistatic surveillance radars", Radar 1977 conference, London, IEE Conference Publication 155, pp 26-52.

10. Schoenenberger, J.G., Forrest, J. R., 'Principles of independent receivers for use with co-operative radar transmitters' The Radio and Electronic Engineer, Vol. 52, No. 2, pp 93 – 101, February 1982.

11. Griffiths, H. D., Carter, S.M., "Provision of moving target indication in an independent bistatic radar receiver2, The Radio and Electronic Engineer, Vol. 54, No. 7/8, pp 336-342. July/August 1984.

12. Howland, P. E. "A passive metric using a radar of opportunity", Colloque International sur le Radar, Paris, pp251-256 Société des Electriciens et des Electroniciens, 3-6 May 1994.

13. Howland, P. E., "Target tracking using television-based bistatic radar". IEE Proc –Radar, Sonar Navig., Vol. 146, No. 3, pp 166-174. June 1999.

14. www.sandia.gov/radar/images/bistatic.jpg

15. Martinsek, D., Goldstein, R., "Bistatic Radar Experiment". Proceedings of the EUSAR conference, May 1998, Friedrichshafen, Germany.

16. Elson, B. M., "Bistatic airborne radar use studied", Aviation Week and Space Technology August 13, 1979, pp 57-59.

17. Blumgold, R. "Tactical bistatic radar demonstrated", Defense electronics, December 1980, pp 78-82.

18. Fawcette, J., "Vulnerable radars seek safe sanctuary", MSN April 1980, pp 45-50.

19. Kirk, J.C., "Bistatic SAR Motion Compensation". IEEE International Radar Conference 1985 pp 360-365.

20. Cardillo, G. P. "On the use of the gradient to determine bistatic SAR resolution", IEEE Antennas and Propagation Society International Symposium 1990 pp 1032-1035.

21. Soumekh, M., "Bistatic synthetic aperture radar inversion with application in dynamic object Imaging". IEEE Transactions on signal processing Vol 39, No 9, pp 2044-2055. September 1991.

22. Soumekh, M., "Wide-bandwidth continuous-wave monostatic/bistatic synthetic aperture radar imaging", IEEE Image processing 1998, ICIP proceedings1998 pp 361-365.

23. Dubois-Fernandez, P. *et al.*, "Analysis of bistatic scattering behaviour of natural surfaces", Proceedings of the EUSAR conference, Ulm, Germany, May 2004, pp 573-576.

24. Cantalloube, H. *et al.*, "Challenges in SAR processing for airborne bistatic acquisitions", Proceedings of the Radar 2004 Conference, Toulouse, France, October 2004.

25. Rigling, B. D., Moses, R. L., "Polar Format Algorithm for Bistatic SAR", IEEE Transactions on aerospace and electronic systems, Vol 40, No 4, pp1147-1159. October 2004.

26. Simon, M. P. *et al.*, "Bistatic ISAR Images from a Time-Domain Code", IEEE Antennas and Propagation magazine, Vol 37, No 5, pp 25-32. October 1995.

27. Unpublished DERA report.

28. Carrara, W.G. *et al.*, "Spotlight synthetic aperture radar", published by Artech House, 1995, pp 81-200.

29. Unpublished QinetiQ report.

30. Jakowatz, C.V. *et al*, "Spotlight-mode synthetic aperture radar: a signal processing approach", published by Kluwer Academic publishers, 1996, pp 98-103.

31. Carrara, W.G. *et al.*, "Spotlight synthetic aperture radar", published by Artech House, 1995, pp 401-442.

32. http://www.thales-communications.ltd.uk/prediction.htm

33. Turner, S. D. "RESPECT, rapid electromagnetic scattering predictor for extremely complex targets", IEE Proceedings, Vol 137 Pt F, No F, August 1990.